

MODELING OF MIXED-MODE FATIGUE CRACK PROPAGATION

By

Liming Liu

Dissertation

Submitted to the Faculty of the
Graduate School of Vanderbilt University

In partial fulfillment of the requirements

for the degree of

DOCTOR OF PHILOSOPHY

in

Civil Engineering

May, 2008

Nashville, Tennessee

Approved

Professor Sankaran Mahadevan

Professor Prodyot K. Basu

Professor Carol A. Rubin

Professor Caglar Oskay

Copyright © 2008 by Liming Liu
All Rights Reserved

To my parents

ACKNOWLEDGEMENT

This work would not have been possible without the guidance and support of many people. I thank all of my Dissertation Committee members for their advice and suggestions. Especially to my dissertation supervisor and mentor, Dr. Sankaran Mahadevan, I appreciate your guidance, inspiration, encouragement, and enthusiasm throughout my stay at Vanderbilt. As a successful scientist, erudite and diligent, you are an excellent model for me in both academics and personal life. I would like to thank Dr. Prodyot K. Basu for his advice, suggestions and direction on my graduate study.

I truly appreciate the friendship and technical support I received from Dr. Yongming Liu throughout my graduate study. I am also thankful for the help and valuable discussions from our research group members, Dr. Brant Stratman, Chris Shantz, Venkata Sura, Xinyu Chen. Thanks to Dr. Xiaomo Jiang and all IGERT students for their encouragement and friendship.

I would like to extend my thanks to Union Pacific Railroad, Transportation Technology Center, Inc., Federal Aviation Administration, and Department of Civil and Environmental Engineering at Vanderbilt for their financial support. I would also like to thank Dr. Dan M. Ghiocel, Dr. Letian Wang, Dr. Ning An and Qionglin Wu for their advice and guidance during my internships at Ghiocel Predictive Technologies, Inc.

Finally I want to extend my most gracious and special thanks to my parents. Without the endless support and encouragement you have given me over the years, this could not have been completed.

TABLE OF CONTENTS

	Page
DEDICATION.....	iii
ACKNOWLEDGEMENT.....	iv
LIST OF TABLE.....	vii
LIST OF FIGURES.....	viii
Chapter	
I. INTRODUCTION.....	1
1.1 Overview.....	1
1.2 Research objectives.....	3
1.3 Advantages of the proposed methodology.....	4
1.4 Organization of the dissertation.....	6
II. MIXED-MODE NEAR THRESHOLD FATIGUE CRACK GROWTH IN SMOOTH SPECIMEN.....	8
2.1 Overview.....	8
2.2 Existing mixed-mode fatigue models.....	11
2.3 Proposed mixed-mode I and II fatigue model.....	22
2.3.1 Multiaxial fatigue limit criterion.....	22
2.3.2 Fatigue limit and threshold stress intensity factor.....	23
2.3.3 Mixed-mode I and II threshold stress intensity factor.....	24
2.3.4 Mixed-mode I and II fatigue crack growth.....	31
2.3.5 Experimental validation.....	32
2.4 Proposed mixed-mode I and III fatigue model.....	36
2.4.1 Mixed-mode I and III threshold stress intensity factor.....	36
2.4.2 Mixed-mode I and III fatigue crack growth.....	48
2.4.3 Experimental validation.....	49
2.5 Proposed mixed-mode I, II and III fatigue model.....	51
2.6 Conclusion.....	59
III. MIXED-MODE NEAR THRESHOLD FATIGUE CRACK GROWTH FROM NOTCH.....	60
3.1 Overview.....	60
3.2 Proposed mixed-mode I and II fatigue model for notched specimen.....	65

3.2.1 Fatigue limit and threshold stress intensity factor for notched specimen	65
3.2.2 Mixed-mode I and II threshold stress intensity factor	65
3.2.3 Mixed-mode I and II fatigue crack growth	73
3.3 Proposed mixed-mode I and III fatigue model for notched specimen.....	74
3.3.1 Mixed-mode I and III threshold stress intensity factor	74
3.3.2 Mixed-mode I and III fatigue crack growth.....	85
3.4 Proposed mixed-mode I, II and III fatigue model for notched specimen	86
3.4.1 Mixed-mode I, II and III threshold stress intensity factor	86
3.5 Conclusion	94
IV. MIXED-MODE SMALL FATIGUE CRACK GROWTH	95
4.1 Introduction.....	95
4.2 Background.....	96
4.3 Existing criteria.....	99
4.4 Proposed criterion	107
4.4.1 Fatigue limit and microscopic threshold stress intensity factor.....	107
4.4.2 Stress intensity factor in anisotropic material.....	110
4.4.3 Mixed mode I and II stress intensity factor	113
4.5 Conclusion	117
V. APPLICATION TO RAILROAD WHEELS	118
5.1 Overview.....	118
5.2 Finite element modeling of subsurface crack in wheel/rail contact.....	121
5.3 Conclusion	132
VI. CONCLUSION AND FUTURE WORK.....	133
6.1 Summary of contribution	133
6.2 Future work.....	134
REFERENCES	136

LIST OF TABLES

Table	Page
Table 1. Experimental threshold SIF data used for model validation.....	33
Table 2. Experimental crack growth rate data used for model validation	36
Table 3. Experimental threshold data used for model validation	49

LIST OF FIGURES

Figure	Page
Figure 1. Kitagawa diagram for fatigue limits and threshold stress intensity factor	23
Figure 2. Mixed-mode I and II stress fields near crack tip	25
Figure 3. Orientation of characteristic plane and maximum shear stress (MSS) plane	29
Figure 4. γ vs. ξ for mixed-mode I+II	30
Figure 5. B vs. ξ for mixed-mode I+II	30
Figure 6. Mixed-mode I+II crack orientation β using the MSS criterion	31
Figure 7. Comparisons of predicted and experimental threshold stress intensity factors for mixed-mode I+II	34
Figure 8. Comparisons of predicted and experimental fatigue crack growth rates	35
Figure 9. Mixed-mode I and III stress fields near crack tip	37
Figure 10. Orientation of characteristic plane and maximum shear stress (MSS) plane for mixed-mode I+III	45
Figure 11. γ vs. ξ for mixed-mode I+III (plane stress)	46
Figure 12. B vs. ξ for mixed-mode I+III (plane stress)	46
Figure 13. Mixed-mode I and III crack orientation β using MSS criterion ($\nu = 0.3$ in plane strain)	47
Figure 14. Comparisons of predicted and experimental threshold stress intensity factors for mixed-mode I+III	50
Figure 15. Mixed-mode I, II and III stress fields near crack tip	51
Figure 16. θ vs. K_I / K_{II}	56
Figure 17. Typical notch configurations	62
Figure 18. Mixed-mode I and II stress fields near notch tip	66
Figure 19. Orientation of characteristic plane and maximum shear stress (MSS) plane ..	71

Figure 20. γ vs. ξ	72
Figure 21. B vs. ξ	72
Figure 22. Mixed-mode I and II crack orientation θ using MSS criterion	72
Figure 23. Mixed-mode I and III stress fields near notch tip.....	75
Figure 24. Orientation of characteristic plane and maximum shear stress (MSS) plane for mixed-mode I+III in notched specimens	82
Figure 25. Mixed-mode I and III crack orientation β using the MSS criterion ($\nu = 0.3$ in plane strain).....	84
Figure 26. Mixed-mode I, II and III stress fields near notch tip.....	87
Figure 27. θ vs. K_I / K_{II}	91
Figure 28. Crack growth classification	97
Figure 29. Threshold behavior by Miller [91]	97
Figure 30. Kitagawa-Takahashi diagram [11]	97
Figure 31. Small crack behavior [109]	98
Figure 32. Fatigue life fraction [109].....	98
Figure 33. Coplanar slip band emanating from the tip of isolated crack [121]	108
Figure 34. Coordinate system near crack tip	110
Figure 35. The complex parameters in two coordinate systems.....	110
Figure 36. Crack tip elements	112
Figure 37. Crystal structures	114
Figure 38. Mixed mode I and II stress fields near small crack tip.....	115
Figure 39. Inclusions and pores in wheel material	120
Figure 40. Finite element modeling of wheel/rail contact with subsurface crack	125
Figure 41. Von-Mises stress distribution of wheel/rail contact	126
Figure 42. In-plane shear stress distribution of wheel/rail contact	126
Figure 43. Stress history at two locations in the wheel.....	127

Figure 44. Parameters used in parametric study	128
Figure 45. $\Delta K_{mix,eq}$ vs. applied load	130
Figure 46. $\Delta K_{mix,eq}$ vs. crack length (2a)	130
Figure 47. $\Delta K_{mix,eq}$ vs. grain orientation	130
Figure 48. $\Delta K_{mix,eq}$ vs. grain disorientation	130
Figure 49. Mesh and Von-Mises stress distribution near crack tip.....	131

CHAPTER I

INTRODUCTION

1.1 Overview

Safe-life design is a design approach that has traditionally been used in aircraft structures. This approach assumes no preexisting defects in components. Since all engineering materials and components contain flaws that may grow under cyclic loading even if they are very small and initially safe, it is necessary to study the behavior of preexisting flaws and cracks and to assess how such defects will affect the integrity of components. Damage tolerance design, which assumes the component has preexisting flaws and uses fracture mechanics to predict the fatigue life, has been adopted for fixed-wing aircraft since the 1970's. And it has begun to be studied for rotorcraft in addition to the safe-life approach [1].

Most previous damage tolerance analyses for aircraft and other structures employ fatigue crack growth analysis based on long crack behavior. However, due to the high damage accumulation rate, near threshold crack and small crack behavior is the major concern for the damage tolerance approach. Many helicopter components are subjected to high cycle, low stress, and high stress ratio stress fields. Analytical and experimental approaches to determine multiaxial small crack growth rates and crack growth threshold are not well established and remain an active research topic. In addition, material test data for threshold region is limited and exhibits significant scatter. The commonly used fatigue crack growth formulae in NASGRO and AFGROW codes have shown large

scatter in crack growth life prediction especially in the near threshold region [2]. Thus the fatigue crack growth behavior at near threshold regime is of significant importance and is a central focus of research interest at FAA [3].

It is well known that small crack behavior significantly differs from large crack behavior. Both the crack growth rate curve shape and underlying failure mechanism are quite different. Small fatigue cracks grow at stress intensity factors significantly below the large crack fatigue threshold and grow faster than large cracks at the same ΔK level above threshold. Failure modes of small cracks relate to different material microstructures and damage accumulation at the microstructure level (i.e., slip bands and micro-void coalescence).

The investigation of small fatigue crack behavior has been mostly focused on constant amplitude mode I loading in previous studies. However possible non-planar crack growth and complex external loading will result in mixed-mode fatigue crack growth of small cracks. Service loads on most fatigue-critical structures are usually with random amplitude, such as those experienced by fighter aircraft [4]. Previous work shows that prior loading history involving random loading or multiple overloads can influence fatigue crack growth thresholds [5-8]. The stochasticity in material properties, structural properties and external loadings need to be included in fatigue life prediction.

This dissertation combines structural failure analysis and advanced finite element analysis to develop a methodology for the fatigue life assessment of metallic structures and components. Failure analysis focuses on developing fundamental mixed-mode near threshold and small fatigue crack propagation prediction models and implementing these models with finite element analysis.

1.2 Research objectives

The study attempts to extend the current state-of-the-art methods and develop solutions for mixed-mode near threshold and small fatigue crack life prediction. The proposed objectives are:

1. Develop analytical model for mixed-mode threshold stress intensity factor and crack growth rate prediction in smooth specimen. Based on the multiaxial fatigue limit criterion proposed earlier by Liu and Mahadevan [9], the method is developed using local stresses near the crack tip rather than remote stresses. It is applicable to both ductile and brittle materials and has the potential to be extended for notched specimen. The predicted fatigue crack growth rate is compared with the experimental data in the open literature or in-field observations.
2. Develop analytical model for mixed-mode threshold stress intensity factor and crack growth rate prediction in notched specimen, which extends the life prediction capability from material/specimen level to component/structural level. Most engineering components have notch-like features, such as shoulders, keyways, oil holes, grooves and threads, which induce high local stresses and strains at notch roots. The local stresses near the notch tip and the Kitagawa-Takahashi diagram for notched specimen are combined with an earlier proposed multiaxial fatigue limit criterion to develop the equivalent stress intensity factor for crack growth rate prediction.

3. Develop analytical model for mixed-mode small fatigue crack growth. In this task, the local stress field is transformed onto the slip plane of crystal near small crack tip. The contribution of shear stress on the slip plane, which has been considered as the only driving force of small crack growth in earlier studies, as well as normal stress and hydrostatic stress are taken into account for the life prediction of structures with small cracks.
4. Develop a computational methodology for the life prediction of components under complex loading, such as the rolling contact fatigue simulation of railroad wheels, combining macro-micro level finite element analysis with the proposed mixed-mode fatigue crack growth model. Earlier Liu [10], predicted the fatigue life of railroad wheels with the assumption of initial crack size greater than 1 mm. In this study the failure analysis of railroad wheel starts with the initial crack size less than one grain diameter.

1.3 Advantages of the proposed methodology

Mixed-mode fatigue crack propagation prediction is a challenging problem and a wide variety of experimental and computational models have been proposed in the literature. The test-only based approach is very expensive and inadequate for large scale complex component/system level application. Inexpensive modeling and simulation-based methods depend largely on the assumption for material, loading and environment and none of them have achieved universal acceptance. The study in this dissertation compared the existing methods and proposed some alternative to address the problem with less assumption and broader applicability.

The proposed methodology includes analytical models for mixed-mode stress intensity factor and crack growth rate prediction in both near threshold region and microstructurally small crack region. The method is developed using local stresses near the crack/notch tip rather than remote stresses. The major advantages of the proposed methodology are: (i) The fatigue model can automatically adapt for tensile/shear failure mechanisms according to material properties and loading conditions; (ii) Local geometric effects and residual stress effects can be addressed easily, which makes it feasible for life prediction at the component/structural level; (iii) The effects of various microstructural factors on stage I fatigue crack growth are included; (iv) The semi-analytical formulas quantify equivalent mixed-mode stress intensity factors, which makes fatigue life prediction more easy, efficient and accurate.

The proposed macro-micro level simulation models are applied for the rolling contact fatigue analysis in railroad wheels. The major advantages of the proposed models are: (i) The macro-level 3-D finite element model is versatile in representing complex wheel tread (or rail head) profiles, which is especially important when the contact conditions can not satisfy the Hertz assumptions; (ii) The micro-level 2-D finite element model considers material anisotropy, and randomness in both grain size and grain orientation. The effects of applied load, crack size, grain orientation and grain disorientation on the mixed mode equivalent stress intensity factor are investigated using the proposed model.

1.4 Organization of the dissertation

The dissertation is organized as follows: In Chapter 2, after a brief review of current multiaxial fatigue models and mixed-mode fatigue growth models, new formulas for mixed-mode I+II/I+III/I+II+III threshold stress intensity factor and crack growth rate prediction in smooth specimens are derived based on a characteristic plane approach. The predictions of the proposed fatigue damage model under constant amplitude loading are compared with a wide range of experimental fatigue results in the literature.

Chapter 3 extends the proposed model in Chapter 2 for notched specimens by including the notch tip radius within the local stress expressions, and the relationship between fatigue limit and threshold stress intensity factor.

Chapter 4 applies the proposed mixed-mode threshold fatigue model to stage I fatigue crack growth. Various microstructural factors are taken into account. The relationship between fatigue limit and microscopic threshold stress intensity factor is used instead of the Kitagawa-Takahashi diagram [11], which is more suitable for long cracks. Material anisotropy is addressed instead of the isotropic assumption used in earlier studies.

Chapter 5 combines macro-micro level finite element analysis with the proposed mixed-mode fatigue crack growth model for shattered rim failure analysis in railroad wheels. The non-proportional multiaxial stress state is analyzed using the macro-level model, and the equivalent tensile stress calculated by the former proposed multiaxial fatigue limit criterion [9] is applied to the micro-level model as the boundary condition. Voronoi tessellation and Monte Carlo simulation are used to address the randomness in

grain size and grain orientation. Parametric studies are carried out for the subsurface fatigue crack behavior within and beyond the grain boundary.

CHAPTER II

MIXED-MODE NEAR THRESHOLD FATIGUE CRACK GROWTH IN SMOOTH SPECIMEN

2.1 Overview

Fracture mechanics has been widely used to predict the fatigue crack growth of flawed structures under mode I loading condition. In many practical problems, either the crack is not perpendicular to the mode I loading direction, or the structure is subjected to multiaxial loadings, resulting in a mixed-mode stress field near crack tip. Under such mixed-mode loading conditions, the shear mode loading can accelerate crack growth and the crack may deviate from the original crack path.

A number of multiaxial fatigue models [12-14] and mixed-mode fatigue crack growth models [15, 16] have been proposed in the literature. Among multiaxial fatigue models using the $S-N$ (or $\varepsilon-N$) curve approach, the critical plane-based models have been gaining in popularity due to their effectiveness and broad application range [13]. The main purpose in critical plane-based methods is to reduce the multiaxial stress state into an equivalent uniaxial one. The development of this approach is based on the observation that the fatigue crack nucleates along certain planes in the material. Such a plane is named “critical plane” and the stress (or strain) components on it are used for fatigue analysis [12]. The critical plane coincides with the maximum shear stress plane during the crack initiation period and coincides with the maximum normal stress plane during the crack propagation period. The dominance of shear vs. tensile type crack

depends on the ratio of shear stress/strain to normal stress/strain, material property and temperature. It has been found that existing models based on shear type failure mechanism perform poorly for tensile type cracks and vice versa [17-19]. Jiang [20] proposed an incremental critical plane-based model which is capable of dealing with tensile cracking, shear cracking, and mixed cracking behavior. Recent work by Jiang and Feng [21] and Feng et al. [22] has extended the application of the Jiang multiaxial fatigue criterion to predicting general crack growth. As the Jiang model used plastic strain energy as the major measure of the fatigue damage, the model is only applicable to ductile materials.

In the case of mixed-mode fatigue crack growth models, a similar trend comparable with those of the multiaxial fatigue models can be found in the literature. A number of existing models assume that the tensile crack growth dominates during the fatigue crack propagation. The maximum tangential stress (MTS) criterion proposed by Erdogan and Sih [23] and the maximum tangential strain (MTSN) criterion proposed by Chambers et al. [24] are two typical models using the tensile failure mode assumption. Yan et al. [25] used an equivalent stress intensity factor defined on the maximum tangential stress plane, which also assumed the tensile failure mode. Many other models based on energy concepts, such as the energy release rate model [26], strain energy density model [27] and dilatational strain energy density model [28], can be also deemed as variations of a tensile failure-based model similar to the MTS criterion [29]. Compared with a large number of models based on the tensile failure mode, relatively few models based on the shear failure mode are available in the literature. Otsuka et al. [30] observed Mode II crack growth in ductile steels and stated that fatigue cracks can either grow

along the maximum tangential stress plane (mode I) or along the maximum shear stress plane (mode II). A similar approach for the crack growth under static loading has been proposed by Chao and Liu [29], in which the MTS criterion and the MSS (maximum shear stress) criterion are combined together to predict the crack growth. Socie et al. [31] proposed an equivalent strain intensity factor for the near threshold small crack growth, which is defined on the maximum shear strain plane. A similar approach was also proposed by Reddy and Fatemi [32].

It is well known that models based on the tensile failure mode work well for brittle materials. For ductile materials, both mode I and mode II cracks could occur and the models based on a single failure mechanism cannot give a satisfactory prediction [15, 29]. For mixed-mode fatigue crack growth, it has been reported that the crack could change the growth mode depending on the applied loading amplitude [33]. Gao et al. [33] observed that the near threshold crack growth is shear-mode and the crack branches to tensile-mode when the applied mixed-mode loading is gradually increased. This type of observation indicates that no single model based on a specific failure mechanism can be applied to the whole regime of the fatigue crack growth, i.e., from near-threshold crack growth to long crack growth, since the underlying failure mechanism could be different.

A new model for mixed-mode threshold stress intensity factor and crack growth rate prediction is proposed in this study. The method is developed using local stresses near the crack tip rather than remote stresses. Two major advantages of the proposed model are that (1) it can automatically adapt for different failure mechanisms and (2) local geometric effects and residual stress effects near crack tip can be included in this local stress based model more easily than the remote stress approach, such as cracks

emanating from notches or holes by considering notch radius in the expressions of stress fields near notch tips.

In the section 2.3, the derivation of the model is demonstrated using a smooth specimen with central crack under remote tension. A multiaxial fatigue limit criterion developed earlier by Liu and Mahadevan [9] is extended to develop a threshold stress intensity factor criterion using the Kitagawa-Takahashi diagram [11]. Following this, an equivalent stress intensity factor is proposed for the crack growth rate prediction. The predictions of the proposed fatigue damage model under constant amplitude loading are compared with a wide range of experimental fatigue results in the literature.

2.2 Existing mixed-mode fatigue models

(1) Models using effective stress intensity factors

Fatigue crack growth in metals is usually estimated by using Paris law [34], which is originally proposed for single mode deformation cases. If further crack propagation occurs in the direction of the existing crack, a modified Paris law for mixed-mode loading can be expressed using the effective stress intensity factor (SIF) range as follows:

$$\frac{da}{dN} = C(\Delta K_{eff})^m \quad (1)$$

where C and m are material constants. This equation represents a linear relationship between $\log(\Delta K_{eff})$ and $\log(da/dN)$ which is used to describe the fatigue crack propagation behavior in region II. However the effect of mean stress, loading and specimen geometry are not included in this equation.

For characterizing the effect of stress ratio R ($R = K_{min} / K_{max} = \sigma_{min} / \sigma_{max}$),

Walker [35] proposed the following equation:

$$\frac{da}{dN} = C \left(\frac{\Delta K_{eff}}{(1-R)^{1-\gamma}} \right)^m \quad (2)$$

where C is a constant and m is the slope on the log/log plot. Also, γ is the material constant obtained from data at various R , while the closing values of $\gamma = 1$ imply the weaker effect of R . The constant γ of the Walker equation for rail steel is 0.82, whereas γ of aluminum alloy and AISI 4340 steel are 0.64 and 0.42, respectively. Accordingly, the stress ratio was shown to affect fatigue crack growth behavior of rail steel less than that of these steels [36].

Eq.(2) does not account for the crack growth characteristics at both low and high levels of ΔK . At high ΔK values, as K_{max} approaches the critical level K_c , an increase in crack growth rate is observed. For this case Forman *et al.* [37] proposed the relation

$$\frac{da}{dN} = \frac{C(\Delta K)^n}{(1-R)K_c - \Delta K} \quad (3)$$

where C and n are material constants. The term $[(1-R)K_c - \Delta K]$ will decrease with increasing stress ratio R and decreasing fracture toughness K_c , both of which give rise to increasing crack growth rates at a given ΔK level. For $K_{max} = K_c$, corresponding to instability, this equation predicts an unbounded value of da/dN .

For low value of ΔK , Donahue *et al.* [38] suggested the relation

$$\frac{da}{dN} = K(\Delta K - \Delta K_{th})^m \quad (4)$$

where ΔK_{th} denotes the threshold value of ΔK .

Erdogan and Ratwani [39] have suggested a generalized fatigue crack growth law,

which can describe the sigmoid response. A relation of the form

$$\frac{da}{dN} = \frac{C(1+\beta)^m(\Delta K - \Delta K_{th})^n}{K_c - (1+\beta)\Delta K} \quad (5)$$

where C , m , n are empirical material constants and

$$\beta = \frac{K_{\max} + K_{\min}}{K_{\max} - K_{\min}} \quad (6)$$

The factor $(1+\beta)$ has been introduced to account for the effect of the mean stress level on fatigue crack propagation, while the factor $K_c - (1+\beta)\Delta K$ takes care of the experimental data at high stress levels and the factor $(\Delta K - \Delta K_{th})^n$ accounts for the experimental data at low stress levels.

An advanced approach is the so-called NASGRO expression (also called Forman-Newman-de Koning equation), which is now common in aerospace applications. This equation describes all sections of the $\frac{da}{dN} - \Delta K_{eff}$ diagram.

$$\frac{da}{dN} = C(\Delta K_{eff})^n \frac{\left(1 - \frac{\Delta K_0}{\Delta K_{eff}}\right)^p}{\left(1 - \frac{K_{\max}}{K_{Jc}}\right)^q} \quad (7)$$

where $C(\Delta K_{eff})^n$ is fitted to the data in the so-called Paris range (range II),

$\left(1 - \frac{\Delta K_0}{\Delta K_{eff}}\right)^p$ and $\left(1 - \frac{K_{\max}}{K_{Jc}}\right)^q$ are used for describing range I and range III. ΔK_0 is the

fatigue threshold, K_{\max} is the maximum stress intensity factor in a load cycle, K_{Jc} is the crack resistance against fracture and p and q are empirical constants from curve fitting.

Pook and Greenan [40] found that crack growth in all cases was at an angle of

roughly 70° with respect to the original crack line even though the applied stress field was mode II. Roberts and Kibler [41] suggest using the following equation for shear fatigue crack growth

$$\frac{da}{dN} = \frac{C_1(\Delta K_I)^{n_1} + C_2(\Delta K_{II})^{n_2}}{\left[\left(\frac{K_{I \max}}{K_{Ic}} \right)^2 + \left(\frac{K_{II \max}}{K_{IIc}} \right)^2 - 1 \right]} \quad (8)$$

(2) Newman's crack closure model

To consider crack closure during crack propagation we can use Newman's crack closure model [42]:

$$\frac{da}{dN} = C(\Delta K_{eff})^n G / H \quad (9)$$

where

$$G = 1 - \left(\frac{\Delta K_o}{\Delta K_{eff}} \right)^p \quad (10)$$

$$H = 1 - \left(\frac{K_{\max}}{C_5} \right)^q \quad (11)$$

The cyclic fracture toughness, like the elastic fracture toughness, is a function of crack length, specimen width, and specimen type.

(3) Chen and Keer's model

Based on Dugdale's model, the fatigue crack growth rate was related to the accumulated crack opening and sliding plastic displacements by Chen and Keer [43]. The following assumptions were made: (i) the crack closure and the crack branching effects can be neglected; (ii) the total accumulated plastic displacement is the vector sum of the accumulated crack opening and crack sliding displacements; and (iii) the tensile and

shear stresses in the yield zone satisfy the von Mises criterion. Based on these assumptions as well as the relationship between stress intensity factors and displacements, and the relationship between ΔJ and displacements under small scale yielding condition, the following expressions were derived for mixed-mode I and II loadings:

$$\frac{da}{dN} = \frac{\pi \Delta K_{eff}^4}{96 E \gamma \sigma_{yc}^2} \quad (12)$$

where

$$\Delta K_{eff} = \left[(\Delta K_I^2 + 3 \Delta K_{II}^2)^3 (\Delta K_I^2 + \Delta K_{II}^2) \right]^{\frac{1}{8}} \quad (13)$$

and

$$\frac{da}{dN} = \frac{\pi E}{96 \gamma} \left(\frac{1 + 3 R_\sigma^2}{1 + R_\sigma^2} \right)^{1.5} \frac{\Delta J^2}{\sigma_{yc}^2} \quad (14)$$

In these equations, γ is considered as the effective surface energy for fatigue crack growth, R_σ is the ratio of the applied shear stress to tensile stress range and σ_{yc} is the cyclic yield strength. Compared with experimental data, the results predicted by this model were thought to be reasonable by Chen and Keer [43].

(4) Equations using strain energy density

Sih and Barthelemy [27] thought the commonly used Paris law is not adequate for mixed-mode crack growth problems since loading parameters, say the stress amplitude and the mean stress level are not included in the equation and a crack does not grow in a self-similar manner under mixed-mode loads. They proposed to use the strain energy density factor concept to predict fatigue crack growth.

$$\frac{da}{dN} = C_s (\Delta S)^{n_s} \quad (15)$$

ΔS is the strain energy density factor range, and C_s and n_s are material constants.

By equating this equation with the Paris equation for mode I loading, the constants C_s and n_s in Eq. (15) can be found. The material constants thus obtained from the Paris equation are assumed not to be sensitive to the modes of loading in the regime of linear elastic fracture mechanics[16].

The strain energy density factor can be written as:

$$S = a_{11}k_1^2 + 2a_{12}k_1k_2 + a_{22}k_2^2 + a_{33}k_3^2 \quad (16)$$

where the coefficients a_{ij} ($i, j = 1, 2$) are given by:

$$\begin{aligned} 16\mu a_{11} &= (1 + \cos \theta)(\kappa - \cos \theta) \\ 16\mu a_{12} &= \sin \theta \{2 \cos \theta - (\kappa - 1)\} \\ 16\mu a_{22} &= (\kappa + 1)(1 - \cos \theta) + (1 + \cos \theta)(3 \cos \theta - 1) \\ 16\mu a_{33} &= 4 \end{aligned} \quad (17)$$

with $\kappa = 3 - 4\nu$ and $\kappa = (3 - \nu)/(1 + \nu)$ for plane strain and plane stress conditions. μ is the shear modulus of elasticity. The angle θ denotes the position of the radius vector and is measured from a line collinear with the crack. The k 's are defined as:

$$k_i = K_i / \sqrt{\pi} \quad (i = I, II, III) \quad (18)$$

where K_i are stress intensity factors for modes I, II and III, respectively.

From the definition of stress intensity factors in the linear elastic fracture mechanics, Δs can be expressed as

$$\Delta S = 2 \left[a_{11} \bar{k}_1 \Delta k_1 + a_{12} \left(\bar{k}_2 \Delta k_1 + \bar{k}_1 \Delta k_2 \right) + a_{22} \bar{k}_2 \Delta k_2 + a_{33} \bar{k}_3 \Delta k_3 \right] \quad (19)$$

where $\Delta S = S_{\max} - S_{\min}$, $\Delta k_j = (k_{\max})_j - (k_{\min})_j$ and $\bar{k}_j = \frac{1}{2}[(k_{\max})_j + (k_{\min})_j]$, $j = 1, 2, 3$

Lam [44] found that the strain energy density factor range ΔS is not compatible with the concept of crack closure and proposed a modification of the existing concept of ΔS based on the contact stress intensity factor concept developed by Lam and Williams [45].

$$\begin{aligned}\Delta S_{eff} &= \Delta S[1 - g(R)] \\ g(R) &= [f(R)/(1 + R)][(1 + R)f(R) - 2] + 2f(R)\end{aligned}\quad (20)$$

where $f(R)$ is a monotonic decreasing function with R .

Theocaris and Andrianopoulos [46] argued that since S is a summation of distortional and dilatational strain energy densities, these two fundamentally different physical quantities should not be added together. Also, S is defined along the boundary of the so-called core region, which is assumed to be circular. This assumption has not been justified yet. Yan et al. [47] suggest that the Nadai elastic-plastic boundary, which considers the different yield strengths in tension and compression, should be used as the boundary of this core region, rather than the assumed circle. Wu [48] pointed out that S is constant under pure antiplane loading condition (mode III) and the S -criterion fails to yield a preferred direction for this case. Wong [49] suggested that more terms in the Westergaard expressions of the stress field around the crack tip should be included in the S expression.

(5) Equations using CTD (crack tip displacement) or ΔJ

These equations are of the form similar to Paris law:

$$\frac{da}{dN} = C(\Delta CTD)^m \quad (21)$$

$$\frac{da}{dN} = \frac{4}{\pi\sigma_s E} \left[(\Delta K_I^2 + 3\Delta K_{II}^2) (\Delta K_I^2 + 2\Delta K_{II}^2 + 2\Delta K_I \Delta K_{II}) \right]^{1/2} \quad (22)$$

$$\frac{da}{dN} = C(\Delta J)^m \quad (23)$$

A “Vector Crack Tip Displacement” (CTD) criterion was proposed by Li [50]. The J-integral approach was suggested by Dowling and Begley [51]; Wuthrich [52]; Srivastava [53] and Chow and Lu [54]. This concept was extended to fatigue crack growth rate analyses of small cracks under mixed-mode loadings by Hoshide and Socie [55].

There are various criteria proposed in the literature for the calculation of effective mixed-mode stress intensity factor; some of them are reviewed here.

(1) Tanaka’s model

This model is based on the assumption that a fatigue crack grows when the sum of the absolute values of the displacements in a plastic strip reaches a critical value. Under mixed-mode conditions, it is assumed that deformations due to mode I and mode II loads are not interactive.

The following equation was proposed by Tanaka [56], who found the correlation obtained from the parameter expressed by this equation to provide the best fit for his experimental data.

$$\Delta K_{eff} = \left(\Delta K_I^4 + 8\Delta K_{II}^4 \right)^{1/4} \quad (24)$$

(2) Tong & Yan’s model

Tong et al. [47] suggested the following equation which was obtained by the maximum tangential stress criterion proposed by Erdogan and Sih [57].

$$\Delta K_{eff} = \frac{1}{2} \cos \frac{\theta_0}{2} [\Delta K_I (1 + \cos \theta_0) - 3 \Delta K_{II} \sin \theta_0] \quad (25)$$

where θ_0 is the crack growth direction obtained from the maximum tangential stress criterion. This model is a simple extension of the maximum tangential stress criterion to the case of mixed-mode fatigue crack growth. This model, however, lacks experimental verification.

(3) Richard's model

Richard [58] proposed an empirical model for the effective stress intensity factor estimation as

$$\left(\frac{K_I}{K_{IC}} \right) + \left(\xi \frac{K_{II}}{K_{IC}} \right)^2 = 1 \quad (26)$$

$$K_{eff} = \frac{1}{2} K_I + \frac{1}{2} \sqrt{K_I^2 + 4(\xi K_{II})^2} \quad (27)$$

where $\xi = \frac{K_{IC}}{K_{IIC}}$.

(4) Energy release rate model 1 [59]

This method calculates the effective stress intensity factor as

$$\Delta K_{eff} = \left(\Delta K_I^2 + \Delta K_{II}^2 + \frac{1}{1-\nu} \Delta K_{III}^2 \right)^{\frac{1}{2}} \quad (28)$$

where ν is the Poisson's ratio. Consider a local coordinate system at the crack front such that the x-axis lies in the plane of the crack and is normal to the crack front. In this case total energy release rate can be decomposed into the energy release rates for each fracture mode.

$$G = G_I + G_{II} + G_{III} \quad (29)$$

For linear elastic fracture mechanics, there exists a direct relationship between G_I , G_{II} , G_{III} and the stress intensity factors K_I , K_{II} , K_{III} , which is given by

$$\begin{Bmatrix} G_I \\ G_{II} \\ G_{III} \end{Bmatrix} = \frac{1}{E_{eff}} \begin{Bmatrix} K_I^2 \\ K_{II}^2 \\ E_{eff} K_{III}^2 / 2\mu \end{Bmatrix} \quad (30)$$

where E_{eff} is an effective modulus depending on the stress state at the crack tip.

$$E_{eff} = \begin{cases} \frac{E}{1-\nu^2} & \text{for plain strain} \\ E & \text{for plain stress} \end{cases} \quad (31)$$

$$\mu = E / 2(1+\nu) \quad (32)$$

Let

$$G = \frac{K_{eff}^2}{E_{eff}} \quad (33)$$

Then

$$K_{eff}^2 = K_I^2 + K_{II}^2 + K_{III}^2 / (1-\nu) \quad (34)$$

Thus, ΔK_{eff} for mode I and II is

$$\Delta K_{eff} = \left(\Delta K_I^2 + \Delta K_{II}^2 \right)^{\frac{1}{2}} \quad (35)$$

and ΔK_{eff} for mode I and III is

$$\Delta K_{eff} = \left(\Delta K_I^2 + \frac{1}{1-\nu} \Delta K_{III}^2 \right)^{\frac{1}{2}} \quad (36)$$

(5) Energy release rate model 2 [26]

This method calculates the effective stress intensity factor as

$$\Delta K_{eff} = \left(\Delta K_I^2 + \Delta K_{II}^2 + \Delta K_{III}^2 \right)^{\frac{1}{2}} \quad (37)$$

Note that Eq. (37) is obtained by substituting $\nu = 0$ in Eq. (28).

(6) Hänsel's model

Fatigue behavior of cold extrusion dies was studied by Hänsel et al, and the effective stress intensity factor was defined as

$$K_{eff} = \frac{1}{2} \left(K_I^2 + \left(4 \frac{K_{IC}}{K_{IIC}} K_{II} \right)^2 \right) \quad (38)$$

(7) Liu and Mahadevan's model

Liu and Mahadevan [60] developed a mixed-mode threshold stress intensity factor model using a characteristic plane based multiaxial fatigue theory and Kitagawa-Takahashi diagram [11].

$$\sqrt{\left(\frac{k_1}{K_{I,th}} \right)^2 + \left(\frac{k_2}{K_{II,th}} \right)^2 + \left(\frac{k_3}{K_{III,th}} \right)^2 + A \left(\frac{k^H}{K_{I,th}} \right)^2} = B \quad (39)$$

The effective stress intensity factor is defined by

$$\Delta K_{eff} = \frac{1}{B} \sqrt{(k_1)^2 + \left(\frac{k_2}{s} \right)^2 + \left(\frac{k_3}{s} \right)^2 + A \left(\frac{k^H}{s} \right)^2} \quad (40)$$

The characteristic plane adjusts its orientation according to mode mixity, which is a function of the ratio of mode I to mode II stress intensity factor, and material ductility s , which is the ratio of the shear fatigue limit to tensile fatigue limit, which makes this model superior to the previous ones. It is applicable to both metallic and composite materials, either shear or tension dominated crack growth, even for nonproportional fatigue loading. However, since this model is based on remote stress rather than local

stress, it cannot capture the geometric details near crack tip, which makes it not applicable for notched specimens.

2.3 Proposed mixed-mode I and II fatigue model

2.3.1 Multiaxial fatigue limit criterion

Liu and Mahadevan [9] proposed a characteristic-plane based model for multiaxial fatigue damage modeling and validated the model using bending-torsional fatigue experimental data. This model was combined with the Kitagawa-Takahashi diagram [11] and used to calculate near threshold equivalent mixed-mode stress intensity factor [60]. Different from most existing critical plane-based models, this method does not rely on the cracking mechanism, such as the crack growth orientations [9]. The characteristic plane in this model is only a material plane on which the stress/strain components are used to analyze the fatigue damage of materials. It arises from the idea of mathematical dimensional reduction rather than physical cracking observations. The method can be applied even without knowing the cracking mechanism, thus to both metallic and composite materials, even though the cracking mechanism for the two materials are fundamentally different [61]. However, since the fatigue damage is evaluated using remote stresses acting on the cracked component, this method can not capture the geometric details and complex stress field near crack tip. In the proposed study a local stress based characteristic plane approach is used to predict mixed-mode I and II stress intensity factor and fatigue crack growth rate.

The general fatigue limit criterion under multiaxial loading for mixed-mode I and II is expressed as

$$\sqrt{\left(\frac{\sigma_c}{f_{-1}}\right)^2 + \left(\frac{\tau_c}{t_{-1}}\right)^2 + A\left(\frac{\sigma_H}{f_{-1}}\right)^2} = B \quad (41)$$

where σ_c and τ_c are the normal stress amplitude and shear stress amplitude acting on the characteristic plane, respectively. σ_H is the hydrostatic stress amplitude. A and B are material parameters which can be determined by tensional and torsional fatigue limits. A detailed derivation and explanation of the model can be found in Liu and Mahadevan [9].

2.3.2 Fatigue limit and threshold stress intensity factor

The concept of fatigue limit is traditionally used within the fatigue resistance design approach, which defines a loading criterion under which no macroscopic crack will form. The concept of threshold stress intensity factor is often used within the damage tolerant design approach, which defines a loading criterion under which the cracks will not grow significantly [62]. A link between the fatigue limit and the threshold stress intensity factor was proposed by Kitagawa and Takahashi [11]. The fatigue limit against the crack size using Kitagawa-Takahashi diagram is shown in Figure 1.

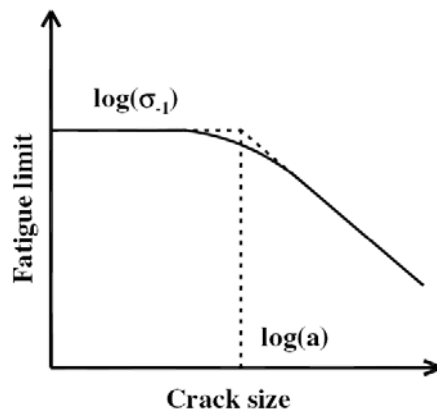


Figure 1. Kitagawa diagram for fatigue limits and threshold stress intensity factor

According to the well-known El Haddad model [63], the fatigue limit can be expressed using the threshold stress intensity factor and a fictional crack length a . The crack length a represents the intersection of the smooth specimen fatigue limit and the linear elastic fracture mechanics (LEFM) threshold stress intensity factor, i.e.,

$$f_{-1} = \frac{K_{I,th}}{\sqrt{\pi a}} \quad t_{-1} = \frac{K_{II,th}}{\sqrt{\pi a}} \quad (42)$$

where f_{-1} and t_{-1} are normal and shear fatigue limit, respectively and $K_{I,th}$ and $K_{II,th}$ are the threshold stress intensity factors for mode I and mode II, respectively.

2.3.3 Mixed-mode I and II threshold stress intensity factor

The multiaxial fatigue limit criterion can be extended to a mixed-mode threshold stress intensity factor criterion using Kitagawa-Takahashi diagram [11], which links the fatigue behavior of cracked and noncracked material together. Consider an infinite plate under remote tensional and torsional loading as shown in Figure 2, there is a mixed-mode I and II stress field near crack tip, which can be expressed as:

$$\begin{aligned} \sigma_{rr} &= \frac{1}{\sqrt{2\pi r}} \cos\left(\frac{\theta}{2}\right) \left[K_I \left(1 + \sin^2\left(\frac{\theta}{2}\right) \right) + K_{II} \left(\frac{3}{2} \sin(\theta) - 2 \tan\left(\frac{\theta}{2}\right) \right) \right] \\ \sigma_{\theta\theta} &= \frac{1}{\sqrt{2\pi r}} \cos\left(\frac{\theta}{2}\right) \left[K_I \cos^2\left(\frac{\theta}{2}\right) - \frac{3}{2} K_{II} \sin(\theta) \right] \\ \sigma_{zz} &= \begin{cases} 0 & \text{plane stress} \\ \nu(\sigma_{\theta\theta} + \sigma_{rr}) & \text{plane strain} \end{cases} \\ \tau_{r\theta} &= \frac{1}{2\sqrt{2\pi r}} \cos\left(\frac{\theta}{2}\right) \left[K_I \sin(\theta) + K_{II} (3 \cos(\theta) - 1) \right] \end{aligned} \quad (43)$$

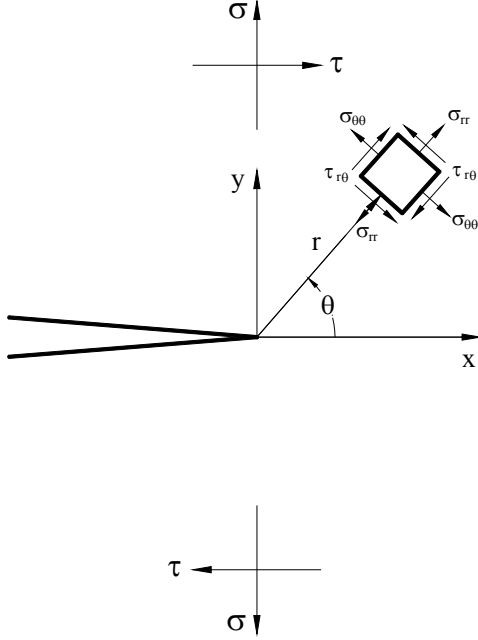


Figure 2. Mixed-mode I and II stress fields near crack tip

For plane stress condition, Eq. (41) can be rewritten as

$$\sqrt{\left(\frac{\sigma_{\theta\theta}}{f_{-1}}\right)^2 + \left(\frac{\tau_{r\theta}}{t_{-1}}\right)^2 + A\left(\frac{\sigma_{\theta\theta} + \sigma_{rr}}{3f_{-1}}\right)^2} = B \quad (44)$$

For plane strain condition, Eq. (41) can be rewritten as

$$\sqrt{\left(\frac{\sigma_{\theta\theta}}{f_{-1}}\right)^2 + \left(\frac{\tau_{r\theta}}{t_{-1}}\right)^2 + A(1+\nu)^2\left(\frac{\sigma_{\theta\theta} + \sigma_{rr}}{3f_{-1}}\right)^2} = B \quad (45)$$

To unify the multiaxial fatigue limit criteria for both plane stress and plane strain condition, a new parameter A^* is introduced which is the same as A under plane stress condition and equals to $A(1+\nu)^2$ under plane strain condition. Thus Eq. (41) can be expressed as

$$\sqrt{\left(\frac{\sigma_{\theta\theta}}{f_{-1}}\right)^2 + \left(\frac{\tau_{r\theta}}{t_{-1}}\right)^2 + A^* \left(\frac{\sigma_{\theta\theta} + \sigma_{rr}}{3f_{-1}}\right)^2} = B \quad (46)$$

To determine the parameters A^* and B , two extreme cases are considered below:

Case 1: For a fully reversed pure tensional fatigue experiment, the ranges of mode I and mode II stress intensity factors are shown as

$$\begin{aligned} K_I &= f_{-1} \sqrt{2\pi r_c} \\ K_{II} &= 0 \end{aligned} \quad (47)$$

where r_c is the characteristic or characteristic distance. From Eq. (43) the stress field near crack tip can be rewritten as

$$\begin{aligned} \sigma_{rr} &= f_{-1} \cos\left(\frac{\theta}{2}\right) \left(1 + \sin^2\left(\frac{\theta}{2}\right)\right) \\ \sigma_{\theta\theta} &= f_{-1} \cos^3\left(\frac{\theta}{2}\right) \\ \tau_{r\theta} &= \frac{1}{2} f_{-1} \cos\left(\frac{\theta}{2}\right) \sin(\theta) \end{aligned} \quad (48)$$

Assume $\xi = t_{-1} / f_{-1}$, Eq. (46) can be expressed as

$$\sqrt{\cos^6\left(\frac{\theta}{2}\right) + \left(\frac{1}{2} \frac{1}{\xi} \cos\left(\frac{\theta}{2}\right) \sin(\theta)\right)^2 + A^* \left(\frac{2}{3} \cos\left(\frac{\theta}{2}\right)\right)^2} = B \quad (49)$$

Case 2: For a fully reversed pure torsion fatigue experiment, the ranges of mode I and mode II stress intensity factors are shown as

$$\begin{aligned} K_I &= 0 \\ K_{II} &= t_{-1} \sqrt{2\pi r_c} \end{aligned} \quad (50)$$

From Eq. (43) the stress field near crack tip can be rewritten as

$$\begin{aligned}
\sigma_{rr} &= t_{-1} \cos\left(\frac{\theta}{2}\right) \left(\frac{3}{2} \sin(\theta) - 2 \tan\left(\frac{\theta}{2}\right) \right) \\
\sigma_{\theta\theta} &= -\frac{3}{2} t_{-1} \cos\left(\frac{\theta}{2}\right) \sin(\theta) \\
\tau_{r\theta} &= \frac{1}{2} t_{-1} \cos\left(\frac{\theta}{2}\right) (3 \cos(\theta) - 1)
\end{aligned} \tag{51}$$

Thus Eq. (46) can be expressed as

$$\sqrt{\left(-\frac{3}{2} \xi \cos\left(\frac{\theta}{2}\right) \sin(\theta)\right)^2 + \left(\frac{1}{2} \cos\left(\frac{\theta}{2}\right) (3 \cos(\theta) - 1)\right)^2} + A^* \left(-\frac{2}{3} \xi \sin\left(\frac{\theta}{2}\right)\right)^2 = B \tag{52}$$

According to the maximum tangential stress criterion (MTS), the maximum tangential stress at r_c occurs at the angle of β , which satisfies

$$\left. \frac{\partial \sigma_{\theta\theta}}{\partial \theta} \right|_{\theta=\beta} = 0 \quad \left. \frac{\partial^2 \sigma_{\theta\theta}}{\partial \theta^2} \right|_{\theta=\beta} < 0 \tag{53}$$

Thus for case 1, $\beta = 0^\circ$ and for case 2, $\beta = -70.529^\circ$. Solving for A^* and B as

$$\begin{aligned}
A^* &= \frac{9\left(\xi^2 - \frac{3}{4}\right)}{3 - \xi^2} \\
B &= \sqrt{\frac{3\xi^2}{3 - \xi^2}}
\end{aligned} \tag{54}$$

Since A^* is the contribution of damage caused by the hydrostatic stress, A^* and B should be non negative real number. The range of ξ need to be

$$\sqrt{3}/2 \leq \xi < \sqrt{3} \tag{55}$$

For most brittle materials, ξ is greater than 1. Thus the characteristic plane orientation calculated by MTS criterion is only applicable to brittle material.

According to the maximum shear stress criterion (MSS), the maximum shear stress at r_c occurs at the angle β , which satisfies

$$\left. \frac{\partial \tau_{r\theta}}{\partial \theta} \right|_{\theta=\beta} = 0 \quad \left. \frac{\partial^2 \tau_{r\theta}}{\partial \theta^2} \right|_{\theta=\beta} < 0 \quad (56)$$

Thus for case 1, $\beta = 70.529^\circ$ and for case 2, $\beta = 0^\circ$. Solving for A^* and B ,

$$A^* = \frac{19\xi^2 - 4}{8\xi^2} \quad (57)$$

$$B = 1$$

Since A^* and B should be non negative real numbers, the range of ξ needs to be

$$\xi \geq 2/\sqrt{19} \quad (58)$$

Thus the characteristic plane orientation calculated by the MSS criterion has a wider application range than by the MTS criterion, and is applicable for both brittle and ductile materials. In these two extreme cases (case 1 and case 2) the characteristic plane orientations coincide with the crack orientations predicted by MSS. Therefore the MSS criterion is used below to predict crack orientation β .

The contribution of the hydrostatic stress is different for different materials if the characteristic plane is fixed for all materials. There are two materials: $\xi = \sqrt{3}/2$ by MTS criterion and $\xi = 2/\sqrt{19}$ by MSS criterion, for which the contribution of hydrostatic stress is zero. It is also noticed that, if the characteristic plane is fixed, the range of applicable material parameters are limited.

Instead of fixing the characteristic plane, the current model searches for the characteristic plane orientations on which the contribution of the hydrostatic stress is minimized to zero.

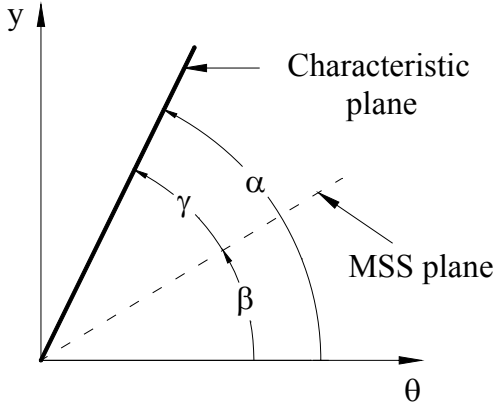


Figure 3. Orientation of characteristic plane and maximum shear stress (MSS) plane

For an arbitrary material, the characteristic plane orientation is assumed to be α (as shown in Figure 3). Since the contribution of the hydrostatic stress is zero, Eq. (46) is rewritten as:

$$\sqrt{\left(\frac{\sigma_{\theta\theta,\alpha}}{f_{-1}}\right)^2 + \left(\frac{\tau_{r\theta,\alpha}}{t_{-1}}\right)^2} = B \quad (59)$$

The objective is to find α and B for an arbitrary material, following the steps described for the first two cases, Eq. (49) and (52) can be rewritten as

$$\sqrt{\cos^6\left(\frac{\theta_1 + \gamma}{2}\right) + \left(\frac{1}{2} \frac{1}{\xi} \cos\left(\frac{\theta_1 + \gamma}{2}\right) \sin(\theta_1 + \gamma)\right)^2} = B \quad (60)$$

$$\sqrt{\left(-\frac{3}{2} \xi \cos\left(\frac{\theta_2 + \gamma}{2}\right) \sin(\theta_2 + \gamma)\right)^2 + \left(\frac{1}{2} \cos\left(\frac{\theta_2 + \gamma}{2}\right) (3 \cos(\theta_2 + \gamma) - 1)\right)^2} = B \quad (61)$$

where $\theta_1 = 70.529^\circ$ and $\theta_2 = 0^\circ$.

It is difficult to obtain a closed form solution for Eqs. (60) and (61). Numerical solutions for γ and B versus material property ξ are shown in Figure 4 and Figure 5. For $\xi \leq \sqrt{3}/2$, effects of hydrostatic stress can be reduced to zero by rotating the characteristic plane from the MSS plane by an angle γ . As ξ increases from $2/\sqrt{19}$ to $\sqrt{3}/2$, material property changes from ductile to brittle, also the characteristic plane orientation changes from MSS plane to MTS plane. For $\xi > \sqrt{3}/2$, which indicate the extremely brittle materials, the contribution of hydrostatic stress cannot be minimized to zero and must be considered during the fatigue damage evaluation. In this case the characteristic plane has the same orientation as the MSS plane and the parameters A^* and B are calculated using Eq. (57).

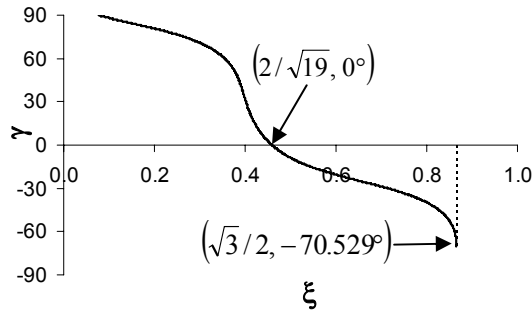


Figure 4. γ .vs. ξ for mixed-mode I+II

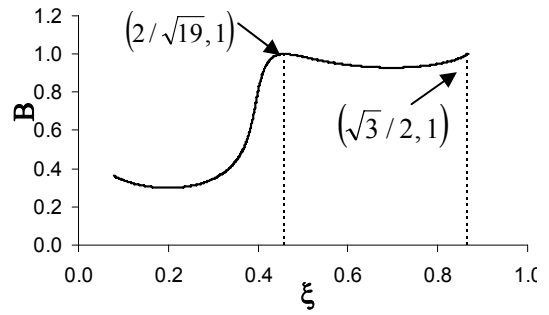


Figure 5. B .vs. ξ for mixed-mode I+II

The mixed-mode I and II crack orientation β can be solved from the MSS criterion using Eq. (56). The numerical solution is shown in Figure 6.

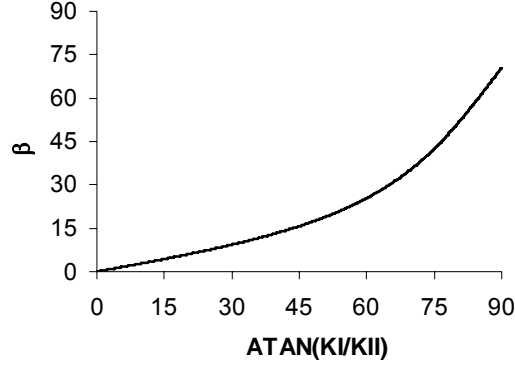


Figure 6. Mixed-mode I+II crack orientation β using the MSS criterion

Then the characteristic plane orientation α can be expressed as

$$\alpha = \beta + \gamma \quad (62)$$

In the proposed method, the characteristic plane depends on mode mixity ϕ , where $\tan \phi$ equals to the ratio of stress intensity factor K_I / K_{II} , and material ductility ξ . The parameter ξ is related to two different material failure mechanisms. A larger value of ξ ($\xi \geq \sqrt{3}/2$) indicates tensional dominated failure and smaller ξ ($\xi < \sqrt{3}/2$) indicates shear-dominated failure. If the value of ξ is known (based on uniaxial and pure torsional fatigue tests), the proposed model can automatically adapt for different failure mechanism.

2.3.4 Mixed-mode I and II fatigue crack growth

Using the parameter α , Eq. (46) becomes

$$\sqrt{\left(\frac{\cos\left(\frac{\alpha}{2}\right) \left[K_I \cos^2\left(\frac{\alpha}{2}\right) - \frac{3}{2} K_{II} \sin(\alpha) \right]}{K_{I,th}} \right)^2 + \left(\frac{\frac{1}{2} \cos\left(\frac{\alpha}{2}\right) \left[K_I \sin(\alpha) + K_{II} (3 \cos(\alpha) - 1) \right]}{\xi K_{I,th}} \right)^2 + A \left(\frac{2 \cos\left(\frac{\alpha}{2}\right) \left[K_I - K_{II} \tan\left(\frac{\alpha}{2}\right) \right]}{3 K_{I,th}} \right)^2} = B \quad (63)$$

For prediction corresponding to a general crack growth rate da / dN , the threshold stress intensity factors ($K_{I,th}$ and $K_{II,th}$) may be replaced by the stress intensity

coefficients at the specific crack growth rate ($K_{I,da/dN}$ and $K_{II,da/dN}$). In the proposed mixed-mode crack growth model, stress intensity coefficients at the specific crack growth rates are considered as equivalent stress intensity factor for mixed-mode case. The mixed-mode crack growth model is expressed as

$$K_{mix,eq} = \frac{\left| \cos\left(\frac{\alpha}{2}\right) \right|}{B} \sqrt{\left(K_I \cos^2\left(\frac{\alpha}{2}\right) - \frac{3}{2} K_{II} \sin(\alpha) \right)^2 + \frac{1}{4g^2} (K_I \sin(\alpha) + K_{II} (3 \cos(\alpha) - 1))^2 + \frac{4}{9} A \left(K_I - K_{II} \tan\left(\frac{\alpha}{2}\right) \right)^2} = K_{I,da/dN} = f\left(\frac{da}{dN}\right) \quad (64)$$

where $f\left(\frac{da}{dN}\right)$ is the crack growth curve obtained under mode I loading. There are no closed form solutions for Eq.(64). In practical calculation, a trial and error method can be used to find da/dN . For high cycle fatigue problem, $K_{II,da/dN}$ and $K_{I,da/dN}$ take initial values as $K_{II,th}$ and $K_{I,th}$, respectively. It is found that usually a few iterations are enough to make N_f converge.

2.3.5 Experimental validation

Seven sets of fatigue experimental data available in the literature are employed in this section and listed in Table 1. The predicted thresholds and the experimental observations are plotted in Figure 7 where the x -axis and the y -axis are the applied stress intensity ranges for mode I and mode II, respectively. All values are normalized using the mode I threshold stress intensity factor. For comparison, the predictions using remote stress condition [60], the maximum strain energy release rate [26], MTS [64] and the minimum strain energy density [27] are also plotted in Figure 7. As shown in Figure 7, the predicted values using the proposed method agree with experimental observations much better than the existing four models.

Table 1. Experimental threshold SIF data used for model validation

Material name	References	Loading case	$K_{I,th} (Mpa\sqrt{m})$	ξ
6061Al	[65]	I + II	3.90	0.55
7075-T6 Aluminum alloy	[66]	I + II	1.60	0.64
316 Stainless steel	[33]	I + II	5.81	0.70
Aluminum alloy	[67]	I + II	2.75	0.83
2017-T3 Aluminum alloy	[66]	I + II	1.60	0.90
2024Al	[68]	I + II	3.90	1.46
SiCp/2024Al composite	[68]	I + II	4.80	1.79

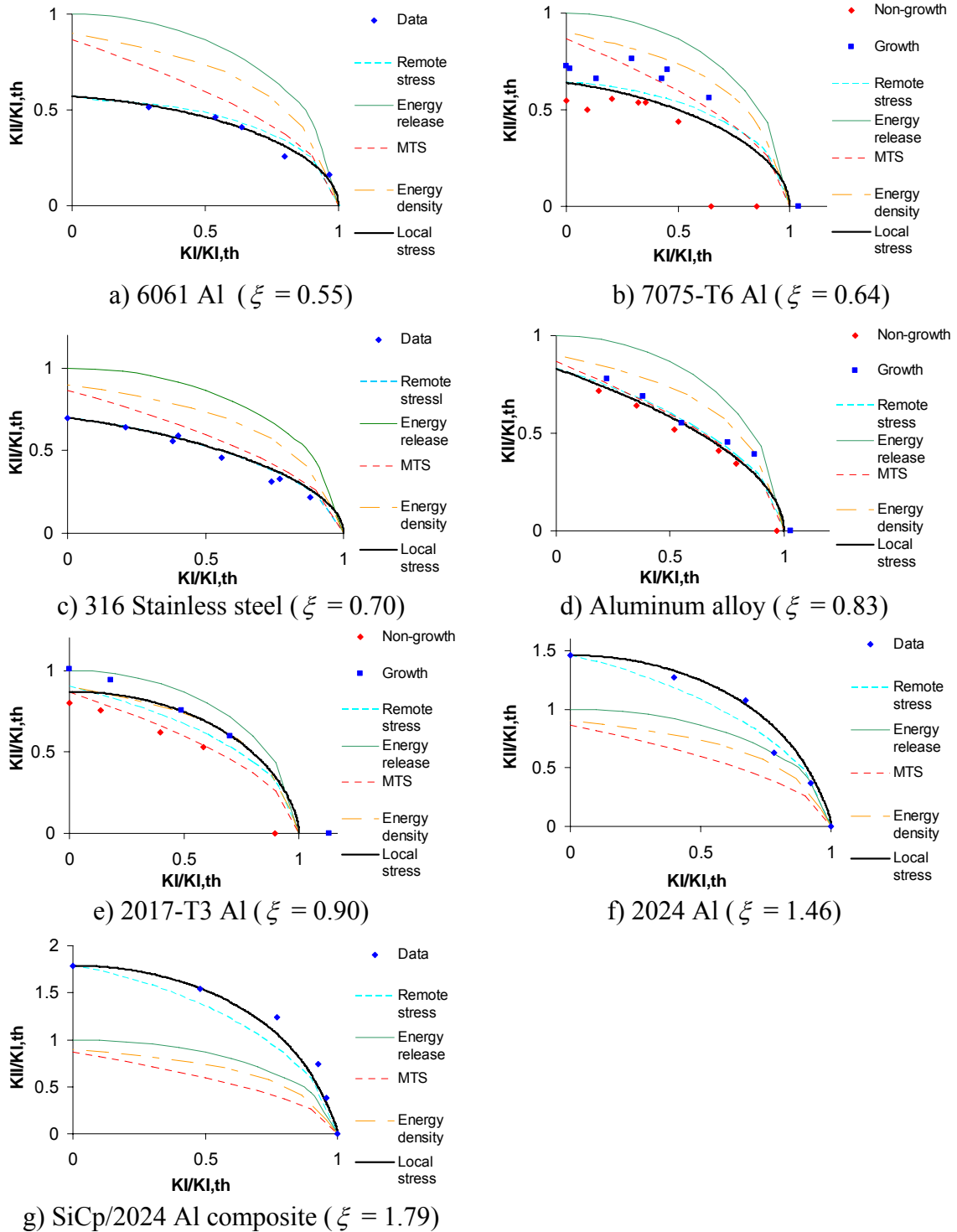
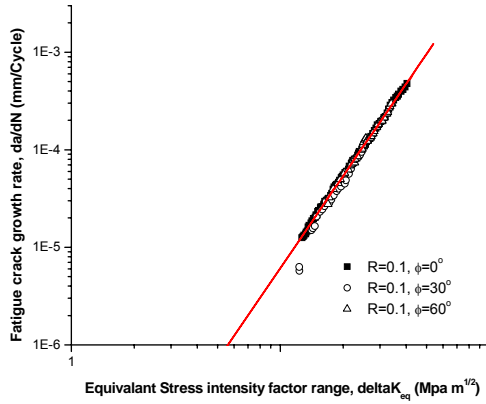
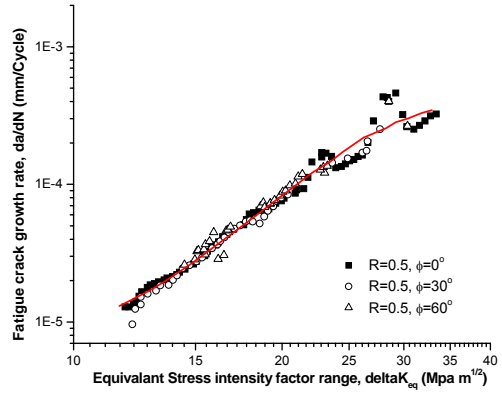


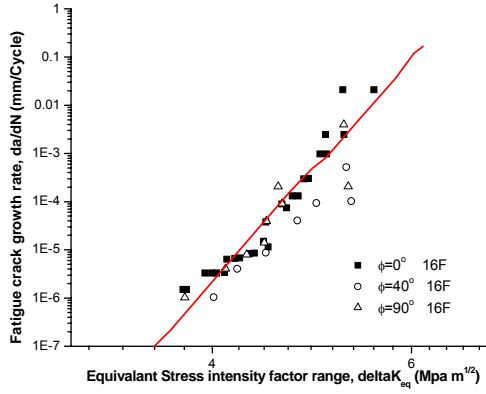
Figure 7. Comparisons of predicted and experimental threshold stress intensity factors for mixed-mode I+II



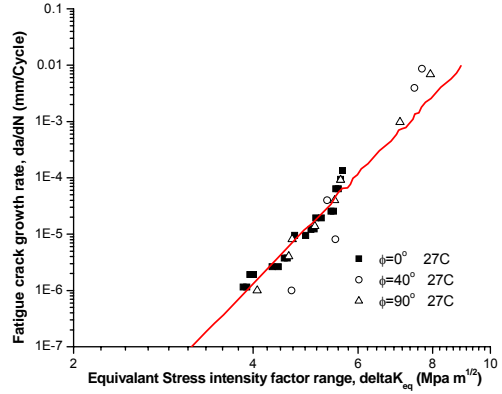
(a) rail steel, R = 0.1



(b) rail steel, R = 0.5



(c) WC-Co cemented carbides 16F



(d) WC-Co cemented carbides 27C

Figure 8. Comparisons of predicted and experimental fatigue crack growth rates

Two sets of fatigue experimental data are employed for the comparisons of fatigue crack growth rates, which are listed in Table 2. The predicted crack growth rates and experimental observations are plotted in Figure 8. In Figure 8, the x -axis is the equivalent applied stress intensity range (Eq.(64)) under mixed-mode loading. The y -axis is the fatigue crack growth rate. Different types of mixed-mode loading are represented using an angle ϕ , as listed in the legends for Figure 8 (a)–(d). The angle ϕ is defined as

$$\phi = \tan^{-1}(K_I / K_{II}) \quad (65)$$

ϕ is 90° for mode I loading and 0° for mode II loading. Predictions of the proposed model, shown as solid lines in Figure 8, correlate different types of mixed-mode crack growth rates using the mode I crack growth function.

Table 2. Experimental crack growth rate data used for model validation

Material name	References	Loading case	Mode mixity ϕ (deg)
Rail steel	[36]	I + II	0, 30, 60
WC-Co cemented carbides	[69]	I + II	0, 40, 90

2.4 Proposed mixed-mode I and III fatigue model

2.4.1 Mixed-mode I and III threshold stress intensity factor

Consider an infinite plate under remote normal and out of plane shear stress as shown in Figure 9. The mixed-mode I and III stress field near crack tip can be expressed as:

$$\begin{aligned}
\sigma_{rr} &= \frac{K_I}{\sqrt{2\pi r}} \cos\left(\frac{\theta}{2}\right) \left(1 + \sin^2\left(\frac{\theta}{2}\right)\right) \\
\sigma_{\theta\theta} &= \frac{K_I}{\sqrt{2\pi r}} \cos^3\left(\frac{\theta}{2}\right) \\
\sigma_{zz} &= \begin{cases} 0 & \text{plane stress} \\ \nu(\sigma_{\theta\theta} + \sigma_{rr}) = 2\nu \frac{K_I}{\sqrt{2\pi r}} \cos\left(\frac{\theta}{2}\right) & \text{plane strain} \end{cases} \\
\tau_{r\theta} &= \frac{K_I}{2\sqrt{2\pi r}} \cos\left(\frac{\theta}{2}\right) \sin(\theta) \\
\tau_{rz} &= \frac{K_{III}}{\sqrt{2\pi r}} \sin\left(\frac{\theta}{2}\right) \\
\tau_{\theta z} &= \frac{K_{III}}{\sqrt{2\pi r}} \cos\left(\frac{\theta}{2}\right)
\end{aligned} \tag{66}$$

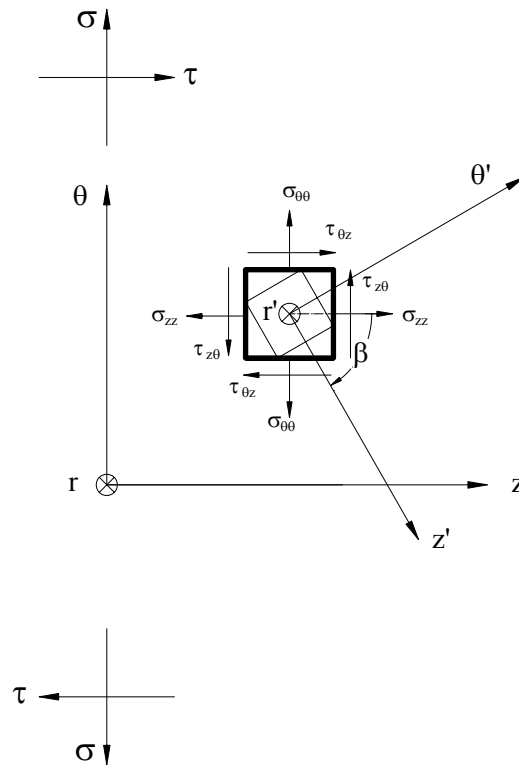


Figure 9. Mixed-mode I and III stress fields near crack tip

The general fatigue limit criterion under multiaxial loading for mixed-mode I and III is expressed as

$$\sqrt{\left(\frac{\sigma_c}{f_{-1}}\right)^2 + \left(\frac{\tau_c}{t_{-1}}\right)^2 + A\left(\frac{\sigma^H}{f_{-1}}\right)^2} = B \quad (67)$$

where σ_c and τ_c are the normal stress amplitude and out of plane shear stress amplitude acting on the characteristic plane, respectively. σ^H is the hydrostatic stress amplitude. A and B are material parameters which can be determined by tensional and torsional fatigue limits.

Experimental data shows that the failure surface under mixed mode I and III loading condition is typically non-planar. Assume coordinate (r, θ, z) rotates β around axis r to coordinate (r', θ', z') , the stress in the new coordinate can be expressed as

$$\begin{aligned} \sigma_{r'r'} &= \sigma_{rr} \\ \sigma_{\theta'\theta'} &= \frac{\sigma_{\theta\theta} + \sigma_{zz}}{2} + \frac{\sigma_{\theta\theta} - \sigma_{zz}}{2} \cos(2\beta) + \tau_{\theta z} \sin(2\beta) \\ \sigma_{z'z'} &= \frac{\sigma_{\theta\theta} + \sigma_{zz}}{2} - \frac{\sigma_{\theta\theta} - \sigma_{zz}}{2} \cos(2\beta) - \tau_{\theta z} \sin(2\beta) \\ \tau_{r'\theta'} &= \tau_{r\theta} \cos(\beta) + \tau_{rz} \sin(\beta) \\ \tau_{r'z'} &= -\tau_{r\theta} \sin(\beta) + \tau_{rz} \cos(\beta) \\ \tau_{\theta'z'} &= -\frac{\sigma_{\theta\theta} - \sigma_{zz}}{2} \sin(2\beta) + \tau_{\theta z} \cos(2\beta) \end{aligned} \quad (68)$$

Under plane strain condition, Eq. (68) can be expressed as

$$\begin{aligned}
\sigma_{r'r'} &= \frac{1}{\sqrt{2\pi r}} \cos\left(\frac{\theta}{2}\right) \left[K_I \left(1 + \sin^2\left(\frac{\theta}{2}\right) \right) \right] \\
\sigma_{\theta'\theta'} &= \frac{1}{\sqrt{2\pi r}} \cos\left(\frac{\theta}{2}\right) \left[K_I \left(\cos^2\left(\frac{\theta}{2}\right) \cos^2(\beta) + 2\nu \sin^2(\beta) \right) + K_{III} \sin(2\beta) \right] \\
\sigma_{z'z'} &= \frac{1}{\sqrt{2\pi r}} \cos\left(\frac{\theta}{2}\right) \left[K_I \left(\cos^2\left(\frac{\theta}{2}\right) \sin^2(\beta) + 2\nu \cos^2(\beta) \right) - K_{III} \sin(2\beta) \right] \\
\tau_{r'\theta'} &= \frac{1}{\sqrt{2\pi r}} \left[\frac{1}{2} K_I \cos\left(\frac{\theta}{2}\right) \sin(\theta) \cos(\beta) + K_{III} \sin\left(\frac{\theta}{2}\right) \sin(\beta) \right] \\
\tau_{r'z'} &= \frac{1}{\sqrt{2\pi r}} \left[-\frac{1}{2} K_I \cos\left(\frac{\theta}{2}\right) \sin(\theta) \sin(\beta) + K_{III} \sin\left(\frac{\theta}{2}\right) \cos(\beta) \right] \\
\tau_{\theta'z'} &= \frac{1}{\sqrt{2\pi r}} \cos\left(\frac{\theta}{2}\right) \left[K_I \left(\nu - \frac{1}{2} \cos^2\left(\frac{\theta}{2}\right) \right) \sin(2\beta) + K_{III} \cos(2\beta) \right]
\end{aligned} \tag{69}$$

Under plane stress condition, Eq. (68) can be expressed as

$$\begin{aligned}
\sigma_{r'r'} &= \frac{1}{\sqrt{2\pi r}} \cos\left(\frac{\theta}{2}\right) \left[K_I \left(1 + \sin^2\left(\frac{\theta}{2}\right) \right) \right] \\
\sigma_{\theta'\theta'} &= \frac{1}{\sqrt{2\pi r}} \cos\left(\frac{\theta}{2}\right) \left[K_I \cos^2\left(\frac{\theta}{2}\right) \cos^2(\beta) + K_{III} \sin(2\beta) \right] \\
\sigma_{z'z'} &= \frac{1}{\sqrt{2\pi r}} \cos\left(\frac{\theta}{2}\right) \left[K_I \cos^2\left(\frac{\theta}{2}\right) \sin^2(\beta) - K_{III} \sin(2\beta) \right] \\
\tau_{r'\theta'} &= \frac{1}{\sqrt{2\pi r}} \left[\frac{1}{2} K_I \cos\left(\frac{\theta}{2}\right) \sin(\theta) \cos(\beta) + K_{III} \sin\left(\frac{\theta}{2}\right) \sin(\beta) \right] \\
\tau_{r'z'} &= \frac{1}{\sqrt{2\pi r}} \left[-\frac{1}{2} K_I \cos\left(\frac{\theta}{2}\right) \sin(\theta) \sin(\beta) + K_{III} \sin\left(\frac{\theta}{2}\right) \cos(\beta) \right] \\
\tau_{\theta'z'} &= \frac{1}{\sqrt{2\pi r}} \cos\left(\frac{\theta}{2}\right) \left[-\frac{1}{2} K_I \cos^2\left(\frac{\theta}{2}\right) \sin(2\beta) + K_{III} \cos(2\beta) \right]
\end{aligned} \tag{70}$$

Thus for mixed mode I and III under both plane strain and plane stress condition, the fatigue limit criterion becomes

$$\sqrt{\left(\frac{\sigma_{\theta'\theta'}}{f_{-1}}\right)^2 + \left(\frac{\tau_{r'\theta'}}{t_{-1}}\right)^2 + \left(\frac{\tau_{\theta'z'}}{t_{-1}}\right)^2} + A \left(\frac{\sigma_{\theta'\theta'} + \sigma_{z'z'} + \sigma_{r'r'}}{3f_{-1}}\right)^2 = B \tag{71}$$

where $-\pi \leq \theta \leq \pi$ and $-\pi/2 \leq \beta \leq \pi/2$. To determine the parameters A and B , two extreme cases are considered below:

Case 1: For a fully reversed pure tensional fatigue experiment

$$\begin{aligned} K_I &= f_{-1} \sqrt{2\pi r_c} \\ K_{III} &= 0 \end{aligned} \quad (72)$$

where r_c is the characteristic distance. From Eq. (69), (70) and (72) the stress fields near crack tip can be rewritten as below

Under plane strain condition:

$$\begin{aligned} \sigma_{r'r'} &= f_{-1} \cos\left(\frac{\theta}{2}\right) \left(1 + \sin^2\left(\frac{\theta}{2}\right)\right) \\ \sigma_{\theta'\theta'} &= f_{-1} \cos\left(\frac{\theta}{2}\right) \left(\cos^2\left(\frac{\theta}{2}\right) \cos^2(\beta) + 2\nu \sin^2(\beta)\right) \\ \sigma_{z'z'} &= f_{-1} \cos\left(\frac{\theta}{2}\right) \left(\cos^2\left(\frac{\theta}{2}\right) \sin^2(\beta) + 2\nu \cos^2(\beta)\right) \\ \tau_{r'\theta'} &= \frac{1}{2} f_{-1} \cos\left(\frac{\theta}{2}\right) \sin(\theta) \cos(\beta) \\ \tau_{r'z'} &= -\frac{1}{2} f_{-1} \cos\left(\frac{\theta}{2}\right) \sin(\theta) \sin(\beta) \\ \tau_{\theta'z'} &= f_{-1} \cos\left(\frac{\theta}{2}\right) \left(\nu - \frac{1}{2} \cos^2\left(\frac{\theta}{2}\right)\right) \sin(2\beta) \end{aligned} \quad (73)$$

Under plane stress condition:

$$\begin{aligned} \sigma_{r'r'} &= f_{-1} \cos\left(\frac{\theta}{2}\right) \left(1 + \sin^2\left(\frac{\theta}{2}\right)\right) \\ \sigma_{\theta'\theta'} &= f_{-1} \cos^3\left(\frac{\theta}{2}\right) \cos^2(\beta) \\ \sigma_{z'z'} &= f_{-1} \cos^3\left(\frac{\theta}{2}\right) \sin^2(\beta) \\ \tau_{r'\theta'} &= \frac{1}{2} f_{-1} \cos\left(\frac{\theta}{2}\right) \sin(\theta) \cos(\beta) \\ \tau_{r'z'} &= -\frac{1}{2} f_{-1} \cos\left(\frac{\theta}{2}\right) \sin(\theta) \sin(\beta) \\ \tau_{\theta'z'} &= -\frac{1}{2} f_{-1} \cos^3\left(\frac{\theta}{2}\right) \sin(2\beta) \end{aligned} \quad (74)$$

Assuming $\xi = t_{-1} / f_{-1}$, Eq. (71) can be expressed as

Under plane strain condition:

$$\left| \cos\left(\frac{\theta}{2}\right) \right| \sqrt{\left(\cos^2\left(\frac{\theta}{2}\right) \cos^2(\beta) + 2\nu \sin^2(\beta) \right)^2 + \left(\frac{\sin(\theta) \cos(\beta)}{2\xi} \right)^2 + \left(\frac{\left(\nu - \frac{1}{2} \cos^2\left(\frac{\theta}{2}\right) \right) \sin(2\beta)}{\xi} \right)^2} + A \frac{4}{9} (1+\nu)^2 = B \quad (75)$$

Under plane stress condition:

$$\left| \cos\left(\frac{\theta}{2}\right) \right| \sqrt{\left(\cos^2\left(\frac{\theta}{2}\right) \cos^2(\beta) \right)^2 + \left(\frac{\sin(\theta) \cos(\beta)}{2\xi} \right)^2 + \left[\frac{1}{2\xi} \sin(2\beta) \cos^2\left(\frac{\theta}{2}\right) \right]^2} + A \frac{4}{9} = B \quad (76)$$

Case 2: For a fully reversed pure torsion fatigue experiment

$$\begin{aligned} K_I &= 0 \\ K_{III} &= t_{-1} \sqrt{2\pi r_c} \end{aligned} \quad (77)$$

From Eq. (69), (70) and (77) the stress fields near crack tip can be rewritten as

$$\begin{aligned} \sigma_{r'r'} &= 0 \\ \sigma_{\theta'\theta'} &= t_{-1} \cos\left(\frac{\theta}{2}\right) \sin(2\beta) \\ \sigma_{z'z'} &= -t_{-1} \cos\left(\frac{\theta}{2}\right) \sin(2\beta) \\ \tau_{r'\theta'} &= t_{-1} \sin\left(\frac{\theta}{2}\right) \sin(\beta) \\ \tau_{r'z'} &= t_{-1} \sin\left(\frac{\theta}{2}\right) \cos(\beta) \\ \tau_{\theta'z'} &= t_{-1} \cos\left(\frac{\theta}{2}\right) \cos(2\beta) \end{aligned} \quad (78)$$

Thus Eq. (71) can be expressed as

$$\sqrt{\left(\xi \cos\left(\frac{\theta}{2}\right) \sin(2\beta) \right)^2 + \left(\sin\left(\frac{\theta}{2}\right) \sin(\beta) \right)^2 + \left(\cos\left(\frac{\theta}{2}\right) \cos(2\beta) \right)^2} = B \quad (79)$$

According to the maximum tangential stress criterion (MTS), the maximum tangential stress at r_c occurs at the angel of θ , which satisfies

$$\frac{\partial \sigma_{\theta\theta'}}{\partial \beta} = 0 \quad \frac{\partial \sigma_{\theta\theta'}}{\partial \theta} = 0 \quad \frac{\partial^2 \sigma_{\theta\theta'}}{\partial \beta^2} < 0 \quad \frac{\partial^2 \sigma_{\theta\theta'}}{\partial \beta^2} \frac{\partial^2 \sigma_{\theta\theta'}}{\partial \theta^2} - \left(\frac{\partial^2 \sigma_{\theta\theta'}}{\partial \beta \partial \theta} \right)^2 > 0 \quad (80)$$

Thus in case 1 under plane strain condition, $\beta = 0$ and $\theta = 0$ at $\nu < 0.5$ and under plane stress condition, $\beta = 0$ and $\theta = 0$. Then Eq. (75) for plane strain can be rewritten as:

$$\sqrt{1 + A \frac{4}{9} (1 + \nu)^2} = B \quad (81)$$

Eq. (76) for plane stress can be rewritten as:

$$\sqrt{1 + \frac{4}{9} A} = B \quad (82)$$

In case 2, $\beta = \pi/4$ and $\theta = 0$ for both plane strain and plane stress. Then Eq. (79) can be rewritten as

$$\xi = B \quad (83)$$

Solving Eqs. (81) and (83) for A and B in plane strain condition,

$$A = \frac{9}{4} \frac{\xi^2 - 1}{(1 + \nu)^2} \quad (84)$$

$$B = \xi$$

Since A and B should be non negative real numbers, the range of ξ needs to be

$$\xi \geq 1 \quad (85)$$

Solving Eqs. (82) and (83) for A and B in plane stress condition,

$$A = \frac{9}{4} (\xi^2 - 1) \quad (86)$$

$$B = \xi$$

Since A and B should be non negative real numbers, the range of ξ needs to be

$$\xi \geq 1 \quad (87)$$

Thus the characteristic plane orientation calculated by the MTS criterion is only applicable to brittle material.

According to the maximum shear stress criteria (MSS), the maximum shear stress at r_c occurs at the angel of θ , which satisfies

$$\frac{\partial \tau_{\theta z'}}{\partial \beta} = 0 \quad \frac{\partial \tau_{\theta z'}}{\partial \theta} = 0 \quad \frac{\partial^2 \tau_{\theta z'}}{\partial \beta^2} < 0 \quad \frac{\partial^2 \tau_{\theta z'}}{\partial \beta^2} \frac{\partial^2 \tau_{\theta z'}}{\partial \theta^2} - \left(\frac{\partial^2 \tau_{\theta z'}}{\partial \beta \partial \theta} \right)^2 > 0 \quad (88)$$

Thus in case 1 for plane strain, $\beta = -\pi/4$ and $\theta = 0$ at $0 < \nu \leq 0.375$ (for most metals $0.29 \leq \nu \leq 0.37$) and $\beta = \pi/4$ and $\theta = \pm 2 \arccos(\sqrt{2\nu/3})$ at $0.375 < \nu < 1.5$ and for plane stress condition, $\beta = -\pi/4$ and $\theta = 0$. Then Eq. (75) for plane strain can be rewritten as:

$$\begin{aligned} \sqrt{\left(\frac{1}{2} + \nu\right)^2 + \left[\frac{1}{\xi} \left(\frac{1}{2} - \nu\right)\right]^2} + A \frac{4}{9} (1 + \nu)^2 = B \quad @ 0 < \nu \leq 0.375 \\ \sqrt{\frac{2}{3} \nu} \sqrt{\frac{16}{9} \nu^2 + \frac{2\nu^2 + 3\nu}{9\xi^2} + A \frac{4}{9} (1 + \nu)^2} = B \quad @ 0.375 < \nu < 1.5 \end{aligned} \quad (89)$$

Eq. (76) for plane stress can be rewritten as:

$$\sqrt{\frac{1}{4} + \frac{1}{4\xi^2} + A \frac{4}{9}} = B \quad (90)$$

In case 2 for both plane strain and plane stress condition, $\theta = 0$ and $\beta = 0$. Eq. (79) can be rewritten as

$$1 = B \quad (91)$$

Solve Eq. (89) and (91) for A and B in plane strain condition

$$\begin{aligned} A &= \frac{9}{4} \frac{1/2 - \nu}{(1 + \nu)^2} \left[\left(\frac{3}{2} + \nu \right) - \frac{1}{\xi^2} \left(\frac{1}{2} - \nu \right) \right] \quad (0 < \nu \leq 0.375) \\ B &= 1 \end{aligned} \quad (92)$$

and

$$A = \frac{(27 - 32\nu^3)\xi^2 - (4\nu^3 + 6\nu^2)}{8\nu(1+\nu)^2 \xi^2} \quad (0.375 < \nu < 3\sqrt[3]{2}/4) \quad (93)$$

$$B = 1$$

Since A and B should be non-negative real numbers, the range of ξ needs to be

$$\xi \geq \sqrt{\frac{1/2 - \nu}{3/2 + \nu}} \quad (0 < \nu \leq 0.375) \quad (94)$$

$$\xi \geq \sqrt{\frac{4\nu^3 + 6\nu^2}{27 - 32\nu^3}} \quad (0.375 < \nu < 3\sqrt[3]{2}/4)$$

Solve Eq. (90) and (91) for A and B in plane stress condition

$$A = \frac{27\xi^2 - 9}{16\xi^2} \quad (95)$$

$$B = 1$$

Since A and B should be non-negative real numbers, the range of ξ needs to be

$$\xi \geq \sqrt{3}/3 \quad (96)$$

Thus the characteristic plane orientation calculated by the MSS criterion is applicable for both brittle and ductile materials. In these two extreme cases (case 1 and case 2) the characteristic plane orientations coincide with the crack orientations predicted by MSS. Thus the MSS criterion is used to predict crack orientation θ below.

The contribution of the hydrostatic stress is different for different materials if the characteristic plane is fixed for all materials. There are two materials: $\xi = 1$ for case 1 and $\xi = \sqrt{3}/3$ for case 2 (plane stress condition), for which the contribution of hydrostatic stress is zero. It is also noticed that, if the characteristic plane is fixed, the range of applicable material parameters is limited.

Instead of fixing the characteristic plane, the current model searches for the characteristic plane orientations on which the contribution of the hydrostatic stress is minimized to zero.

For an arbitrary material, the characteristic plane orientation is assumed to be α (as shown in Figure 10). Since the contribution of the hydrostatic stress is zero, Eq. (71) is rewritten as:

$$\sqrt{\left(\frac{\sigma_{\theta\theta,\alpha}}{f_{-1}}\right)^2 + \left(\frac{\tau_{r\theta,\alpha}}{t_{-1}}\right)^2 + \left(\frac{\tau_{\theta z,\alpha}}{t_{-1}}\right)^2} = B \quad (97)$$

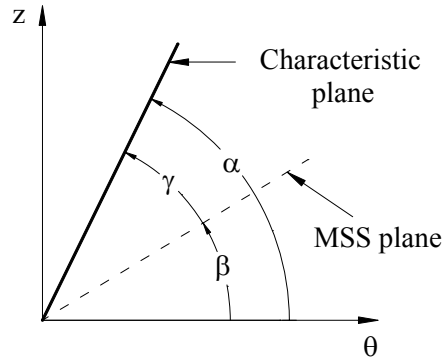


Figure 10. Orientation of characteristic plane and maximum shear stress (MSS) plane for mixed-mode I+III

The objective is to find α and B for an arbitrary material. Following the steps described for the first two cases, for plane strain condition Eq. (75) and (79) can be rewritten as

$$\sqrt{\left(\cos^2(\beta_1 + \gamma) + 2\nu \sin^2(\beta_1 + \gamma)\right)^2 + \left(\frac{1}{\xi} \left(\nu - \frac{1}{2}\right) \sin(2(\beta_1 + \gamma))\right)^2} = B \quad (98)$$

$$\sqrt{(\xi \sin(2(\beta_2 + \gamma)))^2 + (\cos(2(\beta_2 + \gamma)))^2} = B \quad (99)$$

where $\beta_1 = -\pi/4$ $\beta_2 = 0$. At $\nu = 0.3$ solve Eqs. (98) and (99)

$$\sin(2\gamma) = \begin{cases} 1 & (\xi = 1) \\ \frac{4\xi^2 - \sqrt{1 - 35\xi^2 - 225\xi^6 + 275\xi^4}}{-26\xi^2 + 25\xi^4 + 1} & (0.31408 < \xi < 1) \end{cases} \quad (100)$$

$$B = \sqrt{1 + (\xi^2 - 1)\sin^2(2\gamma)}$$

For plane stress condition Eqs. (76) and (79) can be rewritten as

$$\sqrt{(\cos^2(\beta_1 + \gamma))^2 + \left[\frac{1}{2\xi} \sin(2(\beta_1 + \gamma))\right]^2} = B \quad (101)$$

$$\sqrt{(\xi \sin(2(\beta_2 + \gamma)))^2 + (\cos(2(\beta_2 + \gamma)))^2} = B \quad (102)$$

where $\beta_1 = -\pi/4$ $\beta_2 = 0$. Solve Eqs. (101) and (102)

$$\sin(2\gamma) = \begin{cases} \frac{-1 + \sqrt{1 - (5 - 4\xi^2 - 1/\xi^2)(1/\xi^2 - 3)}}{5 - 4\xi^2 - 1/\xi^2} & (\sqrt{3}/3 \leq \xi < 1) \\ 1 & (\xi = 1) \end{cases} \quad (103)$$

$$B = \sqrt{1 + (\xi^2 - 1)\sin^2(2\gamma)}$$

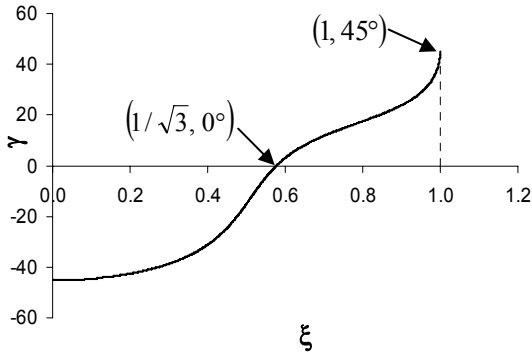


Figure 11. γ .vs. ξ for mixed-mode I+III (plane stress)

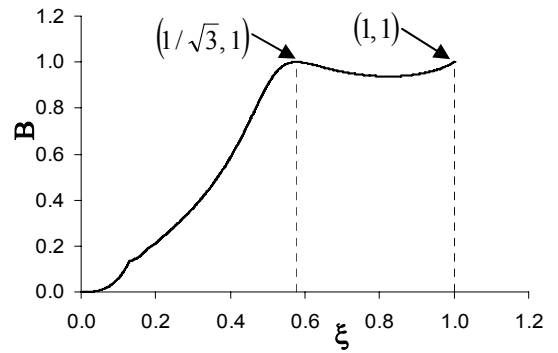


Figure 12. B .vs. ξ for mixed-mode I+III (plane stress)

For a mixed-mode I and III crack, θ and β can be solved from the MSS criterion.

Under plane strain condition:

$$\tau_{\theta z'} = \frac{1}{\sqrt{2\pi r}} \left[K_I \left(\nu - \frac{1}{2} \right) \sin(2\beta) + K_{III} \cos(2\beta) \right] \quad (104)$$

Applying Eq. (88) to Eq. (104),

$$\begin{aligned} \theta &= 0 \\ \tan(2\beta) &= \frac{K_I}{K_{III}} \left(\nu - \frac{1}{2} \right) \end{aligned} \quad (105)$$

Under plane stress condition:

$$\tau_{\theta z'} = \frac{1}{\sqrt{2\pi r}} \left[-\frac{1}{2} K_I \sin(2\beta) + K_{III} \cos(2\beta) \right] \quad (106)$$

Applying Eq. (88) to Eq. (106),

$$\begin{aligned} \theta &= 0 \\ \tan(2\beta) &= -\frac{K_I}{2K_{III}} \end{aligned} \quad (107)$$

The relationships between β and K_I / K_{III} are plotted in Figure 13.

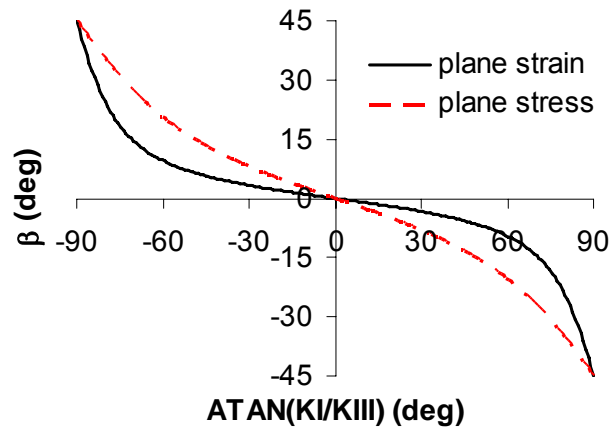


Figure 13. Mixed-mode I and III crack orientation β using MSS criterion ($\nu = 0.3$ in plane strain)

Then the characteristic plane angle α can be calculated as

$$\alpha = \beta + \gamma \quad (108)$$

Eq. (97) becomes

$$\sqrt{\left(\frac{K_I(\cos^2(\alpha) + 2\nu\sin^2(\alpha)) + K_{III}\sin(2\alpha)}{K_{I,th}}\right)^2 + \left(\frac{K_I\left(\nu - \frac{1}{2}\right)\sin(2\alpha) + K_{III}\cos(2\alpha)}{\xi K_{I,th}}\right)^2} + A\left(\frac{2(1+\nu)K_I}{3K_{I,th}}\right)^2 = B \quad (109)$$

2.4.2 Mixed-mode I and III fatigue crack growth

For prediction corresponding to a general crack growth rate da/dN , the threshold stress intensity factors ($K_{I,th}$ and $K_{III,th}$) may be replaced by the stress intensity coefficients at the specific crack growth rate ($K_{I,da/dN}$ and $K_{III,da/dN}$). In the proposed mixed mode crack growth model, stress intensity coefficients at the specific crack growth rates are considered as equivalent stress intensity factor for mixed mode case. The mixed mode crack growth model is expressed as

For plane strain condition

$$K_{mix,eq} = \frac{1}{B} \sqrt{\left(K_I(\cos^2(\alpha) + 2\nu\sin^2(\alpha)) + K_{III}\sin(2\alpha)\right)^2 + \left(\frac{K_I\left(\nu - \frac{1}{2}\right)\sin(2\alpha) + K_{III}\cos(2\alpha)}{\xi}\right)^2} + A\left(\frac{2(1+\nu)K_I}{3}\right)^2 = K_{I,da/dN} = f\left(\frac{da}{dN}\right) \quad (110)$$

For plane stress condition

$$K_{mix,eq} = \frac{1}{B} \sqrt{\left(K_I\cos^2(\alpha) + K_{III}\sin(2\alpha)\right)^2 + \left(\frac{K_I\left(-\frac{1}{2}\right)\sin(2\alpha) + K_{III}\cos(2\alpha)}{\xi}\right)^2} + A\left(\frac{2K_I}{3}\right)^2 = K_{I,da/dN} = f\left(\frac{da}{dN}\right) \quad (111)$$

where $f\left(\frac{da}{dN}\right)$ is the crack growth curve obtained under mode I loading. There are no closed form solutions for Eqs. (110) and (111). In practical calculation, a trial and error method can be used to find da/dN . For a high cycle fatigue problem, $K_{III,da/dN}$ and

$K_{I,da/dN}$ take initial values as $K_{III,th}$ and $K_{I,th}$, respectively. Usually a few iterations are enough to make N_f converge.

2.4.3 Experimental validation

Seven sets of fatigue experimental data available in the literature are employed in this section and listed in Table 3. The predicted thresholds and the experimental observations are plotted in Figure 14. In Figure 14, the x -axis and the y -axis are the applied stress intensity ranges for mode I and mode III, respectively. All values are normalized using the mode I threshold stress intensity factor. For comparisons, the predictions using the mixed mode I and III threshold stress intensity factor criteria, such as the energy release rate, MTS, and Pook's law [70] are also plotted. As shown in Figure 14, the predicted values using the proposed method agree with experimental observations much better than the existing three models.

Table 3. Experimental threshold data used for model validation

Steel	References	$K_{I,th} (Mpa\sqrt{m})$	ξ
3/3 ^{1/2} %Ni	[70]	10.23	0.57
3%Ni	[70]	7.10	0.67
3 ^{1/2} %NiCr (low impact)	[70]	8.35	0.68
CrVa	[70]	7.30	0.69
3 ^{1/2} %NiCr (normal impact)	[70]	9.08	0.81
NiCrMo	[70]	9.18	0.82
0.4%C	[70]	6.05	0.91

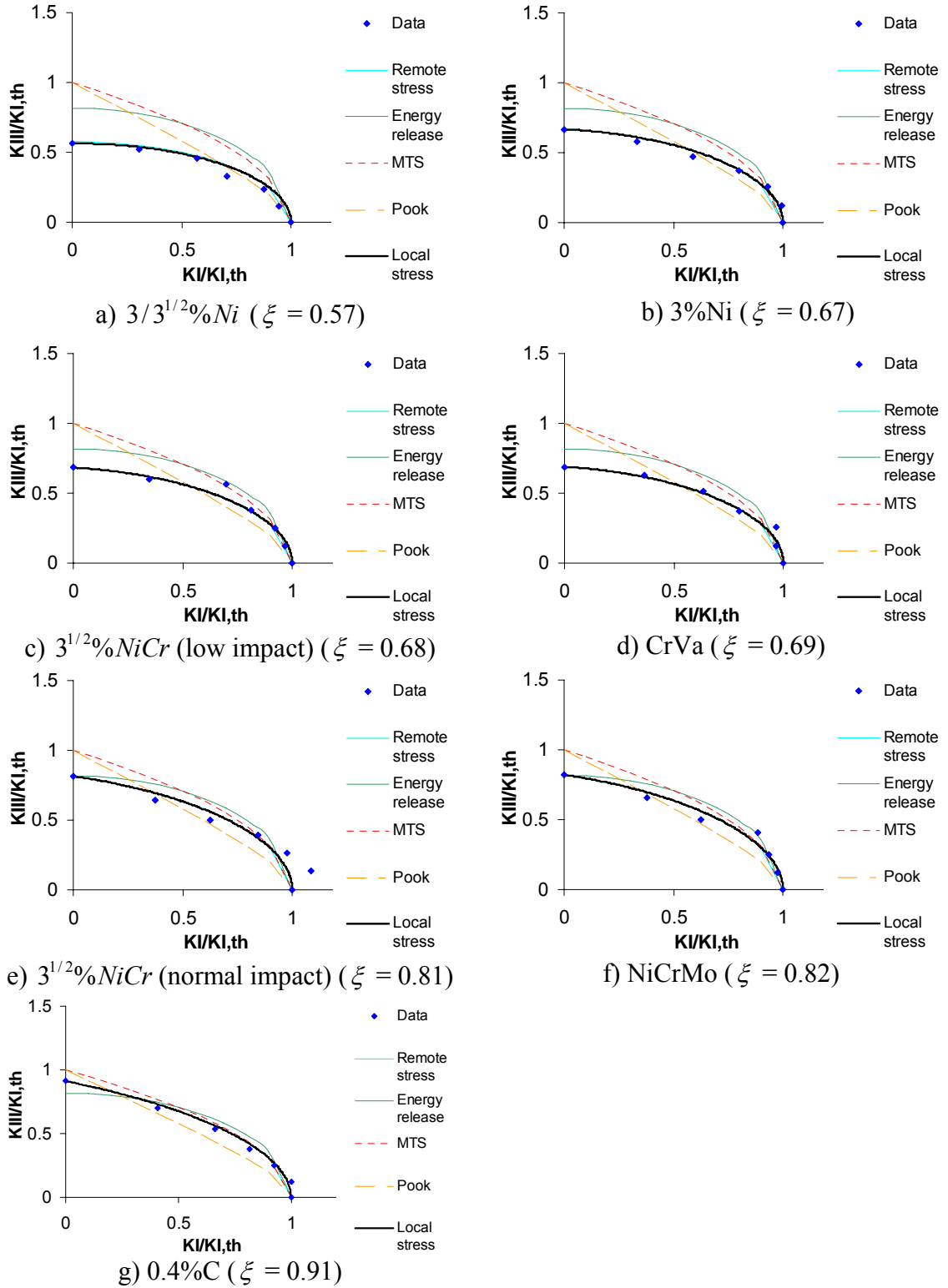


Figure 14. Comparisons of predicted and experimental threshold stress intensity factors for mixed-mode I+III

2.5 Proposed mixed-mode I, II and III fatigue model

Consider an infinite plate under remote normal and out of plane shear stress as shown in Figure 15, there is a mixed-mode I, II and III stress field near crack tip, which can be expressed as:

$$\begin{aligned}
 \sigma_{rr} &= \frac{1}{\sqrt{2\pi r}} \cos\left(\frac{\theta}{2}\right) \left[K_I \left(1 + \sin^2\left(\frac{\theta}{2}\right)\right) + K_{II} \left(\frac{3}{2} \sin(\theta) - 2 \tan\left(\frac{\theta}{2}\right)\right) \right] \\
 \sigma_{\theta\theta} &= \frac{1}{\sqrt{2\pi r}} \cos\left(\frac{\theta}{2}\right) \left[K_I \cos^2\left(\frac{\theta}{2}\right) - \frac{3}{2} K_{II} \sin(\theta) \right] \\
 \sigma_{zz} &= \begin{cases} 0 & \text{plane stress} \\ \nu(\sigma_{\theta\theta} + \sigma_{rr}) = \frac{2\nu}{\sqrt{2\pi r}} \cos\left(\frac{\theta}{2}\right) \left[K_I - K_{II} \tan\left(\frac{\theta}{2}\right) \right] & \text{plane strain} \end{cases} \quad (112) \\
 \tau_{r\theta} &= \frac{1}{2\sqrt{2\pi r}} \cos\left(\frac{\theta}{2}\right) \left[K_I \sin(\theta) + K_{II} (3 \cos(\theta) - 1) \right] \\
 \tau_{rz} &= \frac{K_{III}}{\sqrt{2\pi r}} \sin\left(\frac{\theta}{2}\right) \\
 \tau_{\theta z} &= \frac{K_{III}}{\sqrt{2\pi r}} \cos\left(\frac{\theta}{2}\right)
 \end{aligned}$$

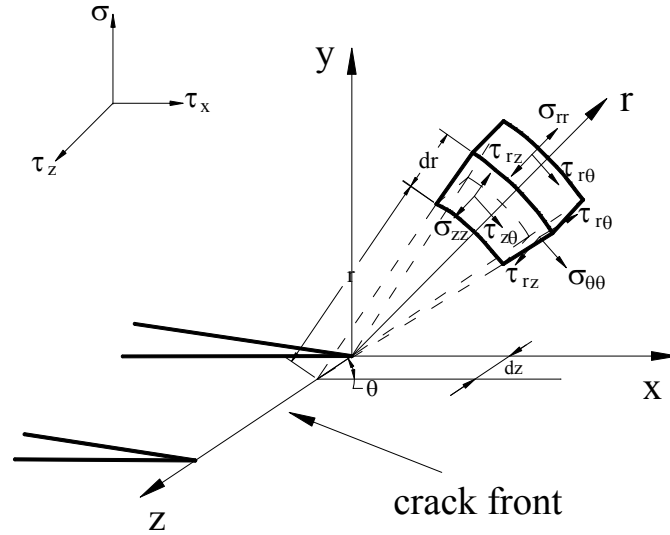


Figure 15. Mixed-mode I, II and III stress fields near crack tip

Experimental data shows that the failure surface under mixed mode I, II and III loading condition is typically non-planar. Assume coordinate (r, θ, z) rotates β around axis r to coordinate (r', θ', z') , the stress in the new coordinate can be expressed as

$$\begin{aligned}
\sigma_{r'r'} &= \sigma_{rr} \\
\sigma_{\theta'\theta'} &= \frac{\sigma_{\theta\theta} + \sigma_{zz}}{2} + \frac{\sigma_{\theta\theta} - \sigma_{zz}}{2} \cos(2\beta) + \tau_{\theta z} \sin(2\beta) \\
\sigma_{z'z'} &= \frac{\sigma_{\theta\theta} + \sigma_{zz}}{2} - \frac{\sigma_{\theta\theta} - \sigma_{zz}}{2} \cos(2\beta) - \tau_{\theta z} \sin(2\beta) \\
\tau_{r'\theta'} &= \tau_{r\theta} \cos(\beta) + \tau_{rz} \sin(\beta) \\
\tau_{r'z'} &= -\tau_{r\theta} \sin(\beta) + \tau_{rz} \cos(\beta) \\
\tau_{\theta'z'} &= -\frac{\sigma_{\theta\theta} - \sigma_{zz}}{2} \sin(2\beta) + \tau_{\theta z} \cos(2\beta)
\end{aligned} \tag{113}$$

Under plane strain condition, Eq. (68) can be expressed as

$$\begin{aligned}
\sigma_{r'r'} &= \frac{1}{\sqrt{2\pi r}} \cos\left(\frac{\theta}{2}\right) \left[K_I \left(1 + \sin^2\left(\frac{\theta}{2}\right) \right) + K_{II} \left(\frac{3}{2} \sin(\theta) - 2 \tan\left(\frac{\theta}{2}\right) \right) \right] \\
\sigma_{\theta'\theta'} &= \frac{1}{\sqrt{2\pi r}} \cos\left(\frac{\theta}{2}\right) \left[K_I \left(\cos^2\left(\frac{\theta}{2}\right) \cos^2(\beta) + 2\nu \sin^2(\beta) \right) - K_{II} \left(\frac{3}{2} \sin(\theta) \cos^2(\beta) + 2\nu \tan\left(\frac{\theta}{2}\right) \sin^2(\beta) \right) + K_{III} \sin(2\beta) \right] \\
\sigma_{z'z'} &= \frac{1}{\sqrt{2\pi r}} \cos\left(\frac{\theta}{2}\right) \left[K_I \left(\cos^2\left(\frac{\theta}{2}\right) \sin^2(\beta) + 2\nu \cos^2(\beta) \right) - K_{II} \left(\frac{3}{2} \sin(\theta) \sin^2(\beta) + 2\nu \tan\left(\frac{\theta}{2}\right) \cos^2(\beta) \right) - K_{III} \sin(2\beta) \right] \\
\tau_{r'\theta'} &= \frac{1}{\sqrt{2\pi r}} \left[\frac{1}{2} K_I \cos\left(\frac{\theta}{2}\right) \sin(\theta) \cos(\beta) + \frac{1}{2} K_{II} \cos\left(\frac{\theta}{2}\right) (3 \cos(\theta) - 1) \cos(\beta) + K_{III} \sin\left(\frac{\theta}{2}\right) \sin(\beta) \right] \\
\tau_{r'z'} &= \frac{1}{\sqrt{2\pi r}} \left[-\frac{1}{2} K_I \cos\left(\frac{\theta}{2}\right) \sin(\theta) \sin(\beta) - \frac{1}{2} K_{II} \cos\left(\frac{\theta}{2}\right) (3 \cos(\theta) - 1) \sin(\beta) + K_{III} \sin\left(\frac{\theta}{2}\right) \cos(\beta) \right] \\
\tau_{\theta'z'} &= \frac{1}{\sqrt{2\pi r}} \cos\left(\frac{\theta}{2}\right) \left[K_I \left(\nu - \frac{1}{2} \cos^2\left(\frac{\theta}{2}\right) \right) \sin(2\beta) + K_{II} \left(\frac{3}{4} \sin(\theta) - \nu \tan\left(\frac{\theta}{2}\right) \right) \sin(2\beta) + K_{III} \cos(2\beta) \right]
\end{aligned} \tag{114}$$

Under plane stress condition, Eq. (68) can be expressed as

$$\begin{aligned}
\sigma_{r'r'} &= \frac{1}{\sqrt{2\pi r'}} \cos\left(\frac{\theta}{2}\right) \left[K_I \left(1 + \sin^2\left(\frac{\theta}{2}\right) \right) + K_{II} \left(\frac{3}{2} \sin(\theta) - 2 \tan\left(\frac{\theta}{2}\right) \right) \right] \\
\sigma_{\theta'\theta'} &= \frac{1}{\sqrt{2\pi r'}} \cos\left(\frac{\theta}{2}\right) \left[K_I \cos^2\left(\frac{\theta}{2}\right) \cos^2(\beta) - \frac{3}{2} K_{II} \sin(\theta) \cos^2(\beta) + K_{III} \sin(2\beta) \right] \\
\sigma_{z'z'} &= \frac{1}{\sqrt{2\pi r'}} \cos\left(\frac{\theta}{2}\right) \left[K_I \cos^2\left(\frac{\theta}{2}\right) \sin^2(\beta) - \frac{3}{2} K_{II} \sin(\theta) \sin^2(\beta) - K_{III} \sin(2\beta) \right] \\
\tau_{r'\theta'} &= \frac{1}{\sqrt{2\pi r'}} \left[\frac{1}{2} K_I \cos\left(\frac{\theta}{2}\right) \sin(\theta) \cos(\beta) + \frac{1}{2} K_{II} \cos\left(\frac{\theta}{2}\right) (3 \cos(\theta) - 1) \cos(\beta) + K_{III} \sin\left(\frac{\theta}{2}\right) \sin(\beta) \right] \\
\tau_{r'z'} &= \frac{1}{\sqrt{2\pi r'}} \left[-\frac{1}{2} K_I \cos\left(\frac{\theta}{2}\right) \sin(\theta) \sin(\beta) - \frac{1}{2} K_{II} \cos\left(\frac{\theta}{2}\right) (3 \cos(\theta) - 1) \sin(\beta) + K_{III} \sin\left(\frac{\theta}{2}\right) \cos(\beta) \right] \\
\tau_{\theta'z'} &= \frac{1}{\sqrt{2\pi r'}} \cos\left(\frac{\theta}{2}\right) \left[-\frac{1}{2} K_I \cos^2\left(\frac{\theta}{2}\right) \sin(2\beta) + \frac{3}{4} K_{II} \sin(\theta) \sin(2\beta) + K_{III} \cos(2\beta) \right]
\end{aligned} \tag{115}$$

Thus for mixed mode I, II and III under both plane strain and plane stress condition, the fatigue limit criterion becomes

$$\sqrt{\left(\frac{\sigma_{\theta'\theta'}}{f_{-1}}\right)^2 + \left(\frac{\tau_{r'\theta'}}{t_{-1}}\right)^2 + \left(\frac{\tau_{\theta'z'}}{t_{-1}}\right)^2 + A \left(\frac{\sigma_{\theta'\theta'} + \sigma_{z'z'} + \sigma_{r'r'}}{3f_{-1}}\right)^2} = B \tag{116}$$

where $-\pi \leq \theta \leq \pi$ and $-\pi/2 \leq \beta \leq \pi/2$. To determine the parameters A and B , two extreme cases are considered below:

Case 1: Mixed mode I and II fatigue experiment as shown in Figure 2:

In this case there is no contribution of K_{III} . From Eqs. (69) and (70) the stress fields near crack tip can be rewritten as

(a) Under plane strain condition:

$$\begin{aligned}
\sigma_{r'r'} &= \frac{1}{\sqrt{2\pi r}} \cos\left(\frac{\theta}{2}\right) \left[K_I \left(1 + \sin^2\left(\frac{\theta}{2}\right) \right) + K_{II} \left(\frac{3}{2} \sin(\theta) - 2 \tan\left(\frac{\theta}{2}\right) \right) \right] \\
\sigma_{\theta'\theta'} &= \frac{1}{\sqrt{2\pi r}} \cos\left(\frac{\theta}{2}\right) \left[K_I \left(\cos^2\left(\frac{\theta}{2}\right) \cos^2(\beta) + 2\nu \sin^2(\beta) \right) - K_{II} \left(\frac{3}{2} \sin(\theta) \cos^2(\beta) + 2\nu \tan\left(\frac{\theta}{2}\right) \sin^2(\beta) \right) \right] \\
\sigma_{z'z'} &= \frac{1}{\sqrt{2\pi r}} \cos\left(\frac{\theta}{2}\right) \left[K_I \left(\cos^2\left(\frac{\theta}{2}\right) \sin^2(\beta) + 2\nu \cos^2(\beta) \right) - K_{II} \left(\frac{3}{2} \sin(\theta) \sin^2(\beta) + 2\nu \tan\left(\frac{\theta}{2}\right) \cos^2(\beta) \right) \right] \\
\tau_{r'\theta'} &= \frac{1}{2\sqrt{2\pi r}} \cos\left(\frac{\theta}{2}\right) \left[K_I \sin(\theta) + K_{II} (3 \cos(\theta) - 1) \right] \cos(\beta) \\
\tau_{r'z'} &= -\frac{1}{2\sqrt{2\pi r}} \cos\left(\frac{\theta}{2}\right) \left[K_I \sin(\theta) + K_{II} (3 \cos(\theta) - 1) \right] \sin(\beta) \\
\tau_{\theta'z'} &= \frac{1}{\sqrt{2\pi r}} \cos\left(\frac{\theta}{2}\right) \left[K_I \left(\nu - \frac{1}{2} \cos^2\left(\frac{\theta}{2}\right) \right) + K_{II} \left(\frac{3}{4} \sin(\theta) - \nu \tan\left(\frac{\theta}{2}\right) \right) \right] \sin(2\beta)
\end{aligned} \tag{117}$$

(b) Under plane stress condition:

$$\begin{aligned}
\sigma_{r'r'} &= \frac{1}{\sqrt{2\pi r}} \cos\left(\frac{\theta}{2}\right) \left[K_I \left(1 + \sin^2\left(\frac{\theta}{2}\right) \right) + K_{II} \left(\frac{3}{2} \sin(\theta) - 2 \tan\left(\frac{\theta}{2}\right) \right) \right] \\
\sigma_{\theta'\theta'} &= \frac{1}{\sqrt{2\pi r}} \cos\left(\frac{\theta}{2}\right) \left[K_I \cos^2\left(\frac{\theta}{2}\right) \cos^2(\beta) - \frac{3}{2} K_{II} \sin(\theta) \cos^2(\beta) \right] \\
\sigma_{z'z'} &= \frac{1}{\sqrt{2\pi r}} \cos\left(\frac{\theta}{2}\right) \left[K_I \cos^2\left(\frac{\theta}{2}\right) \sin^2(\beta) - \frac{3}{2} K_{II} \sin(\theta) \sin^2(\beta) \right] \\
\tau_{r'\theta'} &= \frac{1}{2\sqrt{2\pi r}} \cos\left(\frac{\theta}{2}\right) \left[K_I \sin(\theta) + K_{II} (3 \cos(\theta) - 1) \right] \cos(\beta) \\
\tau_{r'z'} &= -\frac{1}{2\sqrt{2\pi r}} \cos\left(\frac{\theta}{2}\right) \left[K_I \sin(\theta) + K_{II} (3 \cos(\theta) - 1) \right] \sin(\beta) \\
\tau_{\theta'z'} &= \frac{1}{\sqrt{2\pi r}} \cos\left(\frac{\theta}{2}\right) \left[-\frac{1}{2} K_I \cos^2\left(\frac{\theta}{2}\right) + \frac{3}{4} K_{II} \sin(\theta) \right] \sin(2\beta)
\end{aligned} \tag{118}$$

Case 2: Mixed mode I and III fatigue experiment as shown in Figure 9:

In this case there is no contribution of K_{II} . From Eqs. (69) and (70) the stress fields near crack tip can be rewritten as

(a) Under plane strain condition:

$$\begin{aligned}
\sigma_{r'r'} &= \frac{1}{\sqrt{2\pi r}} \cos\left(\frac{\theta}{2}\right) \left[K_I \left(1 + \sin^2\left(\frac{\theta}{2}\right) \right) \right] \\
\sigma_{\theta'\theta'} &= \frac{1}{\sqrt{2\pi r}} \cos\left(\frac{\theta}{2}\right) \left[K_I \left(\cos^2\left(\frac{\theta}{2}\right) \cos^2(\beta) + 2\nu \sin^2(\beta) \right) + K_{III} \sin(2\beta) \right] \\
\sigma_{z'z'} &= \frac{1}{\sqrt{2\pi r}} \cos\left(\frac{\theta}{2}\right) \left[K_I \left(\cos^2\left(\frac{\theta}{2}\right) \sin^2(\beta) + 2\nu \cos^2(\beta) \right) - K_{III} \sin(2\beta) \right] \\
\tau_{r'\theta'} &= \frac{1}{\sqrt{2\pi r}} \left[\frac{1}{2} K_I \cos\left(\frac{\theta}{2}\right) \sin(\theta) \cos(\beta) + K_{III} \sin\left(\frac{\theta}{2}\right) \sin(\beta) \right] \\
\tau_{r'z'} &= \frac{1}{\sqrt{2\pi r}} \left[-\frac{1}{2} K_I \cos\left(\frac{\theta}{2}\right) \sin(\theta) \sin(\beta) + K_{III} \sin\left(\frac{\theta}{2}\right) \cos(\beta) \right] \\
\tau_{\theta'z'} &= \frac{1}{\sqrt{2\pi r}} \cos\left(\frac{\theta}{2}\right) \left[K_I \left(\nu - \frac{1}{2} \cos^2\left(\frac{\theta}{2}\right) \right) \sin(2\beta) + K_{III} \cos(2\beta) \right]
\end{aligned} \tag{119}$$

(b) Under plane stress condition:

$$\begin{aligned}
\sigma_{r'r'} &= \frac{1}{\sqrt{2\pi r}} \cos\left(\frac{\theta}{2}\right) \left[K_I \left(1 + \sin^2\left(\frac{\theta}{2}\right) \right) \right] \\
\sigma_{\theta'\theta'} &= \frac{1}{\sqrt{2\pi r}} \cos\left(\frac{\theta}{2}\right) \left[K_I \cos^2\left(\frac{\theta}{2}\right) \cos^2(\beta) + K_{III} \sin(2\beta) \right] \\
\sigma_{z'z'} &= \frac{1}{\sqrt{2\pi r}} \cos\left(\frac{\theta}{2}\right) \left[K_I \cos^2\left(\frac{\theta}{2}\right) \sin^2(\beta) - K_{III} \sin(2\beta) \right] \\
\tau_{r'\theta'} &= \frac{1}{\sqrt{2\pi r}} \left[\frac{1}{2} K_I \cos\left(\frac{\theta}{2}\right) \sin(\theta) \cos(\beta) + K_{III} \sin\left(\frac{\theta}{2}\right) \sin(\beta) \right] \\
\tau_{r'z'} &= \frac{1}{\sqrt{2\pi r}} \left[-\frac{1}{2} K_I \cos\left(\frac{\theta}{2}\right) \sin(\theta) \sin(\beta) + K_{III} \sin\left(\frac{\theta}{2}\right) \cos(\beta) \right] \\
\tau_{\theta'z'} &= \frac{1}{\sqrt{2\pi r}} \cos\left(\frac{\theta}{2}\right) \left[-\frac{1}{2} K_I \cos^2\left(\frac{\theta}{2}\right) \sin(2\beta) + K_{III} \cos(2\beta) \right]
\end{aligned} \tag{120}$$

According to the maximum shear stress criterion (MSS), the maximum shear stress at r_c occurs at the angle of θ , which satisfies

$$\frac{\partial \tau_{r'\theta'}}{\partial \beta} = 0 \quad \frac{\partial \tau_{r'\theta'}}{\partial \theta} = 0 \quad \frac{\partial^2 \tau_{r'\theta'}}{\partial \beta^2} < 0 \quad \frac{\partial^2 \tau_{r'\theta'}}{\partial \beta^2} \frac{\partial^2 \tau_{r'\theta'}}{\partial \theta^2} - \left(\frac{\partial^2 \tau_{r'\theta'}}{\partial \beta \partial \theta} \right)^2 > 0 \tag{121}$$

for mixed mode I and II, and

$$\frac{\partial \tau_{\theta'z'}}{\partial \beta} = 0 \quad \frac{\partial \tau_{\theta'z'}}{\partial \theta} = 0 \quad \frac{\partial^2 \tau_{\theta'z'}}{\partial \beta^2} < 0 \quad \frac{\partial^2 \tau_{\theta'z'}}{\partial \beta^2} \frac{\partial^2 \tau_{\theta'z'}}{\partial \theta^2} - \left(\frac{\partial^2 \tau_{\theta'z'}}{\partial \beta \partial \theta} \right)^2 > 0 \tag{122}$$

for mixed mode I and III.

In case 1 for both plane strain and plane stress, the relationship between θ and the ratio of K_I to K_{II} is shown in Figure 16.

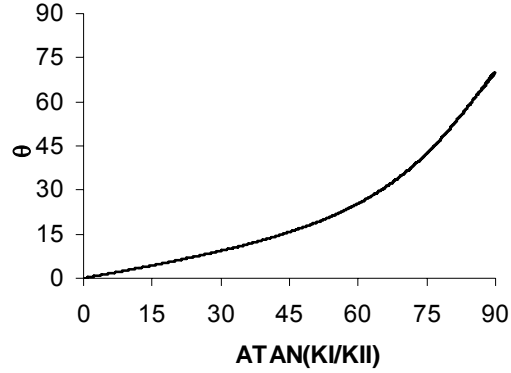


Figure 16. θ vs. K_I / K_{II}

Then Eq. (116) for plane strain condition can be rewritten as:

$$\left| \cos\left(\frac{\theta}{2}\right) \right| \sqrt{\left(\frac{K_I \cos^2\left(\frac{\theta}{2}\right) - \frac{3}{2} K_{II} \sin(\theta)}{K_{I,th}} \right)^2 + \left(\frac{K_I \sin(\theta) + K_{II} (3 \cos(\theta) - 1)}{2\xi K_{I,th}} \right)^2 + A \left(\frac{2(1+\nu) \left[K_I - K_{II} \tan\left(\frac{\theta}{2}\right) \right]}{3K_{I,th}} \right)^2} = B \quad (123)$$

For plane stress condition Eq. (116) can be expressed as

$$\left| \cos\left(\frac{\theta}{2}\right) \right| \sqrt{\left(\frac{K_I \cos^2\left(\frac{\theta}{2}\right) - \frac{3}{2} K_{II} \sin(\theta)}{K_{I,th}} \right)^2 + \left(\frac{K_I \sin(\theta) + K_{II} (3 \cos(\theta) - 1)}{2\xi K_{I,th}} \right)^2 + A \left(\frac{2 \left[K_I - K_{II} \tan\left(\frac{\theta}{2}\right) \right]}{3K_{I,th}} \right)^2} = B \quad (124)$$

In case 2 for plane strain condition

$$\tau_{\theta'z'} = \frac{1}{\sqrt{2\pi r}} \cos\left(\frac{\theta}{2}\right) \left[K_I \left(\nu - \frac{1}{2} \cos^2\left(\frac{\theta}{2}\right) \right) \sin(2\beta) + K_{III} \cos(2\beta) \right] \quad (125)$$

where θ and β can be solved from the MSS criterion using Eq. (88). Thus in mixed mode I and III for plane strain

$$\begin{cases} \theta = 0 \\ \tan(2\beta) = \frac{K_I}{K_{III}} \left(\nu - \frac{1}{2} \right) \end{cases} \quad (126)$$

In case 2 for plane stress condition

$$\tau_{\theta'z'} = \frac{1}{\sqrt{2\pi r}} \cos\left(\frac{\theta}{2}\right) \left[-\frac{1}{2} K_I \cos^2\left(\frac{\theta}{2}\right) \sin(2\beta) + K_{III} \cos(2\beta) \right] \quad (127)$$

where θ and β can be solved from MSS criteria using Eq. (88). Thus in mixed mode I and III for plane stress

$$\begin{cases} \theta = 0 \\ \tan(2\beta) = -\frac{1}{2} \frac{K_I}{K_{III}} \end{cases} \quad (128)$$

Then in case 2 under plane strain condition Eq. (116) can be rewritten as:

$$\sqrt{\left(\frac{K_I (\cos^2(\beta) + 2\nu \sin^2(\beta)) + K_{III} \sin(2\beta)}{K_{I,th}} \right)^2 + \left(\frac{K_I \left(\nu - \frac{1}{2} \right) \sin(2\beta) + K_{III} \cos(2\beta)}{\xi K_{I,th}} \right)^2} + A \left(\frac{2(1+\nu)K_I}{3K_{I,th}} \right)^2 = B \quad (129)$$

For plane stress condition Eq. (116) can be expressed as

$$\sqrt{\left(\frac{K_I \cos^2(\beta) + K_{III} \sin(2\beta)}{K_{I,th}} \right)^2 + \left(\frac{-\frac{1}{2} K_I \sin(2\beta) + K_{III} \cos(2\beta)}{\xi K_{I,th}} \right)^2} + A \left(\frac{2K_I}{3K_{I,th}} \right)^2 = B \quad (130)$$

Eqs.(129) and (130) can be simplified as: for plane strain condition

$$\left| \frac{K_I}{K_{I,th}} \right| \sqrt{\left(\nu + \frac{1}{2} \right)^2 + \frac{1 + (K_I / K_{III})^2 \left(\nu - \frac{1}{2} \right)^2}{\xi^2 (K_I / K_{III})^2}} + \frac{4}{9} A (1 + \nu)^2 = B \quad (131)$$

for plane stress condition

$$\left| \frac{K_I}{K_{I,th}} \right| \sqrt{\frac{1}{4} + \frac{1 + (K_I / K_{III})^2 / 4}{\xi^2 (K_I / K_{III})^2} + \frac{4}{9} A} = B \quad (132)$$

Solve Eqs. (123) and (131) for A and B in plane strain condition

$$A = \frac{\left(\frac{\cos^2(\theta/2)}{9\cos^2(\theta/2)-2} \right)^2 \left[16\cos^2(\theta/2) + \frac{1}{\xi^2} \frac{(\cos^2(\theta/2)-2)^2}{\sin^2(\theta/2)} \right] - \left(\nu + \frac{1}{2} \right)^2 - \frac{1 + (K_I / K_{III})^2 \left(\nu - \frac{1}{2} \right)^2}{\xi^2 (K_I / K_{III})^2}}{\frac{4}{9} (\nu + 1)^2 - 16 \left(\frac{\cos^2(\theta/2)}{9\cos^2(\theta/2)-2} \right)^2 (1 + \nu)^2 \cos^2(\theta/2)} \quad (133)$$

$$B = \left| \cos\left(\frac{\theta}{2}\right) \right| \sqrt{\left(\frac{K_I \cos^2\left(\frac{\theta}{2}\right) - \frac{3}{2} K_{II} \sin(\theta)}{K_{I,th}} \right)^2 + \left(\frac{K_I \sin(\theta) + K_{II} (3\cos(\theta) - 1)}{2\xi K_{I,th}} \right)^2 + A \left(\frac{2(1+\nu) \left[K_I - K_{II} \tan\left(\frac{\theta}{2}\right) \right]}{3K_{I,th}} \right)^2}$$

Solve Eqs. (124) and (132) for A and B in plane stress condition

$$A = \frac{\left(\frac{\cos^2(\theta/2)}{9\cos^2(\theta/2)-2} \right)^2 \left[16\cos^2(\theta/2) + \frac{1}{\xi^2} \frac{(\cos^2(\theta/2)-2)^2}{\sin^2(\theta/2)} \right] - \frac{1}{4} - \frac{1 + (K_I / K_{III})^2 / 4}{\xi^2 (K_I / K_{III})^2}}{\frac{4}{9} - 16 \left(\frac{\cos^2(\theta/2)}{9\cos^2(\theta/2)-2} \right)^2 \cos^2(\theta/2)} \quad (134)$$

$$B = \left| \frac{K_I}{K_{I,th}} \right| \sqrt{\frac{1}{4} + \frac{1 + (K_I / K_{III})^2 / 4}{\xi^2 (K_I / K_{III})^2} + \frac{4}{9} A}$$

where A and B should be non negative real numbers.

The characteristic plane orientation calculated by the MSS criterion is applicable for both brittle and ductile materials. In these two extreme cases (case 1 and case 2) the characteristic plane orientations coincide with the crack orientations θ and β predicted by the MSS criterion. If the length of the structure is much greater than the other two dimensions, Eq. (133) for plane strain can be used. If one of the dimensions of the structure is much smaller than the other two, such as in a thin plate, Eq. (134) for plane stress can be applied.

2.6 Conclusion

Three models for mixed-mode (I+II / I+III / I+II+III) threshold stress intensity factor and crack growth rate prediction are proposed in this chapter. The prediction based on the proposed criterion shows excellent agreement with the experimental threshold stress intensity factor data reported in the literature. The new threshold stress intensity factor criterion is then extended to develop a fatigue crack growth rate prediction model. A very good agreement is obtained between experimental and predicted fatigue crack growth rates.

The proposed fatigue crack growth model is developed using the local stress components (near crack tip) and the characteristic plane concept. Most of the existing fatigue crack growth models can only be applied to individual failure modes, i.e., shear dominated failure or tension dominated failure. Their applicability generally depends on the material's properties and loading conditions. In the proposed model, the characteristic plane changes its orientation corresponding to different material failure modes, thus helping the proposed model to have a wide range of applicability.

The proposed models in this chapter are only applicable to smooth specimens. In reality, structural components contain holes or notches. To make the proposed criteria more realistic, notch effects need to be included in the local stress expressions. This is investigated in Chapter 3.

CHAPTER III

MIXED-MODE NEAR THRESHOLD FATIGUE CRACK GROWTH FROM NOTCH

3.1 Overview

Whether deliberately created or inadvertently induced, notches and other geometrical irregularities invariably exist in engineering components which cause significant stress concentration and lead to the initiation of fatigue cracks.

The crack initiation life of notched components is predicted using the classical stress/strain-based approach, and the stress concentration effect is addressed by a fatigue notch factor K_f instead of the elastic stress concentration factor K_t . The most commonly accepted definition of K_f is the ratio of the unnotched bar endurance limit to that of a notched bar under the same experimental conditions and the same number of cycles [71].

$$K_f = \frac{\text{unnotched bar endurance limit}}{\text{notched bar endurance limit}} \quad (135)$$

The fatigue notch factor depends on many factors such as notch geometry, material properties, loading type and fatigue life. Though the most reliable way to determine K_f is from experiments, there are many empirical formulas proposed for engineering application, which can be found in previous review papers [72, 73]. The basic idea is to consider the stress at a specific location or averaged over a domain from the notch tip and to express the critical distance as a function of the tensile strength of the material. Due to the high localized stress/strain, the crack initiation life could decrease

significantly and 90% of the fatigue time may be spent on crack propagation time. So this approach is very useful when the stress levels below the fatigue limit, but could be dangerous in the finite life regime [74]. Since this approach does not take into account the fatigue crack near notch tip, it is not able to analyze the different modes and extensions of fatigue cracks.

To eliminate these deficiencies, fracture mechanics based approaches have been applied for the fatigue analysis at a notch. By neglecting the fatigue initiation period, the fatigue process is assumed to be a crack growth process, which is driven by stress intensity factor, J integral or crack tip displacement [74, 75]. Some attempts have been made to unify the studies between notch and crack [76-78], which rely on some length scale parameters whose physical meaning hasn't been fully understood.

For simplification purposes, crack is usually regarded as a mathematical line and the crack tip is regarded as a mathematical singular point. For a blunt crack which can also be considered as a U-shaped notch, the stress near the crack or notch tip depends largely on the radius of curvature at the crack or notch tip. In this case, the effects of notch tip radius need to be included in the Kitagawa-Takahashi diagram and the local stress expressions. There are three typical notch configurations as shown in Figure 17. For the notch with rounded or elliptical notch tip (Figure 17 (a)), Creager and Paris [79] derived closed form solutions for the elastic stress field ahead of notch tip. For the other notch types, the stress field are shown in [80]. Several analytical models have been proposed to calculate the stress intensity factor. A brief review is given below.

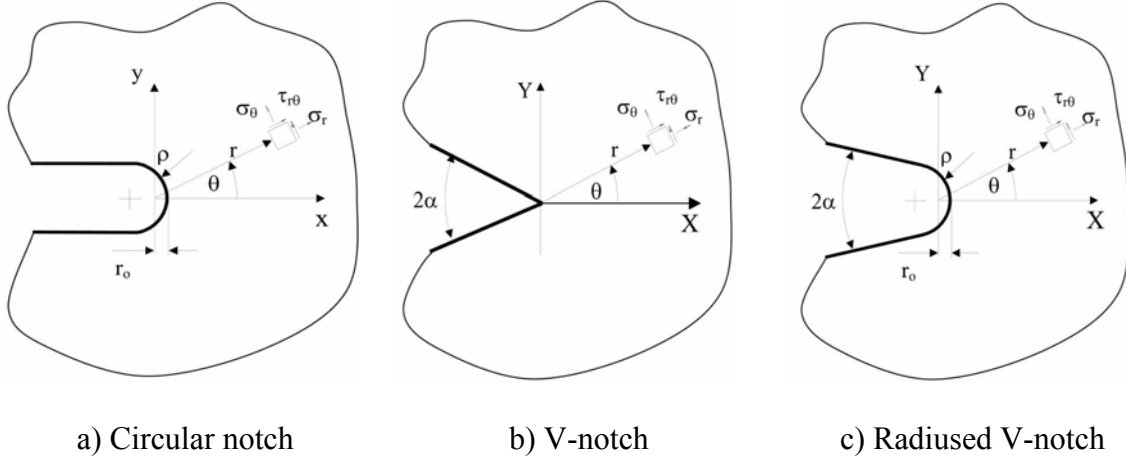


Figure 17. Typical notch configurations

Smith and Miller [74] proposed the stress intensity factor of small cracks at the root of a notch as

$$K = \sqrt{1 + 7.69\sqrt{D/\rho}\sigma\sqrt{\pi a}} \quad (136)$$

where a is the crack length, σ is the applied stress, D is the notch depth and ρ is the notch tip radius.

Kujawski [81] applied the local stress distribution at a distance a from the notch tip for the stress intensity factor calculation. The formula can be shown as

$$\Delta K = F_f \frac{K_t}{2} \left[\left(1 + 2\frac{a}{\rho}\right)^{-1/2} + \left(1 + 2\frac{a}{\rho}\right)^{-3/2} \right] \Delta\sigma\sqrt{\pi a} \quad (137)$$

where K_t is the stress concentration factor, $\Delta\sigma$ is the applied stress range and F_f is the geometric factor. This approximation is quite accurate for uni-axial loading, but can yield significant errors for other loading states [82].

Lukas [83] proposed that stress intensity factor can be written as

$$K = 1.12 / \sqrt{1 + 4.5a / \rho} \sigma \sqrt{\pi a} \quad (138)$$

Benthem and Koiter [84] proposed a formulae using stress gradient method which can be expressed as

$$K = (1.12\sigma_{\max} + 0.683\partial\sigma / \partial x|_{x=0} a) \sqrt{\pi a} \quad (139)$$

where σ_{\max} is the maximum stress and $\partial\sigma / \partial x$ is the stress gradient.

Jones and Peng [82] proposed a simplified method to calculate the stress intensity factor at notch as

$$K = \left[1 / \sqrt{2} - (1.12 - 1 / \sqrt{2}) \exp(-\alpha \cdot a / \rho) \right] \sigma \sqrt{\pi a} \quad (140)$$

where $\alpha = 0.8[1.0 - 0.3(a / \rho) + 0.13(a / \rho)^2]$ for mode I, and $\alpha = 0.32$ if $a / \rho < 1.3$ and $\alpha = 0.32[1.0 - 0.5(a / \rho - 1.3) / a / \rho]$ if $a / \rho > 1.3$ for mode II.

Jones et al [85] proposed another equation for a semi-elliptical surface flaw as

$$K(\phi) = F \left[\frac{1}{E(K)} (\sin^2 \phi + (c / a)^2 \cos^2 \phi)^{1/4} \right] \sigma \sqrt{\pi a} \quad (141)$$

where $2c$ is the surface length and a is the depth of the surface flaw, ϕ is the angle in the parametric equations of ellipse, $E(K)$ is complete elliptic integral of the second kind, and F is a correction factor considering the notch radius and boundary conditions which can be expressed as

$$F = F_e + (F_s - F_e) e^{-\alpha_\phi \frac{a}{\rho}} \quad (142)$$

Gomez et al [86] used local strain energy to predict the static failure of U-notched plate under mixed-mode I and II loading. The mode I and II stress intensity factors are expressed as

$$K_{\rho,I}^V = \sqrt{2\pi} \frac{(\sigma_{\theta\theta})_{\theta=0} r^{1-\lambda_1}}{1 + \tilde{\omega}_1 (r/r_0)^{\mu_1-\lambda_1}} \quad (143)$$

$$K_{\rho,II}^V = \sqrt{2\pi} \frac{(\tau_{r\theta})_{\theta=0} r^{1-\lambda_2}}{1 + \tilde{\omega}_2 (r/r_0)^{\mu_2-\lambda_2}}$$

This method has been applied for U-notched specimens with notch root radius ranging from 0.2 to 4.0 mm in materials exhibiting a brittle or quasi-brittle behavior [86].

Compared with mode I loading, the problem is more complicated under mixed-mode loading. There is no universally accepted model for fatigue crack growth from a notch under multiaxial fatigue loading and the experimental data for various materials and notch geometries are limited.

The objective of this chapter is to extend the model proposed in Chapter 2 for mixed-mode threshold stress intensity factor and crack growth rate prediction from smooth specimen to notched specimen. The method is developed using local stresses near the U-notch tip rather than remote stresses. Two major advantages of the proposed model are that it can automatically adapt for different failure mechanism, and it is able to capture the influence of notch tip radius on fatigue failure. To predict the fatigue life of the components with blunt crack or U-notch, only the mode I fatigue crack growth data, the crack/notch tip radius, and some material properties are needed.

In the following section, the derivation of the model is demonstrated using a U-notched specimen under remote tension. A multiaxial fatigue limit criterion developed earlier by Liu and Mahadevan [9] is extended to develop a threshold stress intensity factor criterion using the modified Kitagawa-Takahashi diagram [87]. Following this, an equivalent stress intensity factor is proposed for the crack growth rate prediction.

3.2 Proposed mixed-mode I and II fatigue model for notched specimen

3.2.1 Fatigue limit and threshold stress intensity factor for notched specimen

Recently, while dealing with notch sensitivity and defect sensitivity, the Kitagawa-Takahashi diagram [11] which is valid for cracks was extended by Atzori and Lazzarin [87] to notches to create a common equation in the analysis of small cracks, cracks, crack-like notches and common notches, which can be expressed as

$$f_{-1} = \frac{K_{I,th}}{\sqrt{\pi(a+a_0)}} \quad t_{-1} = \frac{K_{II,th}}{\sqrt{\pi(a+a_0)}} \quad (144)$$

where $a_0 = \frac{1}{\pi} \left(\frac{\Delta K_{th}}{\alpha \cdot \Delta \sigma_0} \right)^2$ and α is related to the notch tip radius.

3.2.2 Mixed-mode I and II threshold stress intensity factor

The multiaxial fatigue limit criterion as shown in Eq. (41) can be extended to a mixed-mode threshold stress intensity factor criterion using the Kitagawa-Takahashi diagram for notched specimens, which links the fatigue behavior of notched and unnotched material together. Consider an infinite plate under remote tension and torsional loading as shown in Figure 18. There is a mixed-mode I and II stress field near the U-notch tip, which can be expressed as:

$$\begin{aligned} \sigma_{rr} &= \frac{K_I}{\sqrt{2\pi r}} \cos\left(\frac{\theta}{2}\right) \left(2 - \cos^2\left(\frac{\theta}{2}\right) - \frac{R_0}{r}\right) + \frac{K_{II}}{\sqrt{2\pi r}} \sin\left(\frac{\theta}{2}\right) \left(1 - 3\sin^2\left(\frac{\theta}{2}\right) - \frac{R_0}{r}\right) \\ \sigma_{\theta\theta} &= \frac{K_I}{\sqrt{2\pi r}} \cos\left(\frac{\theta}{2}\right) \left(\cos^2\left(\frac{\theta}{2}\right) + \frac{R_0}{r}\right) + \frac{K_{II}}{\sqrt{2\pi r}} \sin\left(\frac{\theta}{2}\right) \left(-3\cos^2\left(\frac{\theta}{2}\right) + \frac{R_0}{r}\right) \\ \sigma_{zz} &= \begin{cases} 0 & \text{plane stress} \\ \nu(\sigma_{\theta\theta} + \sigma_{rr}) & \text{plane strain} \end{cases} \\ \tau_{r\theta} &= \frac{K_I}{\sqrt{2\pi r}} \sin\left(\frac{\theta}{2}\right) \left(\cos^2\left(\frac{\theta}{2}\right) + \frac{R_0}{r}\right) + \frac{K_{II}}{\sqrt{2\pi r}} \cos\left(\frac{\theta}{2}\right) \left(1 - 3\sin^2\left(\frac{\theta}{2}\right) - \frac{R_0}{r}\right) \end{aligned} \quad (145)$$

where $2R_0$ is equal to the notch tip radius ρ .

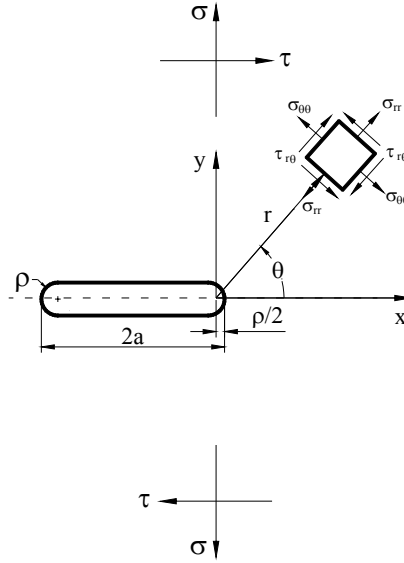


Figure 18. Mixed-mode I and II stress fields near notch tip

For plane stress condition, Eq. (41) can be rewritten as

$$\sqrt{\left(\frac{\sigma_{\theta\theta}}{f_{-1}}\right)^2 + \left(\frac{\tau_{r\theta}}{t_{-1}}\right)^2 + A\left(\frac{\sigma_{\theta\theta} + \sigma_{rr}}{3f_{-1}}\right)^2} = B \quad (146)$$

For plane strain condition, Eq. (41) can be rewritten as

$$\sqrt{\left(\frac{\sigma_{\theta\theta}}{f_{-1}}\right)^2 + \left(\frac{\tau_{r\theta}}{t_{-1}}\right)^2 + A(1+\nu)^2\left(\frac{\sigma_{\theta\theta} + \sigma_{rr}}{3f_{-1}}\right)^2} = B \quad (147)$$

To unify the multiaxial fatigue limit criterion for both plane stress and plane strain conditions, a new parameter A^* is introduced which is the same as A under plane stress condition and equals to $A(1+\nu)^2$ under plane strain condition. Thus Eq. (41) can be expressed as

$$\sqrt{\left(\frac{\sigma_{\theta\theta}}{f_{-1}}\right)^2 + \left(\frac{\tau_{r\theta}}{t_{-1}}\right)^2 + A^* \left(\frac{\sigma_{\theta\theta} + \sigma_{rr}}{3f_{-1}}\right)^2} = B \quad (148)$$

To determine the parameters A^* and B , two extreme cases are considered below:

Case 1: For a fully reversed pure tension fatigue experiment

$$\begin{aligned} K_I &= f_{-1} \sqrt{2\pi r_c} \\ K_{II} &= 0 \end{aligned} \quad (149)$$

where r_c is the characteristic or characteristic distance. From Eq. (145), the stress field near the crack tip can be rewritten as

$$\begin{aligned} \sigma_{rr} &= f_{-1} \cos\left(\frac{\theta}{2}\right) \left(2 - \cos^2\left(\frac{\theta}{2}\right) - \frac{R_0}{r_c}\right) \\ \sigma_{\theta\theta} &= f_{-1} \cos\left(\frac{\theta}{2}\right) \left(\cos^2\left(\frac{\theta}{2}\right) + \frac{R_0}{r_c}\right) \\ \tau_{r\theta} &= f_{-1} \sin\left(\frac{\theta}{2}\right) \left(\cos^2\left(\frac{\theta}{2}\right) + \frac{R_0}{r_c}\right) \end{aligned} \quad (150)$$

Assume $\xi = t_{-1} / f_{-1}$, Eq. (148) can be expressed as

$$\sqrt{\left(\cos\left(\frac{\theta}{2}\right) \left(\cos^2\left(\frac{\theta}{2}\right) + \frac{R_0}{r_c}\right)\right)^2 + \left(\frac{1}{\xi} \sin\left(\frac{\theta}{2}\right) \left(\cos^2\left(\frac{\theta}{2}\right) + \frac{R_0}{r_c}\right)\right)^2 + A^* \left(\frac{2}{3} \cos\left(\frac{\theta}{2}\right)\right)^2} = B \quad (151)$$

Case 2: For a fully reversed pure torsion fatigue experiment

$$\begin{aligned} K_I &= 0 \\ K_{II} &= t_{-1} \sqrt{2\pi r_c} \end{aligned} \quad (152)$$

From Eq. (145) the stress field near crack tip can be rewritten as

$$\begin{aligned}
\sigma_{rr} &= t_{-1} \sin\left(\frac{\theta}{2}\right) \left(1 - 3 \sin^2\left(\frac{\theta}{2}\right) - \frac{R_0}{r_c}\right) \\
\sigma_{\theta\theta} &= t_{-1} \sin\left(\frac{\theta}{2}\right) \left(-3 \cos^2\left(\frac{\theta}{2}\right) + \frac{R_0}{r_c}\right) \\
\tau_{r\theta} &= t_{-1} \cos\left(\frac{\theta}{2}\right) \left(1 - 3 \sin^2\left(\frac{\theta}{2}\right) - \frac{R_0}{r_c}\right)
\end{aligned} \tag{153}$$

Thus Eq. (148) can be expressed as

$$\sqrt{\left(\xi \sin\left(\frac{\theta}{2}\right) \left(-3 \cos^2\left(\frac{\theta}{2}\right) + \frac{R_0}{r_c}\right)\right)^2 + \left(\cos\left(\frac{\theta}{2}\right) \left(1 - 3 \sin^2\left(\frac{\theta}{2}\right) - \frac{R_0}{r_c}\right)\right)^2 + A^* \left(-\frac{2}{3} \xi \sin\left(\frac{\theta}{2}\right)\right)^2} = B \tag{154}$$

According to the maximum tangential stress criterion (MTS), the maximum tangential stress at r_c occurs at the angle of θ , which satisfies

$$\frac{\partial \sigma_{\theta\theta}}{\partial \theta} = 0 \quad \frac{\partial^2 \sigma_{\theta\theta}}{\partial \theta^2} < 0 \tag{155}$$

Thus for case 1, $\theta = 0^\circ$. Then Eq. (151) can be rewritten as

$$\sqrt{\left(1 + \frac{R_0}{r_c}\right)^2 + \frac{4}{9} A^*} = B \tag{156}$$

For case 2, $\theta = -2 \arccos \sqrt{\frac{2}{3} + \frac{1}{9} \frac{R_0}{r_c}} \left(0 \leq \frac{R_0}{r_c} \leq 3\right)$. Then Eq.(154) can be

rewritten as

$$\sqrt{\frac{4}{81} \xi^2 \left(3 - \frac{R_0}{r_c}\right)^3 - \frac{2}{27} \frac{R_0}{r_c} \left(6 + \frac{R_0}{r_c}\right) + \frac{4}{81} \xi^2 A^* \left(3 - \frac{R_0}{r_c}\right)} = B \tag{157}$$

Solving Eq. (156) and (157) for A^* and B ,

$$A^* = \frac{81 + 198\left(\frac{R_0}{r_c}\right) + 87\left(\frac{R_0}{r_c}\right)^2 - 4\xi^2\left(3 - \frac{R_0}{r_c}\right)^3}{4\left[\xi^2\left(3 - \frac{R_0}{r_c}\right) - 9\right]} \quad (158)$$

$$B = \sqrt{\frac{36\left(\frac{R_0}{r_c}\right) + 6\left(\frac{R_0}{r_c}\right)^2 + \xi^2\left(3 - \frac{R_0}{r_c}\right)\left(5\frac{R_0}{r_c} - 3\right)\left(\frac{R_0}{r_c} + 9\right)}{9\left[\xi^2\left(3 - \frac{R_0}{r_c}\right) - 9\right]}}$$

Since A^* is the contribution of damage caused by the hydrostatic stress, A^* and B should be non negative real numbers. The range of ξ needs to be

$$\sqrt{\left(81 + 198\left(\frac{R_0}{r_c}\right) + 87\left(\frac{R_0}{r_c}\right)^2\right) / \left(4\left(3 - \frac{R_0}{r_c}\right)^3\right)} \leq \xi < \sqrt{9} / \left(3 - \frac{R_0}{r_c}\right) \quad (159)$$

Thus the characteristic plane orientation calculated by MTS criterion is only applicable to brittle material.

According to the maximum shear stress criterion (MSS), the maximum shear stress at r_c occurs at the angle θ , which satisfies

$$\frac{\partial \tau_{r\theta}}{\partial \theta} = 0 \quad \frac{\partial^2 \tau_{r\theta}}{\partial \theta^2} < 0 \quad (160)$$

Thus for case 1, $\theta = 2 \arccos \sqrt{\frac{2}{3} - \frac{1}{3} \frac{R_0}{r_c}}$ ($0 \leq \frac{R_0}{r_c} < 2$) and $\theta = -2 \arccos \sqrt{\frac{2}{3} - \frac{1}{3} \frac{R_0}{r_c}}$ ($2 < \frac{R_0}{r_c} \leq 3$).

Then Eq. (151) can be rewritten as

$$\sqrt{\frac{4}{27}\left(2 - \frac{R_0}{r_c}\right)\left(1 + \frac{R_0}{r_c}\right)^2 + \frac{4}{27}\frac{1}{\xi^2}\left(1 + \frac{R_0}{r_c}\right)^3 + \frac{4}{27}A^*\left(2 - \frac{R_0}{r_c}\right)} = B \quad (161)$$

For case 2, $\theta = 0$. Then Eq. (154) can be rewritten as

$$\left|1 - \frac{R_0}{r_c}\right| = B \quad (162)$$

Solving Eqs. (161) and (162) for A^* and B ,

$$A^* = \frac{19 - 66\frac{R_0}{r_c} + 27\left(\frac{R_0}{r_c}\right)^2 + 4\left(\frac{R_0}{r_c}\right)^3 - \frac{4}{\xi^2}\left(1 + \frac{R_0}{r_c}\right)^3}{4\left(2 - \frac{R_0}{r_c}\right)} \quad (163)$$

$$B = \left|1 - \frac{R_0}{r_c}\right|$$

Since A^* and B should be non negative real numbers, the range of ξ needs to be

$$\xi \geq \sqrt{4\left(1 + \frac{R_0}{r_c}\right)^3 / \left(19 - 66\frac{R_0}{r_c} + 27\left(\frac{R_0}{r_c}\right)^2 + 4\left(\frac{R_0}{r_c}\right)^3\right)} \quad (164)$$

Thus the characteristic plane orientation calculated by the MSS criterion is applicable for both brittle and ductile materials. In these two extreme cases (case 1 and case 2) the characteristic plane orientations coincide with the crack orientations predicted by MSS. Therefore the MSS criterion is used below to predict crack orientation β .

The contribution of the hydrostatic stress is different for different materials if the characteristic plane is fixed for all materials. There are two materials for which the contribution of hydrostatic stress is zero. It is also noticed that, if the characteristic plane is fixed, the range of applicable material parameters are limited.

Instead of fixing the characteristic plane, the current model searches for the characteristic plane orientations on which the contribution of the hydrostatic stress is minimized to zero.

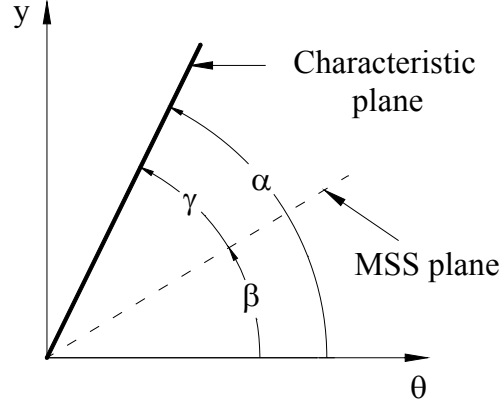


Figure 19. Orientation of characteristic plane and maximum shear stress (MSS) plane

For an arbitrary material, the characteristic plane orientation is assumed to be α (as shown in Figure 19). Since the contribution of the hydrostatic stress is zero, Eq. (148) is rewritten as:

$$\sqrt{\left(\frac{\sigma_{\theta\theta,\alpha}}{f_{-1}}\right)^2 + \left(\frac{\tau_{r\theta,\alpha}}{t_{-1}}\right)^2} = B \quad (165)$$

The objective is to find α and B for an arbitrary material. Following the steps described for the first two cases, Eq. (151) and (154) can be rewritten as

$$\sqrt{\left[\cos\left(\frac{\theta_1 + \gamma}{2}\right)\left(\cos^2\left(\frac{\theta_1 + \gamma}{2}\right) + \frac{R_0}{r_c}\right)\right]^2 + \left[\frac{1}{\xi}\sin\left(\frac{\theta_1 + \gamma}{2}\right)\left(\cos^2\left(\frac{\theta_1 + \gamma}{2}\right) + \frac{R_0}{r_c}\right)\right]^2} = B \quad (166)$$

$$\sqrt{\left[\xi\sin\left(\frac{\theta_2 + \gamma}{2}\right)\left(-3\cos^2\left(\frac{\theta_2 + \gamma}{2}\right) + \frac{R_0}{r_c}\right)\right]^2 + \left[\cos\left(\frac{\theta_2 + \gamma}{2}\right)\left(1 - 3\sin^2\left(\frac{\theta_2 + \gamma}{2}\right) - \frac{R_0}{r_c}\right)\right]^2} = B \quad (167)$$

where $\theta_1 = 2 \arccos \sqrt{\frac{2}{3} - \frac{1}{3} \frac{R_0}{r_c}} \left(0 \leq \frac{R_0}{r_c} < 2\right)$, $\theta_1 = -2 \arccos \sqrt{\frac{2}{3} - \frac{1}{3} \frac{R_0}{r_c}} \left(2 < \frac{R_0}{r_c} \leq 3\right)$ and $\theta_2 = 0$.

It is difficult to obtain a closed form solution for Eqs. (166) and (167). Numerical solutions for γ and B under different R_0/r_c versus material property ξ are shown in Figure 20 and Figure 21.

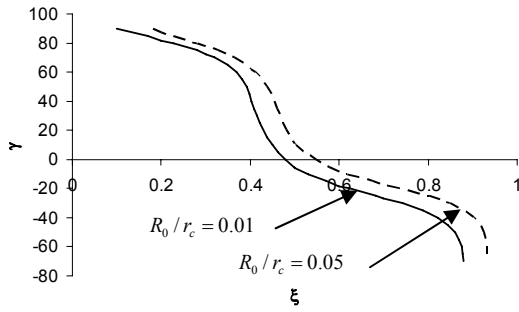


Figure 20. γ .vs. ξ

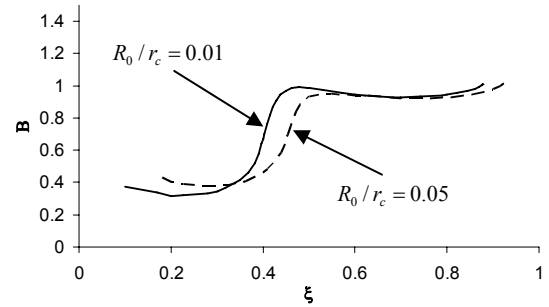


Figure 21. B .vs. ξ

The mixed-mode I and II crack orientation θ can be found using the MSS criterion in Eq. (160). The numerical solution is shown in Figure 22.

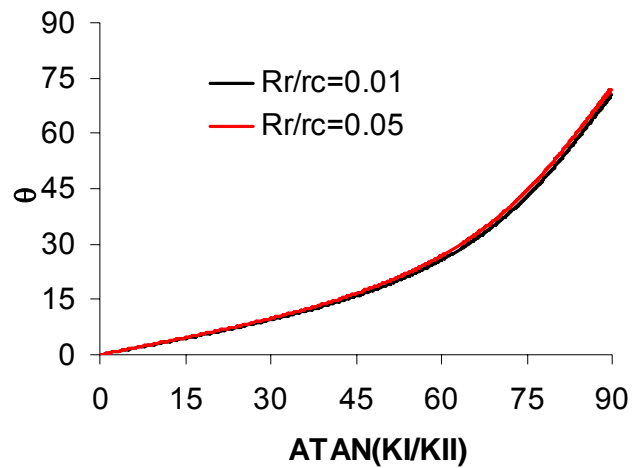


Figure 22. Mixed-mode I and II crack orientation θ using MSS criterion

Then the characteristic plane orientation α can be expressed as

$$\alpha = \theta + \gamma \quad (168)$$

In the proposed method, the characteristic plane depends on mode mixity β , where $\tan \beta$ is equal to the ratio of stress intensity factor K_I / K_{II} , and material ductility ξ , where $\xi = t_{-1} / f_{-1} = K_{II,th} / K_{I,th}$. The parameter ξ is related to two different material failure mechanism. A larger value of ξ indicates tension dominated failure and smaller ξ indicates shear-dominated failure. If the value of ξ is known (based on uniaxial and pure torsional fatigue tests), the proposed model can automatically adapt for different failure mechanism.

3.2.3 Mixed-mode I and II fatigue crack growth

Using the parameter α , Eq. (148) becomes

$$\sqrt{\left(\frac{K_I \cos\left(\frac{\alpha}{2}\right) \left(\cos^2\left(\frac{\alpha}{2}\right) + \frac{R_0}{r_c} \right) + K_{II} \sin\left(\frac{\alpha}{2}\right) \left(-3 \cos^2\left(\frac{\alpha}{2}\right) + \frac{R_0}{r_c} \right)}{K_{I,th}} \right)^2 + \left(\frac{K_I \sin\left(\frac{\alpha}{2}\right) \left(\cos^2\left(\frac{\alpha}{2}\right) + \frac{R_0}{r_c} \right) + K_{II} \cos\left(\frac{\alpha}{2}\right) \left(1 - 3 \sin^2\left(\frac{\alpha}{2}\right) - \frac{R_0}{r_c} \right)}{\xi K_{I,th}} \right)^2} + A^* \left(\frac{2 \cos\left(\frac{\alpha}{2}\right) \left[K_I - K_{II} \tan\left(\frac{\alpha}{2}\right) \right]}{3 K_{I,th}} \right)^2 = B \quad (169)$$

For prediction corresponding to a general crack growth rate da / dN , the threshold stress intensity factors ($K_{I,th}$ and $K_{II,th}$) may be replaced by the stress intensity coefficients at the specific crack growth rate ($K_{I,da/dN}$ and $K_{II,da/dN}$). In the proposed mixed-mode crack growth model, stress intensity coefficients at the specific crack growth rates are considered as equivalent stress intensity factor for mixed-mode case. The mixed-mode crack growth model is expressed as

$$\begin{aligned}
K_{mix,eq} &= \frac{1}{B} \sqrt{\left(K_I \cos\left(\frac{\alpha}{2}\right) \left(\cos^2\left(\frac{\alpha}{2}\right) + \frac{R_0}{r_c} \right) + K_{II} \sin\left(\frac{\alpha}{2}\right) \left(-3 \cos^2\left(\frac{\alpha}{2}\right) + \frac{R_0}{r_c} \right) \right)^2 +} \\
&\quad \left(K_I \sin\left(\frac{\alpha}{2}\right) \left(\cos^2\left(\frac{\alpha}{2}\right) + \frac{R_0}{r_c} \right) + K_{II} \cos\left(\frac{\alpha}{2}\right) \left(1 - 3 \sin^2\left(\frac{\alpha}{2}\right) - \frac{R_0}{r_c} \right) \right)^2} \\
&\quad + \frac{4}{9} A^* \left(\cos\left(\frac{\alpha}{2}\right) \left[K_I - K_{II} \tan\left(\frac{\alpha}{2}\right) \right] \right)^2 \quad (170) \\
&= K_{I,da/dN} = f\left(\frac{da}{dN}\right)
\end{aligned}$$

where $f\left(\frac{da}{dN}\right)$ is the crack growth curve obtained under mode I loading. There are no closed form solutions for Eq.(170). In practical calculation, a trial and error method can be used to find da/dN . For high cycle fatigue problem, $K_{II,da/dN}$ and $K_{I,da/dN}$ take initial values as $K_{II,th}$ and $K_{I,th}$, respectively.

3.3 Proposed mixed-mode I and III fatigue model for notched specimen

3.3.1 Mixed-mode I and III threshold stress intensity factor

The procedure is similar to that for mixed-mode I and III fatigue model for smooth specimen in Chapter 2. Consider an infinite plate under remote tensional and torsional loading as shown in Figure 23, there is a mixed-mode I and III stress field near U notch tip, which can be expressed as:

$$\begin{aligned}
\sigma_{rr} &= \frac{K_I}{\sqrt{2\pi r}} \cos\left(\frac{\theta}{2}\right) \left(2 - \cos^2\left(\frac{\theta}{2}\right) - \frac{R_0}{r} \right) \\
\sigma_{\theta\theta} &= \frac{K_I}{\sqrt{2\pi r}} \cos\left(\frac{\theta}{2}\right) \left(\cos^2\left(\frac{\theta}{2}\right) + \frac{R_0}{r} \right) \\
\sigma_{zz} &= \begin{cases} 0 & \text{plane stress} \\ \nu(\sigma_{\theta\theta} + \sigma_{rr}) & \text{plane strain} \end{cases} \\
\tau_{r\theta} &= \frac{K_I}{\sqrt{2\pi r}} \sin\left(\frac{\theta}{2}\right) \left(\cos^2\left(\frac{\theta}{2}\right) + \frac{R_0}{r} \right) \\
\tau_{rz} &= \frac{K_{III}}{\sqrt{2\pi r}} \sin\left(\frac{\theta}{2}\right) \\
\tau_{\theta z} &= \frac{K_{III}}{\sqrt{2\pi r}} \cos\left(\frac{\theta}{2}\right)
\end{aligned} \quad (171)$$

$$\begin{aligned}
\sigma_{r'r'} &= \frac{1}{\sqrt{2\pi r}} \cos\left(\frac{\theta}{2}\right) \left[K_I \left(2 - \cos^2\left(\frac{\theta}{2}\right) - \frac{R_0}{r} \right) \right] \\
\sigma_{\theta'\theta'} &= \frac{1}{\sqrt{2\pi r}} \cos\left(\frac{\theta}{2}\right) \left[K_I \left(\left(\cos^2\left(\frac{\theta}{2}\right) + \frac{R_0}{r} \right) \cos^2(\beta) + 2\nu \sin^2(\beta) \right) + K_{III} \sin(2\beta) \right] \\
\sigma_{z'z'} &= \frac{1}{\sqrt{2\pi r}} \cos\left(\frac{\theta}{2}\right) \left[K_I \left(\left(\cos^2\left(\frac{\theta}{2}\right) + \frac{R_0}{r} \right) \sin^2(\beta) + 2\nu \cos^2(\beta) \right) - K_{III} \sin(2\beta) \right] \\
\tau_{r'\theta'} &= \frac{1}{\sqrt{2\pi r}} \sin\left(\frac{\theta}{2}\right) \left[K_I \left(\cos^2\left(\frac{\theta}{2}\right) + \frac{R_0}{r} \right) \cos(\beta) + K_{III} \sin(\beta) \right] \\
\tau_{r'z'} &= \frac{1}{\sqrt{2\pi r}} \sin\left(\frac{\theta}{2}\right) \left[-K_I \left(\cos^2\left(\frac{\theta}{2}\right) + \frac{R_0}{r} \right) \sin(\beta) + K_{III} \cos(\beta) \right] \\
\tau_{\theta'z'} &= \frac{1}{\sqrt{2\pi r}} \cos\left(\frac{\theta}{2}\right) \left[K_I \left(\nu - \frac{1}{2} \left(\cos^2\left(\frac{\theta}{2}\right) + \frac{R_0}{r} \right) \right) \sin(2\beta) + K_{III} \cos(2\beta) \right]
\end{aligned} \tag{173}$$

Under plane stress condition, Eq. (172) can be expressed as

$$\begin{aligned}
\sigma_{r'r'} &= \frac{1}{\sqrt{2\pi r}} \cos\left(\frac{\theta}{2}\right) \left[K_I \left(2 - \cos^2\left(\frac{\theta}{2}\right) - \frac{R_0}{r} \right) \right] \\
\sigma_{\theta'\theta'} &= \frac{1}{\sqrt{2\pi r}} \cos\left(\frac{\theta}{2}\right) \left[K_I \left(\cos^2\left(\frac{\theta}{2}\right) + \frac{R_0}{r} \right) \cos^2(\beta) + K_{III} \sin(2\beta) \right] \\
\sigma_{z'z'} &= \frac{1}{\sqrt{2\pi r}} \cos\left(\frac{\theta}{2}\right) \left[K_I \left(\cos^2\left(\frac{\theta}{2}\right) + \frac{R_0}{r} \right) \sin^2(\beta) - K_{III} \sin(2\beta) \right] \\
\tau_{r'\theta'} &= \frac{1}{\sqrt{2\pi r}} \sin\left(\frac{\theta}{2}\right) \left[K_I \left(\cos^2\left(\frac{\theta}{2}\right) + \frac{R_0}{r} \right) \cos(\beta) + K_{III} \sin(\beta) \right] \\
\tau_{r'z'} &= \frac{1}{\sqrt{2\pi r}} \sin\left(\frac{\theta}{2}\right) \left[-K_I \left(\cos^2\left(\frac{\theta}{2}\right) + \frac{R_0}{r} \right) \sin(\beta) + K_{III} \cos(\beta) \right] \\
\tau_{\theta'z'} &= \frac{1}{\sqrt{2\pi r}} \cos\left(\frac{\theta}{2}\right) \left[-\frac{1}{2} K_I \left(\cos^2\left(\frac{\theta}{2}\right) + \frac{R_0}{r} \right) \sin(2\beta) + K_{III} \cos(2\beta) \right]
\end{aligned} \tag{174}$$

Thus for mixed mode I and III under either plane strain or plane stress condition, the fatigue limit criterion becomes

$$\sqrt{\left(\frac{\sigma_{\theta'\theta'}}{f_{-1}}\right)^2 + \left(\frac{\tau_{r'\theta'}}{t_{-1}}\right)^2 + \left(\frac{\tau_{\theta'z'}}{t_{-1}}\right)^2 + A \left(\frac{\sigma_{\theta'\theta'} + \sigma_{z'z'} + \sigma_{r'r'}}{3f_{-1}}\right)^2} = B \tag{175}$$

where $-\pi \leq \theta \leq \pi$ and $-\pi/2 \leq \beta \leq \pi/2$. To determine the parameters A and B , two extreme cases are considered below:

Case 1: For a fully reversed pure tensional fatigue experiment

$$\begin{aligned} K_I &= f_{-1} \sqrt{2\pi r_c} \\ K_{III} &= 0 \end{aligned} \quad (176)$$

where r_c is the characteristic or characteristic distance. From Eqs.(173), (174) and (176)

the stress field near crack tip can be rewritten as

(a) Under plane strain condition:

$$\begin{aligned} \sigma_{r'r'} &= f_{-1} \cos\left(\frac{\theta}{2}\right) \left(2 - \cos^2\left(\frac{\theta}{2}\right) - \frac{R_0}{r}\right) \\ \sigma_{\theta'\theta'} &= f_{-1} \cos\left(\frac{\theta}{2}\right) \left[\left(\cos^2\left(\frac{\theta}{2}\right) + \frac{R_0}{r}\right) \cos^2(\beta) + 2\nu \sin^2(\beta) \right] \\ \sigma_{z'z'} &= f_{-1} \cos\left(\frac{\theta}{2}\right) \left[\left(\cos^2\left(\frac{\theta}{2}\right) + \frac{R_0}{r}\right) \sin^2(\beta) + 2\nu \cos^2(\beta) \right] \\ \tau_{r'\theta'} &= f_{-1} \sin\left(\frac{\theta}{2}\right) \left(\cos^2\left(\frac{\theta}{2}\right) + \frac{R_0}{r}\right) \cos(\beta) \\ \tau_{r'z'} &= -f_{-1} \sin\left(\frac{\theta}{2}\right) \left(\cos^2\left(\frac{\theta}{2}\right) + \frac{R_0}{r}\right) \sin(\beta) \\ \tau_{\theta'z'} &= f_{-1} \cos\left(\frac{\theta}{2}\right) \left(\nu - \frac{1}{2} \left(\cos^2\left(\frac{\theta}{2}\right) + \frac{R_0}{r}\right)\right) \sin(2\beta) \end{aligned} \quad (177)$$

(b) Under plane stress condition:

$$\begin{aligned} \sigma_{r'r'} &= f_{-1} \cos\left(\frac{\theta}{2}\right) \left(2 - \cos^2\left(\frac{\theta}{2}\right) - \frac{R_0}{r}\right) \\ \sigma_{\theta'\theta'} &= f_{-1} \cos\left(\frac{\theta}{2}\right) \left(\cos^2\left(\frac{\theta}{2}\right) + \frac{R_0}{r}\right) \cos^2(\beta) \\ \sigma_{z'z'} &= f_{-1} \cos\left(\frac{\theta}{2}\right) \left(\cos^2\left(\frac{\theta}{2}\right) + \frac{R_0}{r}\right) \sin^2(\beta) \\ \tau_{r'\theta'} &= f_{-1} \sin\left(\frac{\theta}{2}\right) \left(\cos^2\left(\frac{\theta}{2}\right) + \frac{R_0}{r}\right) \cos(\beta) \\ \tau_{r'z'} &= -f_{-1} \sin\left(\frac{\theta}{2}\right) \left(\cos^2\left(\frac{\theta}{2}\right) + \frac{R_0}{r}\right) \sin(\beta) \\ \tau_{\theta'z'} &= -\frac{1}{2} f_{-1} \cos\left(\frac{\theta}{2}\right) \left(\cos^2\left(\frac{\theta}{2}\right) + \frac{R_0}{r}\right) \sin(2\beta) \end{aligned} \quad (178)$$

Assuming $\xi = t_{-1} / f_{-1}$, Eq. (175) can be expressed as

(a) Under plane strain condition:

$$\sqrt{\left[\cos\left(\frac{\theta}{2}\right) \left[\cos^2\left(\frac{\theta}{2}\right) + \frac{R_0}{r} \right] \cos^2(\beta) + 2\nu \sin^2(\beta) \right]^2 + \left[\frac{\sin\left(\frac{\theta}{2}\right) \left(\cos^2\left(\frac{\theta}{2}\right) + \frac{R_0}{r} \right) \cos(\beta)}{\xi} \right]^2 + \left[\frac{\cos\left(\frac{\theta}{2}\right) \left(\nu - \frac{1}{2} \left(\cos^2\left(\frac{\theta}{2}\right) + \frac{R_0}{r} \right) \right) \sin(2\beta)}{\xi} \right]^2 + A \left(\frac{2 \cos\left(\frac{\theta}{2}\right) (1 + \nu)}{3} \right)^2} = B \quad (179)$$

(b) Under plane stress condition:

$$\sqrt{\left[\cos\left(\frac{\theta}{2}\right) \left(\cos^2\left(\frac{\theta}{2}\right) + \frac{R_0}{r} \right) \cos^2(\beta) \right]^2 + \left[\frac{\sin\left(\frac{\theta}{2}\right) \left(\cos^2\left(\frac{\theta}{2}\right) + \frac{R_0}{r} \right) \cos(\beta)}{\xi} \right]^2 + \left[\frac{\cos\left(\frac{\theta}{2}\right) \left(\cos^2\left(\frac{\theta}{2}\right) + \frac{R_0}{r} \right) \sin(2\beta)}{2\xi} \right]^2 + \frac{4}{9} A \cos^2\left(\frac{\theta}{2}\right)} = B \quad (180)$$

Case 2: For a fully reversed pure torsion fatigue experiment

$$\begin{aligned} K_I &= 0 \\ K_{III} &= t_{-1} \sqrt{2\pi r_c} \end{aligned} \quad (181)$$

From Eqs.(173), (174) and (181) the stress field near crack tip for both plane strain and plane stress condition can be rewritten as

$$\begin{aligned} \sigma_{r'r'} &= 0 \\ \sigma_{\theta'\theta'} &= t_{-1} \cos\left(\frac{\theta}{2}\right) \sin(2\beta) \\ \sigma_{z'z'} &= -t_{-1} \cos\left(\frac{\theta}{2}\right) \sin(2\beta) \\ \tau_{r'\theta'} &= t_{-1} \sin\left(\frac{\theta}{2}\right) \sin(\beta) \\ \tau_{r'z'} &= t_{-1} \sin\left(\frac{\theta}{2}\right) \cos(\beta) \\ \tau_{\theta'z'} &= t_{-1} \cos\left(\frac{\theta}{2}\right) \cos(2\beta) \end{aligned} \quad (182)$$

Thus Eq. (175) can be expressed as

$$\sqrt{\left(\xi \cos\left(\frac{\theta}{2}\right) \sin(2\beta) \right)^2 + \left(\sin\left(\frac{\theta}{2}\right) \sin(\beta) \right)^2 + \left(\cos\left(\frac{\theta}{2}\right) \cos(2\beta) \right)^2} = B \quad (183)$$

According to the maximum tangential stress criterion (MTS), the maximum tangential stress at r_c occurs at the angle θ , which satisfies

$$\frac{\partial \sigma_{\theta\theta'}}{\partial \beta} = 0 \quad \frac{\partial \sigma_{\theta\theta'}}{\partial \theta} = 0 \quad \frac{\partial^2 \sigma_{\theta\theta'}}{\partial \beta^2} < 0 \quad \frac{\partial^2 \sigma_{\theta\theta'}}{\partial \beta^2} \frac{\partial^2 \sigma_{\theta\theta'}}{\partial \theta^2} - \left(\frac{\partial^2 \sigma_{\theta\theta'}}{\partial \beta \partial \theta} \right)^2 > 0 \quad (184)$$

Thus in case 1 under plane strain condition, $\beta = 0$ and $\theta = 0$ at $\nu < 0.5 + (R_0/r)/2$ and under plane stress condition, $\beta = 0$ and $\theta = 0$. Then Eq. (179) for plane strain can be rewritten as:

$$\sqrt{\left(1 + \frac{R_0}{r}\right)^2 + \frac{4}{9}(1+\nu)^2} A = B \quad (185)$$

Eq. (180) for plane stress can be rewritten as:

$$\sqrt{\left(1 + \frac{R_0}{r}\right)^2 + \frac{4}{9}A} = B \quad (186)$$

In case 2, $\beta = \pi/4$ and $\theta = 0$ for both plane strain and plane stress. Then Eq. (183) can be rewritten as

$$\xi = B \quad (187)$$

Solving Eqs. (185) and (187) for A and B under plane strain condition,

$$A = \frac{9}{4} \frac{\xi^2 - (1 + R_0/r)^2}{(1+\nu)^2} \quad (188)$$

$$B = \xi$$

Since A and B should be non-negative real numbers, the range of ξ needs to be

$$\xi \geq 1 + R_0/r \quad (189)$$

Solving Eqs. (186) and (187) for A and B in plane stress condition,

$$A = \frac{9}{4} [\xi^2 - (1 + R_0/r)^2] \quad (190)$$

$$B = \xi$$

Since A and B should be non-negative real numbers, the range of ξ needs to be

$$\xi \geq 1 + R_0/r \quad (191)$$

Thus the characteristic plane orientation calculated by MTS criterion is only applicable to brittle materials.

According to the maximum shear stress criteria (MSS), the maximum shear stress at r_c occurs at the angel of θ , which satisfies

$$\frac{\partial \tau_{\theta'z'}}{\partial \beta} = 0 \quad \frac{\partial \tau_{\theta'z'}}{\partial \theta} = 0 \quad \frac{\partial^2 \tau_{\theta'z'}}{\partial \beta^2} < 0 \quad \frac{\partial^2 \tau_{\theta'z'}}{\partial \beta^2} \frac{\partial^2 \tau_{\theta'z'}}{\partial \theta^2} - \left(\frac{\partial^2 \tau_{\theta'z'}}{\partial \beta \partial \theta} \right)^2 > 0 \quad (192)$$

Thus in case 1 for plane strain $\beta = -\pi/4$ and $\theta = 0$ at $0 < \nu \leq \frac{3}{8} + \frac{1}{2} \frac{R_0}{r}$ (for most metals

$0.29 \leq \nu \leq 0.37$) and $\beta = \pi/4$ and $\theta = \pm 2 \arccos(\sqrt{(2\nu - R_0/r)/3})$ at $\frac{3}{8} + \frac{1}{2} \frac{R_0}{r} < \nu < \frac{3}{2} + \frac{1}{2} \frac{R_0}{r}$.

For plane stress condition, $\beta = -\pi/4$ and $\theta = 0$. Then Eq. (179) for plane strain can be rewritten as:

$$\sqrt{\frac{1}{2} \left(1 + \frac{R_0}{r} + \nu \right)^2 + \left[\frac{1}{\xi} \left(\nu - \frac{1}{2} \left(1 + \frac{R_0}{r} \right) \right) \right]^2} + A \frac{4}{9} (1 + \nu)^2 = B \quad @ 0 < \nu \leq \frac{3}{8} + \frac{1}{2} \frac{R_0}{r}$$

$$\sqrt{\left(\frac{2}{3} \nu - \frac{1}{3} \frac{R_0}{r} \right) \left(\frac{4}{3} \nu + \frac{1}{3} \frac{R_0}{r} \right)^2 + \frac{1}{\xi^2} \left[\frac{4}{27} \nu^3 + \frac{2}{9} \nu^2 - \frac{18}{27} \nu^2 \frac{R_0}{r} + \frac{4}{9} \nu \frac{R_0}{r} + \frac{6}{27} \nu \left(\frac{R_0}{r} \right)^2 + \frac{2}{9} \left(\frac{R_0}{r} \right)^2 - \frac{1}{27} \left(\frac{R_0}{r} \right)^3 \right]} + A \frac{4}{9} (1 + \nu)^2 \left(\frac{2}{3} \nu - \frac{1}{3} \frac{R_0}{r} \right) = B \quad (193)$$

$$@ \frac{3}{8} + \frac{1}{2} \frac{R_0}{r} < \nu < \frac{3}{2} + \frac{1}{2} \frac{R_0}{r}$$

Eq. (180) for plane stress can be rewritten as:

$$\sqrt{\frac{1}{4} \left(1 + \frac{R_0}{r} \right)^2 + \frac{1}{4 \xi^2} \left(1 + \frac{R_0}{r} \right)^2} + \frac{4}{9} A = B \quad (194)$$

In case 2 for both plane strain and plane stress condition: $\theta = 0$ and $\beta = 0$. Eq. (183) can be rewritten as

$$1 = B \quad (195)$$

Solving Eqs. (193) and (195) for A and B in plane strain condition

$$A = \frac{9}{4} \frac{1}{(1+\nu)^2} \left[1 - \left[\frac{1}{2} \left(1 + \frac{R_0}{r} \right) + \nu \right]^2 - \left[\frac{1}{\xi} \left(\nu - \frac{1}{2} \left(1 + \frac{R_0}{r} \right) \right) \right]^2 \right] \quad \left(0 < \nu \leq \frac{3}{8} + \frac{1}{2} \frac{R_0}{r} \right) \quad (196)$$

$$B = 1$$

and

$$A = \frac{1 - \left(\frac{2}{3} \nu - \frac{1}{3} \frac{R_0}{r} \right) \left(\frac{4}{3} \nu + \frac{1}{3} \frac{R_0}{r} \right)^2 - \frac{1}{\xi^2} \left[\frac{4}{27} \nu^3 + \frac{2}{9} \nu^2 - \frac{18}{27} \nu^2 \frac{R_0}{r} + \frac{4}{9} \nu \frac{R_0}{r} + \frac{6}{27} \nu \left(\frac{R_0}{r} \right)^2 + \frac{2}{9} \left(\frac{R_0}{r} \right)^2 - \frac{1}{27} \left(\frac{R_0}{r} \right)^3 \right]}{\frac{4}{9} (1+\nu)^2 \left(\frac{2}{3} \nu - \frac{1}{3} \frac{R_0}{r} \right)} \quad (197)$$

$$B = 1 \quad \left(\frac{3}{8} + \frac{1}{2} \frac{R_0}{r} < \nu < \frac{3}{2} + \frac{1}{2} \frac{R_0}{r} \right)$$

Since A and B should be non negative real numbers, the range of ξ needs to be

$$\xi \geq \sqrt{\frac{[\nu - (1 + R_0/r)/2]^2}{1 - [\nu + (1 + R_0/r)/2]^2}} \quad \left(0 < \nu \leq \frac{3}{8} + \frac{1}{2} \frac{R_0}{r} \right)$$

$$\xi \geq \sqrt{\frac{\frac{4}{27} \nu^3 + \frac{2}{9} \nu^2 - \frac{18}{27} \nu^2 \frac{R_0}{r} + \frac{4}{9} \nu \frac{R_0}{r} + \frac{6}{27} \nu \left(\frac{R_0}{r} \right)^2 + \frac{2}{9} \left(\frac{R_0}{r} \right)^2 - \frac{1}{27} \left(\frac{R_0}{r} \right)^3}{1 - \left(\frac{2}{3} \nu - \frac{1}{3} \frac{R_0}{r} \right) \left(\frac{4}{3} \nu + \frac{1}{3} \frac{R_0}{r} \right)^2}} \quad \left(\frac{3}{8} + \frac{1}{2} \frac{R_0}{r} < \nu < \frac{3}{2} + \frac{1}{2} \frac{R_0}{r} \right) \quad (198)$$

Solving Eqs. (194) and (195) for A and B in plane stress condition

$$A = \frac{9}{4} - \frac{9}{16} \left(1 + \frac{1}{\xi^2} \right) \left(1 + \frac{R_0}{r} \right)^2 \quad (199)$$

$$B = 1$$

Since A and B should be non negative real numbers, the range of ξ needs to be

$$\xi \geq \frac{\left(1 + \frac{R_0}{r} \right)}{\sqrt{4 - \left(1 + \frac{R_0}{r} \right)^2}} \quad (200)$$

Thus the characteristic plane orientation calculated by MSS criterion is applicable for both brittle and ductile materials. In these two extreme cases (case 1 and case 2) the

characteristic plane orientations coincide with the crack orientations predicted by MSS. Therefore the MSS criterion is used below to predict crack orientation θ .

Instead of fixing the characteristic plane, the current model searches for the characteristic plane orientations on which the contribution of the hydrostatic stress is minimized to zero.

For an arbitrary material, the characteristic plane orientation is assumed to be α (as shown in Figure 24). Since the contribution of the hydrostatic stress is zero, Eq. (175) is rewritten as:

$$\sqrt{\left(\frac{\sigma_{\theta'\theta',\alpha}}{f_{-1}}\right)^2 + \left(\frac{\tau_{r'\theta',\alpha}}{t_{-1}}\right)^2 + \left(\frac{\tau_{\theta'z',\alpha}}{t_{-1}}\right)^2} = B \quad (201)$$

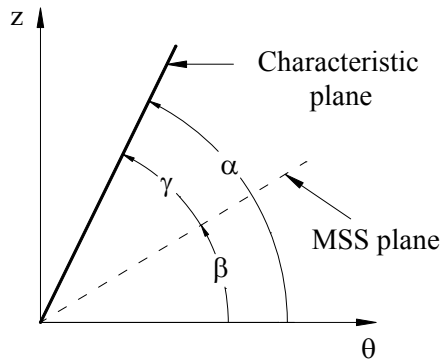


Figure 24. Orientation of characteristic plane and maximum shear stress (MSS) plane for mixed-mode I+III in notched specimens

The objective is to find α and B for an arbitrary material. Following the steps described for the first two cases, for plane strain condition Eqs. (179) and (183) can be rewritten as

$$\sqrt{\left[\left(1 + \frac{R_0}{r}\right) \cos^2(\beta_1 + \gamma) + 2\nu \sin^2(\beta_1 + \gamma)\right]^2 + \left[\frac{\left(\nu - \frac{1}{2}\left(1 + \frac{R_0}{r}\right)\right) \sin(2(\beta_1 + \gamma))}{\xi}\right]^2} = B \quad (202)$$

$$\sqrt{(\xi \sin(2(\beta_2 + \gamma)))^2 + (\cos(2(\beta_2 + \gamma)))^2} = B \quad (203)$$

where $\beta_1 = -\pi/4$ $\beta_2 = 0$. Solving Eqs. (202) and (203)

$$\sin(2\gamma) = \begin{cases} \frac{[\nu + (1 + R_0/r)/2] + [\nu - (1 + R_0/r)/2] - 1}{2\nu^2 - (1 + R_0/r)^2/2} & (\xi = 1) \\ \frac{[\nu^2 - (1 + R_0/r)^2/4] \pm \sqrt{[\nu^2 - (1 + R_0/r)^2/4]^2 - (1 - 1/\xi^2)[\nu - (1 + R_0/r)/2]^2 - \xi^2[\nu + (1 + R_0/r)/2]^2 + [\nu - (1 + R_0/r)/2]^2/\xi^2 - 1}}{(1 - 1/\xi^2)[\nu - (1 + R_0/r)/2]^2 - \xi^2} & (0.31408 < \xi < 1) \end{cases} \quad (204)$$

$$B = \sqrt{1 + (\xi^2 - 1)\sin^2(2\gamma)}$$

For plane stress condition Eqs. (180) and (183) can be rewritten as

$$\sqrt{\left[\left(1 + \frac{R_0}{r}\right) \cos^2(\beta_1 + \gamma)\right]^2 + \left[\frac{\left(1 + \frac{R_0}{r}\right) \sin(2(\beta_1 + \gamma))}{2\xi}\right]^2} = B \quad (205)$$

$$\sqrt{(\xi \sin(2(\beta_2 + \gamma)))^2 + (\cos(2(\beta_2 + \gamma)))^2} = B \quad (206)$$

where $\beta_1 = -\pi/4$ $\beta_2 = 0$. Solving Eqs. (205) and (206)

$$\sin(2\gamma) = \begin{cases} \frac{-(1 + R_0/r) \pm \sqrt{(1 + R_0/r)^4 - [4 - 4\xi^2 + (1 - 1/\xi^2)(1 + R_0/r)^2][1 + 1/\xi^2](1 + R_0/r)^2 - 4}}{4 - 4\xi^2 + (1 - 1/\xi^2)(1 + R_0/r)^2} & (\sqrt{3}/3 \leq \xi < 1) \\ 1 & (\xi = 1) \end{cases} \quad (207)$$

$$B = \sqrt{1 + (\xi^2 - 1)\sin^2(2\gamma)}$$

For mixed mode I and III crack θ and β can be solved from MSS criteria

Under plane strain condition

$$\tau_{\theta'z'} = \frac{1}{\sqrt{2\pi r}} \left[K_I \left(\nu - \frac{1}{2} \left(1 + \frac{R_0}{r} \right) \right) \sin(2\beta) + K_{III} \cos(2\beta) \right] \quad (208)$$

Apply Eq. (88) to Eq. (104)

$$\begin{aligned} \theta &= 0 \\ \tan(2\beta) &= \frac{K_I}{K_{III}} \left[\nu - \frac{1}{2} \left(1 + \frac{R_0}{r} \right) \right] \end{aligned} \quad (209)$$

Under plane stress condition

$$\tau_{\theta'z'} = \frac{1}{\sqrt{2\pi r}} \left[-\frac{1}{2} K_I \left(1 + \frac{R_0}{r} \right) \sin(2\beta) + K_{III} \cos(2\beta) \right] \quad (210)$$

Apply Eq. (88) to Eq. (106)

$$\begin{aligned} \theta &= 0 \\ \tan(2\beta) &= -\frac{K_I}{2K_{III}} \left(1 + \frac{R_0}{r} \right) \end{aligned} \quad (211)$$

The relationships between β and K_I / K_{III} are plotted in Figure 25.

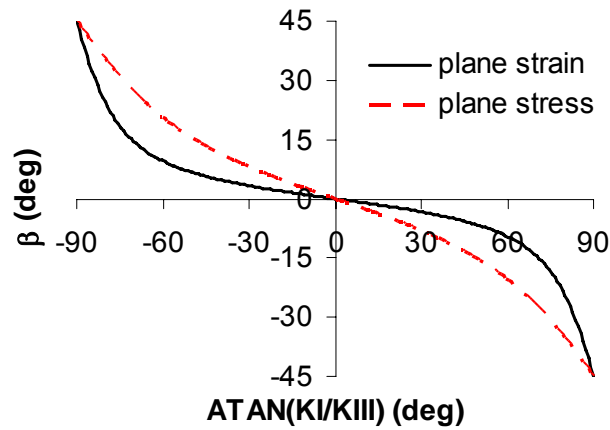


Figure 25. Mixed-mode I and III crack orientation β using the MSS criterion ($\nu = 0.3$ in plane strain)

Then the characteristic plane angle α can be calculated as

$$\alpha = \beta + \gamma \quad (212)$$

3.3.2 Mixed-mode I and III fatigue crack growth

Using the parameter α , Eq. (175) becomes

$$\sqrt{\left[\frac{K_I \left(\left(1 + \frac{R_0}{r}\right) \cos^2(\alpha) + 2\nu \sin^2(\alpha) \right) + K_{III} \sin(2\alpha)}{K_{I,th}} \right]^2 + \left[\frac{K_I \left(\nu - \frac{1}{2} \left(1 + \frac{R_0}{r}\right) \right) \sin(2\alpha) + K_{III} \cos(2\alpha)}{\xi K_{I,th}} \right]^2} + \frac{4}{9} A \left[\frac{(1+\nu)K_I}{K_{I,th}} \right]^2 = B \quad (213)$$

for plane strain condition and

$$\sqrt{\left[\frac{K_I \left(1 + \frac{R_0}{r}\right) \cos^2(\alpha) + K_{III} \sin(2\alpha)}{K_{I,th}} \right]^2 + \left[\frac{K_I \left(-\frac{1}{2} \left(1 + \frac{R_0}{r}\right) \right) \sin(2\alpha) + K_{III} \cos(2\alpha)}{\xi K_{I,th}} \right]^2} + \frac{4}{9} A \left[\frac{K_I}{K_{I,th}} \right]^2 = B \quad (214)$$

for plane stress condition.

For prediction corresponding to a general crack growth rate da/dN , the threshold stress intensity factors ($K_{I,th}$ and $K_{III,th}$) may be replaced by the stress intensity coefficients at the specific crack growth rate ($K_{I,da/dN}$ and $K_{III,da/dN}$). In the proposed mixed mode crack growth model, stress intensity coefficients at the specific crack growth rates are considered as equivalent stress intensity factor for mixed mode case. The mixed mode crack growth model is expressed as follows:

For plane strain condition

$$K_{mix,eq} = \frac{1}{B} \sqrt{\left(K_I \left(\left(1 + \frac{R_0}{r}\right) \cos^2(\alpha) + K_{III} \sin(2\alpha) \right) \right)^2 + \left(K_I \left(-\frac{1}{2} \left(1 + \frac{R_0}{r}\right) \right) \sin(2\alpha) + K_{III} \cos(2\alpha) \right)^2} + A \left(\frac{2(1+\nu)K_I}{3} \right)^2 = K_{I,da/dN} = f \left(\frac{da}{dN} \right) \quad (215)$$

For plane stress condition

$$K_{mix,eq} = \frac{1}{B} \sqrt{\left(K_I \left(1 + \frac{R_0}{r}\right) \cos^2(\alpha) + K_{III} \sin(2\alpha) \right)^2 + \left(\frac{K_I \left(-\frac{1}{2} \left(1 + \frac{R_0}{r}\right) \right) \sin(2\alpha) + K_{III} \cos(2\alpha)}{\xi} \right)^2} + A \left(\frac{2K_I}{3} \right)^2 = K_{I,da/dN} = f \left(\frac{da}{dN} \right) \quad (216)$$

where $f\left(\frac{da}{dN}\right)$ is the crack growth curve obtained under mode I loading. There are no closed form solutions for Eqs . (215) and (216). In practical calculation, a trial and error method can be used to find da/dN . For high cycle fatigue problem, $K_{III,da/dN}$ and $K_{I,da/dN}$ take initial values as $K_{III,th}$ and $K_{I,th}$, respectively.

3.4 Proposed mixed-mode I, II and III fatigue model for notched specimen

3.4.1 Mixed-mode I, II and III threshold stress intensity factor

Consider an infinite plate under remote normal and out of plane shear stress as shown in Figure 26, there is a mixed-mode I, II and III stress field near crack tip, which can be expressed as:

$$\begin{aligned}
\sigma_{rr} &= \frac{K_I}{\sqrt{2\pi r}} \cos\left(\frac{\theta}{2}\right) \left(2 - \cos^2\left(\frac{\theta}{2}\right) - \frac{R_0}{r}\right) + \frac{K_{II}}{\sqrt{2\pi r}} \sin\left(\frac{\theta}{2}\right) \left(1 - 3\sin^2\left(\frac{\theta}{2}\right) - \frac{R_0}{r}\right) \\
\sigma_{\theta\theta} &= \frac{K_I}{\sqrt{2\pi r}} \cos\left(\frac{\theta}{2}\right) \left(\cos^2\left(\frac{\theta}{2}\right) + \frac{R_0}{r}\right) + \frac{K_{II}}{\sqrt{2\pi r}} \sin\left(\frac{\theta}{2}\right) \left(-3\cos^2\left(\frac{\theta}{2}\right) + \frac{R_0}{r}\right) \\
\sigma_{zz} &= \begin{cases} 0 & \text{plane stress} \\ \nu(\sigma_{\theta\theta} + \sigma_{rr}) & \text{plane strain} \end{cases} \\
\tau_{r\theta} &= \frac{K_I}{\sqrt{2\pi r}} \sin\left(\frac{\theta}{2}\right) \left(\cos^2\left(\frac{\theta}{2}\right) + \frac{R_0}{r}\right) + \frac{K_{II}}{\sqrt{2\pi r}} \cos\left(\frac{\theta}{2}\right) \left(1 - 3\sin^2\left(\frac{\theta}{2}\right) - \frac{R_0}{r}\right) \\
\tau_{rz} &= \frac{K_{III}}{\sqrt{2\pi r}} \sin\left(\frac{\theta}{2}\right) \\
\tau_{\theta z} &= \frac{K_{III}}{\sqrt{2\pi r}} \cos\left(\frac{\theta}{2}\right)
\end{aligned} \tag{217}$$

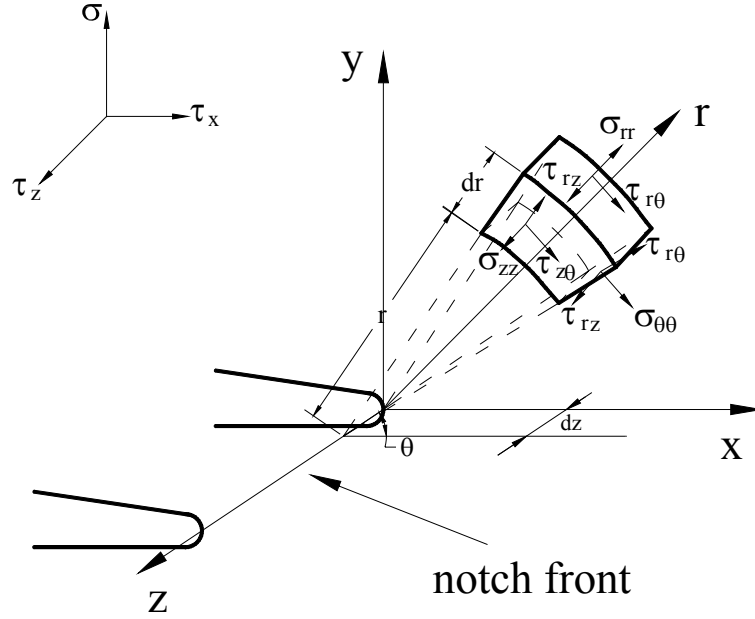


Figure 26. Mixed-mode I, II and III stress fields near notch tip

Experimental data shows that the failure surface under mixed mode I, II and III loading condition is typically non-planar. Assume coordinate (r, θ, z) rotates β around axis r to coordinate (r', θ', z') , the stress in the new coordinate can be expressed as

$$\begin{aligned}
 \sigma_{r'r'} &= \sigma_{rr} \\
 \sigma_{\theta'\theta'} &= \frac{\sigma_{\theta\theta} + \sigma_{zz}}{2} + \frac{\sigma_{\theta\theta} - \sigma_{zz}}{2} \cos(2\beta) + \tau_{\theta z} \sin(2\beta) \\
 \sigma_{z'z'} &= \frac{\sigma_{\theta\theta} + \sigma_{zz}}{2} - \frac{\sigma_{\theta\theta} - \sigma_{zz}}{2} \cos(2\beta) - \tau_{\theta z} \sin(2\beta) \\
 \tau_{r'\theta'} &= \tau_{r\theta} \cos(\beta) + \tau_{rz} \sin(\beta) \\
 \tau_{r'z'} &= -\tau_{r\theta} \sin(\beta) + \tau_{rz} \cos(\beta) \\
 \tau_{\theta'z'} &= -\frac{\sigma_{\theta\theta} - \sigma_{zz}}{2} \sin(2\beta) + \tau_{\theta z} \cos(2\beta)
 \end{aligned} \tag{218}$$

Under plane strain condition, Eq. (217) can be expressed as

$$\begin{aligned}
\sigma_{r'r'} &= \frac{K_I}{\sqrt{2\pi r}} \cos\left(\frac{\theta}{2}\right) \left(2 - \cos^2\left(\frac{\theta}{2}\right) - \frac{R_0}{r}\right) + \frac{K_{II}}{\sqrt{2\pi r}} \sin\left(\frac{\theta}{2}\right) \left(1 - 3\sin^2\left(\frac{\theta}{2}\right) - \frac{R_0}{r}\right) \\
\sigma_{\theta\theta'} &= \frac{1}{\sqrt{2\pi r}} \cos\left(\frac{\theta}{2}\right) \left[K_I \left(\cos^2\left(\frac{\theta}{2}\right) + \frac{R_0}{r} \right) \cos^2(\beta) + 2\nu \sin^2(\beta) \right] - K_{II} \left(\frac{3}{2} \sin(\theta) - \frac{R_0}{r} \tan\left(\frac{\theta}{2}\right) \right) \cos^2(\beta) + 2\nu \tan\left(\frac{\theta}{2}\right) \sin^2(\beta) + K_{III} \sin(2\beta) \\
\sigma_{z'z'} &= \frac{1}{\sqrt{2\pi r}} \cos\left(\frac{\theta}{2}\right) \left[K_I \left(\cos^2\left(\frac{\theta}{2}\right) + \frac{R_0}{r} \right) \sin^2(\beta) + 2\nu \cos^2(\beta) \right] - K_{II} \left(\frac{3}{2} \sin(\theta) - \frac{R_0}{r} \tan\left(\frac{\theta}{2}\right) \right) \sin^2(\beta) + 2\nu \tan\left(\frac{\theta}{2}\right) \cos^2(\beta) - K_{III} \sin(2\beta) \\
\tau_{r'\theta'} &= \frac{1}{\sqrt{2\pi r}} \left[K_I \sin\left(\frac{\theta}{2}\right) \left(\cos^2\left(\frac{\theta}{2}\right) + \frac{R_0}{r} \right) \cos(\beta) + K_{II} \cos\left(\frac{\theta}{2}\right) \left(1 - 3\sin^2\left(\frac{\theta}{2}\right) - \frac{R_0}{r} \right) \cos(\beta) + K_{III} \sin\left(\frac{\theta}{2}\right) \sin(\beta) \right] \\
\tau_{r'z'} &= \frac{1}{\sqrt{2\pi r}} \left[-K_I \sin\left(\frac{\theta}{2}\right) \left(\cos^2\left(\frac{\theta}{2}\right) + \frac{R_0}{r} \right) \sin(\beta) - K_{II} \cos\left(\frac{\theta}{2}\right) \left(1 - 3\sin^2\left(\frac{\theta}{2}\right) - \frac{R_0}{r} \right) \sin(\beta) + K_{III} \sin\left(\frac{\theta}{2}\right) \cos(\beta) \right] \\
\tau_{\theta'z'} &= \frac{1}{\sqrt{2\pi r}} \cos\left(\frac{\theta}{2}\right) \left[K_I \left(\nu - \frac{1}{2} \cos^2\left(\frac{\theta}{2}\right) - \frac{1}{2} \frac{R_0}{r} \right) \sin(2\beta) + K_{II} \left(\frac{3}{4} \sin(\theta) - \frac{1}{2} \frac{R_0}{r} \tan\left(\frac{\theta}{2}\right) - \nu \tan\left(\frac{\theta}{2}\right) \right) \sin(2\beta) + K_{III} \cos(2\beta) \right]
\end{aligned} \tag{219}$$

Under plane stress condition, Eq. (217) can be expressed as

$$\begin{aligned}
\sigma_{r'r'} &= \frac{K_I}{\sqrt{2\pi r}} \cos\left(\frac{\theta}{2}\right) \left(2 - \cos^2\left(\frac{\theta}{2}\right) - \frac{R_0}{r}\right) + \frac{K_{II}}{\sqrt{2\pi r}} \sin\left(\frac{\theta}{2}\right) \left(1 - 3\sin^2\left(\frac{\theta}{2}\right) - \frac{R_0}{r}\right) \\
\sigma_{\theta\theta'} &= \frac{1}{\sqrt{2\pi r}} \cos\left(\frac{\theta}{2}\right) \left[K_I \left(\cos^2\left(\frac{\theta}{2}\right) + \frac{R_0}{r} \right) \cos^2(\beta) - K_{II} \left(\frac{3}{2} \sin(\theta) - \frac{R_0}{r} \tan\left(\frac{\theta}{2}\right) \right) \cos^2(\beta) + K_{III} \sin(2\beta) \right] \\
\sigma_{z'z'} &= \frac{1}{\sqrt{2\pi r}} \cos\left(\frac{\theta}{2}\right) \left[K_I \left(\cos^2\left(\frac{\theta}{2}\right) + \frac{R_0}{r} \right) \sin^2(\beta) - K_{II} \left(\frac{3}{2} \sin(\theta) - \frac{R_0}{r} \tan\left(\frac{\theta}{2}\right) \right) \sin^2(\beta) - K_{III} \sin(2\beta) \right] \\
\tau_{r'\theta'} &= \frac{1}{\sqrt{2\pi r}} \left[K_I \sin\left(\frac{\theta}{2}\right) \left(\cos^2\left(\frac{\theta}{2}\right) + \frac{R_0}{r} \right) \cos(\beta) + K_{II} \cos\left(\frac{\theta}{2}\right) \left(1 - 3\sin^2\left(\frac{\theta}{2}\right) - \frac{R_0}{r} \right) \cos(\beta) + K_{III} \sin\left(\frac{\theta}{2}\right) \sin(\beta) \right] \\
\tau_{r'z'} &= \frac{1}{\sqrt{2\pi r}} \left[-K_I \sin\left(\frac{\theta}{2}\right) \left(\cos^2\left(\frac{\theta}{2}\right) + \frac{R_0}{r} \right) \sin(\beta) - K_{II} \cos\left(\frac{\theta}{2}\right) \left(1 - 3\sin^2\left(\frac{\theta}{2}\right) - \frac{R_0}{r} \right) \sin(\beta) + K_{III} \sin\left(\frac{\theta}{2}\right) \cos(\beta) \right] \\
\tau_{\theta'z'} &= \frac{1}{\sqrt{2\pi r}} \cos\left(\frac{\theta}{2}\right) \left[K_I \left(-\frac{1}{2} \cos^2\left(\frac{\theta}{2}\right) - \frac{1}{2} \frac{R_0}{r} \right) \sin(2\beta) + K_{II} \left(\frac{3}{4} \sin(\theta) - \frac{1}{2} \frac{R_0}{r} \tan\left(\frac{\theta}{2}\right) \right) \sin(2\beta) + K_{III} \cos(2\beta) \right]
\end{aligned} \tag{220}$$

Thus for mixed mode I, II and III under either plane strain or plane stress condition, the fatigue limit criterion becomes

$$\sqrt{\left(\frac{\sigma_{\theta'\theta'}}{f_{-1}}\right)^2 + \left(\frac{\tau_{r'\theta'}}{t_{-1}}\right)^2 + \left(\frac{\tau_{\theta'z'}}{t_{-1}}\right)^2 + A \left(\frac{\sigma_{\theta'\theta'} + \sigma_{z'z'} + \sigma_{r'r'}}{3f_{-1}}\right)^2} = B \tag{221}$$

where $-\pi \leq \theta \leq \pi$ and $-\pi/2 \leq \beta \leq \pi/2$. To determine the parameters A and B , two extreme cases are considered below:

Case 1: Mixed mode I and II fatigue experiment as shown in Figure 18:

In this case there is no contribution of K_{III} . From Eqs. (219) and (220) the stress fields near crack tip can be rewritten as

(a) Under plane strain condition:

$$\begin{aligned}
\sigma_{r,r'} &= \frac{1}{\sqrt{2\pi r}} \left[K_I \cos\left(\frac{\theta}{2}\right) \left(2 - \cos^2\left(\frac{\theta}{2}\right) - \frac{R_0}{r} \right) + K_{II} \sin\left(\frac{\theta}{2}\right) \left(1 - 3 \sin^2\left(\frac{\theta}{2}\right) - \frac{R_0}{r} \right) \right] \\
\sigma_{\theta,\theta'} &= \frac{1}{\sqrt{2\pi r}} \cos\left(\frac{\theta}{2}\right) \left[K_I \left(\cos^2\left(\frac{\theta}{2}\right) + \frac{R_0}{r} \right) \cos^2(\beta) + 2\nu \sin^2(\beta) \right] - K_{II} \left(\frac{3}{2} \sin(\theta) - \frac{R_0}{r} \tan\left(\frac{\theta}{2}\right) \right) \cos^2(\beta) + 2\nu \tan\left(\frac{\theta}{2}\right) \sin^2(\beta) \\
\sigma_{z,z'} &= \frac{1}{\sqrt{2\pi r}} \cos\left(\frac{\theta}{2}\right) \left[K_I \left(\cos^2\left(\frac{\theta}{2}\right) + \frac{R_0}{r} \right) \sin^2(\beta) + 2\nu \cos^2(\beta) \right] - K_{II} \left(\frac{3}{2} \sin(\theta) - \frac{R_0}{r} \tan\left(\frac{\theta}{2}\right) \right) \sin^2(\beta) + 2\nu \tan\left(\frac{\theta}{2}\right) \cos^2(\beta) \\
\tau_{r,\theta'} &= \frac{1}{\sqrt{2\pi r}} \left[K_I \sin\left(\frac{\theta}{2}\right) \left(\cos^2\left(\frac{\theta}{2}\right) + \frac{R_0}{r} \right) \cos(\beta) + K_{II} \cos\left(\frac{\theta}{2}\right) \left(1 - 3 \sin^2\left(\frac{\theta}{2}\right) - \frac{R_0}{r} \right) \cos(\beta) \right] \\
\tau_{r,z'} &= \frac{1}{\sqrt{2\pi r}} \left[-K_I \sin\left(\frac{\theta}{2}\right) \left(\cos^2\left(\frac{\theta}{2}\right) + \frac{R_0}{r} \right) \sin(\beta) - K_{II} \cos\left(\frac{\theta}{2}\right) \left(1 - 3 \sin^2\left(\frac{\theta}{2}\right) - \frac{R_0}{r} \right) \sin(\beta) \right] \\
\tau_{\theta,z'} &= \frac{1}{\sqrt{2\pi r}} \cos\left(\frac{\theta}{2}\right) \left[K_I \left(\nu - \frac{1}{2} \cos^2\left(\frac{\theta}{2}\right) - \frac{1}{2} \frac{R_0}{r} \right) \sin(2\beta) + K_{II} \left(\frac{3}{4} \sin(\theta) - \frac{1}{2} \frac{R_0}{r} \tan\left(\frac{\theta}{2}\right) - \nu \tan\left(\frac{\theta}{2}\right) \right) \sin(2\beta) \right]
\end{aligned} \tag{222}$$

(b) Under plane stress condition:

$$\begin{aligned}
\sigma_{r,r'} &= \frac{1}{\sqrt{2\pi r}} \left[K_I \cos\left(\frac{\theta}{2}\right) \left(2 - \cos^2\left(\frac{\theta}{2}\right) - \frac{R_0}{r} \right) + K_{II} \sin\left(\frac{\theta}{2}\right) \left(1 - 3 \sin^2\left(\frac{\theta}{2}\right) - \frac{R_0}{r} \right) \right] \\
\sigma_{\theta,\theta'} &= \frac{1}{\sqrt{2\pi r}} \cos\left(\frac{\theta}{2}\right) \left[K_I \left(\cos^2\left(\frac{\theta}{2}\right) + \frac{R_0}{r} \right) \cos^2(\beta) - K_{II} \left(\frac{3}{2} \sin(\theta) - \frac{R_0}{r} \tan\left(\frac{\theta}{2}\right) \right) \cos^2(\beta) \right] \\
\sigma_{z,z'} &= \frac{1}{\sqrt{2\pi r}} \cos\left(\frac{\theta}{2}\right) \left[K_I \left(\cos^2\left(\frac{\theta}{2}\right) + \frac{R_0}{r} \right) \sin^2(\beta) - K_{II} \left(\frac{3}{2} \sin(\theta) - \frac{R_0}{r} \tan\left(\frac{\theta}{2}\right) \right) \sin^2(\beta) \right] \\
\tau_{r,\theta'} &= \frac{1}{\sqrt{2\pi r}} \left[K_I \sin\left(\frac{\theta}{2}\right) \left(\cos^2\left(\frac{\theta}{2}\right) + \frac{R_0}{r} \right) \cos(\beta) + K_{II} \cos\left(\frac{\theta}{2}\right) \left(1 - 3 \sin^2\left(\frac{\theta}{2}\right) - \frac{R_0}{r} \right) \cos(\beta) \right] \\
\tau_{r,z'} &= \frac{1}{\sqrt{2\pi r}} \left[-K_I \sin\left(\frac{\theta}{2}\right) \left(\cos^2\left(\frac{\theta}{2}\right) + \frac{R_0}{r} \right) \sin(\beta) - K_{II} \cos\left(\frac{\theta}{2}\right) \left(1 - 3 \sin^2\left(\frac{\theta}{2}\right) - \frac{R_0}{r} \right) \sin(\beta) \right] \\
\tau_{\theta,z'} &= \frac{1}{\sqrt{2\pi r}} \cos\left(\frac{\theta}{2}\right) \left[K_I \left(-\frac{1}{2} \cos^2\left(\frac{\theta}{2}\right) - \frac{1}{2} \frac{R_0}{r} \right) \sin(2\beta) + K_{II} \left(\frac{3}{4} \sin(\theta) - \frac{1}{2} \frac{R_0}{r} \tan\left(\frac{\theta}{2}\right) \right) \sin(2\beta) \right]
\end{aligned} \tag{223}$$

Case 2: Mixed mode I and III fatigue experiment as shown in Figure 23:

In this case there is no contribution of K_{II} . From Eqs. (219) and (220) the stress fields near crack tip can be rewritten as

(a) Under plane strain condition:

$$\begin{aligned}
\sigma_{r'r'} &= \frac{K_I}{\sqrt{2\pi r}} \cos\left(\frac{\theta}{2}\right) \left(2 - \cos^2\left(\frac{\theta}{2}\right) - \frac{R_0}{r}\right) \\
\sigma_{\theta\theta'} &= \frac{1}{\sqrt{2\pi r}} \cos\left(\frac{\theta}{2}\right) \left[K_I \left(\left(\cos^2\left(\frac{\theta}{2}\right) + \frac{R_0}{r} \right) \cos^2(\beta) + 2\nu \sin^2(\beta) \right) + K_{III} \sin(2\beta) \right] \\
\sigma_{z'z'} &= \frac{1}{\sqrt{2\pi r}} \cos\left(\frac{\theta}{2}\right) \left[K_I \left(\left(\cos^2\left(\frac{\theta}{2}\right) + \frac{R_0}{r} \right) \sin^2(\beta) + 2\nu \cos^2(\beta) \right) - K_{III} \sin(2\beta) \right] \\
\tau_{r'\theta'} &= \frac{1}{\sqrt{2\pi r}} \left[K_I \sin\left(\frac{\theta}{2}\right) \left(\cos^2\left(\frac{\theta}{2}\right) + \frac{R_0}{r} \right) \cos(\beta) + K_{III} \sin\left(\frac{\theta}{2}\right) \sin(\beta) \right] \\
\tau_{r'z'} &= \frac{1}{\sqrt{2\pi r}} \left[-K_I \sin\left(\frac{\theta}{2}\right) \left(\cos^2\left(\frac{\theta}{2}\right) + \frac{R_0}{r} \right) \sin(\beta) + K_{III} \sin\left(\frac{\theta}{2}\right) \cos(\beta) \right] \\
\tau_{\theta'z'} &= \frac{1}{\sqrt{2\pi r}} \cos\left(\frac{\theta}{2}\right) \left[K_I \left(\nu - \frac{1}{2} \cos^2\left(\frac{\theta}{2}\right) - \frac{1}{2} \frac{R_0}{r} \right) \sin(2\beta) + K_{III} \cos(2\beta) \right]
\end{aligned} \tag{224}$$

(b) Under plane stress condition:

$$\begin{aligned}
\sigma_{r'r'} &= \frac{K_I}{\sqrt{2\pi r}} \cos\left(\frac{\theta}{2}\right) \left(2 - \cos^2\left(\frac{\theta}{2}\right) - \frac{R_0}{r}\right) \\
\sigma_{\theta\theta'} &= \frac{1}{\sqrt{2\pi r}} \cos\left(\frac{\theta}{2}\right) \left[K_I \left(\cos^2\left(\frac{\theta}{2}\right) + \frac{R_0}{r} \right) \cos^2(\beta) + K_{III} \sin(2\beta) \right] \\
\sigma_{z'z'} &= \frac{1}{\sqrt{2\pi r}} \cos\left(\frac{\theta}{2}\right) \left[K_I \left(\cos^2\left(\frac{\theta}{2}\right) + \frac{R_0}{r} \right) \sin^2(\beta) - K_{III} \sin(2\beta) \right] \\
\tau_{r'\theta'} &= \frac{1}{\sqrt{2\pi r}} \left[K_I \sin\left(\frac{\theta}{2}\right) \left(\cos^2\left(\frac{\theta}{2}\right) + \frac{R_0}{r} \right) \cos(\beta) + K_{III} \sin\left(\frac{\theta}{2}\right) \sin(\beta) \right] \\
\tau_{r'z'} &= \frac{1}{\sqrt{2\pi r}} \left[-K_I \sin\left(\frac{\theta}{2}\right) \left(\cos^2\left(\frac{\theta}{2}\right) + \frac{R_0}{r} \right) \sin(\beta) + K_{III} \sin\left(\frac{\theta}{2}\right) \cos(\beta) \right] \\
\tau_{\theta'z'} &= \frac{1}{\sqrt{2\pi r}} \cos\left(\frac{\theta}{2}\right) \left[K_I \left(-\frac{1}{2} \cos^2\left(\frac{\theta}{2}\right) - \frac{1}{2} \frac{R_0}{r} \right) \sin(2\beta) + K_{III} \cos(2\beta) \right]
\end{aligned} \tag{225}$$

According to the maximum shear stress criterion (MSS), the maximum shear stress at r_c occurs at the angle of θ , which satisfies

$$\frac{\partial \tau_{r'\theta'}}{\partial \beta} = 0 \quad \frac{\partial \tau_{r'\theta'}}{\partial \theta} = 0 \quad \frac{\partial^2 \tau_{r'\theta'}}{\partial \beta^2} < 0 \quad \frac{\partial^2 \tau_{r'\theta'}}{\partial \beta^2} \frac{\partial^2 \tau_{r'\theta'}}{\partial \theta^2} - \left(\frac{\partial^2 \tau_{r'\theta'}}{\partial \beta \partial \theta} \right)^2 > 0 \tag{226}$$

for mixed mode I and II, and

$$\frac{\partial \tau_{\theta'z'}}{\partial \beta} = 0 \quad \frac{\partial \tau_{\theta'z'}}{\partial \theta} = 0 \quad \frac{\partial^2 \tau_{\theta'z'}}{\partial \beta^2} < 0 \quad \frac{\partial^2 \tau_{\theta'z'}}{\partial \beta^2} \frac{\partial^2 \tau_{\theta'z'}}{\partial \theta^2} - \left(\frac{\partial^2 \tau_{\theta'z'}}{\partial \beta \partial \theta} \right)^2 > 0 \quad (227)$$

for mixed mode I and III.

In case 1 for both plane strain and plane stress, the relationship between θ and the ratio of K_I to K_{II} is shown in Figure 27.

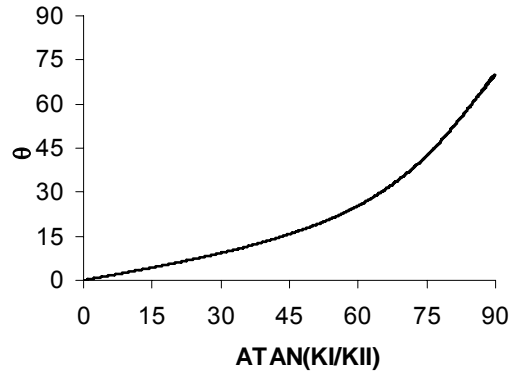


Figure 27. θ vs. K_I / K_{II}

Then Eq. (221) for plane strain condition can be rewritten as:

$$\sqrt{\left(\frac{\cos\left(\frac{\theta}{2}\right) \left[K_I \left(\cos^2\left(\frac{\theta}{2}\right) + \frac{R_0}{r} \right) - K_{II} \left(\frac{3}{2} \sin(\theta) - \frac{R_0}{r} \tan\left(\frac{\theta}{2}\right) \right) \right]}{K_{I,th}} \right)^2 + \left(\frac{K_I \sin\left(\frac{\theta}{2}\right) \left(\cos^2\left(\frac{\theta}{2}\right) + \frac{R_0}{r} \right) + K_{II} \cos\left(\frac{\theta}{2}\right) \left(1 - 3 \sin^2\left(\frac{\theta}{2}\right) - \frac{R_0}{r} \right)}{\xi K_{II,th}} \right)^2 + A \left(\frac{2(1+\nu) \left[K_I - K_{II} \tan\left(\frac{\theta}{2}\right) \right]}{3K_{I,th}} \right)^2} = B \quad (228)$$

For plane stress condition Eq. (221) can be expressed as

$$\sqrt{\left(\frac{\cos\left(\frac{\theta}{2}\right) \left[K_I \left(\cos^2\left(\frac{\theta}{2}\right) + \frac{R_0}{r} \right) - K_{II} \left(\frac{3}{2} \sin(\theta) - \frac{R_0}{r} \tan\left(\frac{\theta}{2}\right) \right) \right]}{K_{I,th}} \right)^2 + \left(\frac{K_I \sin\left(\frac{\theta}{2}\right) \left(\cos^2\left(\frac{\theta}{2}\right) + \frac{R_0}{r} \right) + K_{II} \cos\left(\frac{\theta}{2}\right) \left(1 - 3 \sin^2\left(\frac{\theta}{2}\right) - \frac{R_0}{r} \right)}{\xi K_{II,th}} \right)^2 + A \left(\frac{2 \left[K_I - K_{II} \tan\left(\frac{\theta}{2}\right) \right]}{3K_{I,th}} \right)^2} = B \quad (229)$$

In case 2 for plane strain condition,

$$\tau_{\theta'z'} = \frac{1}{\sqrt{2\pi r}} \cos\left(\frac{\theta}{2}\right) \left[K_I \left(\nu - \frac{1}{2} \cos^2\left(\frac{\theta}{2}\right) - \frac{1}{2} \frac{R_0}{r} \right) \sin(2\beta) + K_{III} \cos(2\beta) \right] \quad (230)$$

where θ and β can be solved from the MSS criterion using Eq. (227). Thus in mixed mode I and III for plane strain

$$\begin{cases} \theta = 0 \\ \tan(2\beta) = \frac{K_I}{K_{III}} \left(\nu - \frac{1}{2} - \frac{1}{2} \frac{R_0}{r} \right) \end{cases} \quad (231)$$

In case 2 for plane stress condition

$$\tau_{\theta'z'} = \frac{1}{\sqrt{2\pi r}} \cos\left(\frac{\theta}{2}\right) \left[K_I \left(-\frac{1}{2} \cos^2\left(\frac{\theta}{2}\right) - \frac{1}{2} \frac{R_0}{r} \right) \sin(2\beta) + K_{III} \cos(2\beta) \right] \quad (232)$$

where θ and β can be solved from MSS criteria using Eq. (227). Thus in mixed mode I and III for plane stress

$$\begin{cases} \theta = 0 \\ \tan(2\beta) = -\frac{1}{2} \frac{K_I}{K_{III}} \left(1 + \frac{R_0}{r} \right) \end{cases} \quad (233)$$

Then in case 2 under plane strain condition Eq. (221) can be rewritten as:

$$\sqrt{\left(\frac{K_I \left(\left(1 + \frac{R_0}{r} \right) \cos^2(\beta) + 2\nu \sin^2(\beta) \right) + K_{III} \sin(2\beta)}{K_{I,th}} \right)^2 + \left(\frac{K_I \left(\nu - \frac{1}{2} - \frac{1}{2} \frac{R_0}{r} \right) \sin(2\beta) + K_{III} \cos(2\beta)}{\xi K_{I,th}} \right)^2} + A \left(\frac{2(1+\nu)K_I}{3K_{I,th}} \right)^2 = B \quad (234)$$

For plane stress condition Eq. (221) can be expressed as

$$\sqrt{\left(\frac{K_I \left(1 + \frac{R_0}{r} \right) \cos^2(\beta) + K_{III} \sin(2\beta)}{K_{I,th}} \right)^2 + \left(\frac{-\frac{1}{2} K_I \left(1 + \frac{R_0}{r} \right) \sin(2\beta) + K_{III} \cos(2\beta)}{\xi K_{I,th}} \right)^2} + \frac{4}{9} A \left(\frac{K_I}{K_{I,th}} \right)^2 = B \quad (235)$$

Eqs. (234) and (235) can be simplified as follows:

(a) for plane strain condition

$$\left| \frac{K_I}{K_{I,th}} \right| \sqrt{\left(\nu + \frac{1}{2} + \frac{1}{2} \frac{R_0}{r} \right)^2 + \frac{1 + (K_I / K_{III})^2 \left(\nu - \frac{1}{2} - \frac{1}{2} \frac{R_0}{r} \right)^2}{\xi^2 (K_I / K_{III})^2} + \frac{4}{9} A (1 + \nu)^2} = B \quad (236)$$

(b) for plane stress condition

$$\left| \frac{K_I}{K_{I,th}} \right| \sqrt{\frac{1}{4} \left(1 + \frac{R_0}{r} \right)^2 + \frac{1 + (K_I / K_{III})^2 \left(1 + \frac{R_0}{r} \right)^2 / 4}{\xi^2 (K_I / K_{III})^2} + \frac{4}{9} A} = B \quad (237)$$

Solving Eqs. (228) and (236) for A and B in plane strain condition

$$A = \frac{\left[\cos^2 \left(\frac{\theta}{2} \right) \left(\cos^2 \left(\frac{\theta}{2} \right) + \frac{R_0}{r} - \frac{K_{II}}{K_I} \left(\frac{3}{2} \sin(\theta) - \frac{R_0}{r} \tan \left(\frac{\theta}{2} \right) \right) \right)^2 + \left[\sin \left(\frac{\theta}{2} \right) \left(\cos^2 \left(\frac{\theta}{2} \right) + \frac{R_0}{r} \right) + \frac{K_{II}}{K_I} \left(1 - 3 \sin^2 \left(\frac{\theta}{2} \right) - \frac{R_0}{r} \right) \right]^2 / \xi^2 - \left(\nu + \frac{1}{2} + \frac{1}{2} \frac{R_0}{r} \right)^2 - \frac{1 + (K_I / K_{III})^2 \left(\nu - \frac{1}{2} - \frac{1}{2} \frac{R_0}{r} \right)^2}{\xi^2 (K_I / K_{III})^2} \right]}{\frac{4}{9} (1 + \nu)^2 - \frac{4}{9} (1 + \nu)^2 \left[1 - \frac{K_{II}}{K_I} \tan \left(\frac{\theta}{2} \right) \right]^2} \quad (238)$$

$$B = \left| \frac{K_I}{K_{I,th}} \right| \sqrt{\left(\nu + \frac{1}{2} + \frac{1}{2} \frac{R_0}{r} \right)^2 + \frac{1 + (K_I / K_{III})^2 \left(\nu - \frac{1}{2} - \frac{1}{2} \frac{R_0}{r} \right)^2}{\xi^2 (K_I / K_{III})^2} + \frac{4}{9} A (1 + \nu)^2}$$

Solving Eqs. (229) and (237) for A and B in plane stress condition

$$A = \frac{\left[\cos^2 \left(\frac{\theta}{2} \right) \left(\cos^2 \left(\frac{\theta}{2} \right) + \frac{R_0}{r} - \frac{K_{II}}{K_I} \left(\frac{3}{2} \sin(\theta) - \frac{R_0}{r} \tan \left(\frac{\theta}{2} \right) \right) \right)^2 + \left[\sin \left(\frac{\theta}{2} \right) \left(\cos^2 \left(\frac{\theta}{2} \right) + \frac{R_0}{r} \right) + \frac{K_{II}}{K_I} \left(1 - 3 \sin^2 \left(\frac{\theta}{2} \right) - \frac{R_0}{r} \right) \right]^2 / \xi^2 - \frac{1}{4} \left(1 + \frac{R_0}{r} \right)^2 - \frac{1 + (K_I / K_{III})^2 \left(1 + \frac{R_0}{r} \right)^2 / 4}{\xi^2 (K_I / K_{III})^2} \right]}{\frac{4}{9} - \frac{4}{9} \left[1 - \frac{K_{II}}{K_I} \tan \left(\frac{\theta}{2} \right) \right]^2} \quad (239)$$

$$B = \left| \frac{K_I}{K_{I,th}} \right| \sqrt{\frac{1}{4} \left(1 + \frac{R_0}{r} \right)^2 + \frac{1 + (K_I / K_{III})^2 \left(1 + \frac{R_0}{r} \right)^2 / 4}{\xi^2 (K_I / K_{III})^2} + \frac{4}{9} A}$$

where A and B should be non negative real numbers.

The characteristic plane orientation calculated by the MSS criterion is applicable for both brittle and ductile materials. In these two extreme cases (case 1 and case 2) the characteristic plane orientations coincide with the crack orientations θ and β predicted by the MSS criterion. If the length of the structure is much greater than the other two dimensions, Eq. (238) for plane strain can be used. If one of the dimensions of the structure is much smaller than the other two, such as thin plate, Eq. (239) for plane stress can be applied.

3.5 Conclusion

Three formulas for mixed-mode (I+II / I+III / I+II+III) threshold stress intensity factor and crack growth rate prediction of notched specimens are derived in this chapter. The proposed fatigue crack growth model is developed using the local stress components (near crack tip) and the characteristic plane concept. Two major advantages of the proposed model are that (1) it can automatically adapt for different failure mechanisms and (2) local geometric effects and residual stress effects near crack tip can be included in this local stress based model much easier than the remote stress approach, such as cracks emanating from notches or holes by considering notch radius in the expressions of stress fields near notch tips.

The models proposed in Chapters 2 and 3 are only applicable to the fatigue crack prediction in the near threshold region and Paris's region. However the fatigue life of many materials is primarily crack growth from small preexisting defects, such as inclusion particles, voids (pores) or slip-band formation, or may be an inadvertent result of careless transportation or handling. When failure originates from microdefects, the majority of the fatigue life will be spent as cracks smaller than the NDI detection limit, which is around 0.5-1.0mm. The mixed mode criteria for small crack growth prediction are investigated in Chapter 4.

CHAPTER IV

MIXED-MODE SMALL FATIGUE CRACK GROWTH

4.1 Introduction

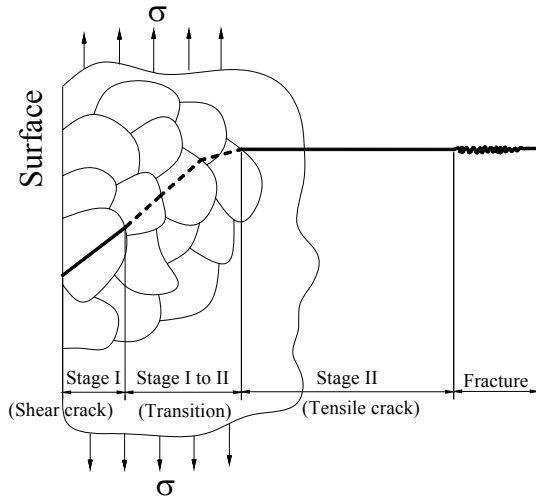
In this task, a new model for mixed-mode small fatigue crack growth rate prediction is proposed. The method is also developed using local stresses near the crack tip rather than remote stresses. The local stress field is transformed onto the slip plane of crystal near small crack tip. The contribution of shear stress on the slip plane, which has been considered as the only driving force of small crack growth in earlier studies, as well as normal stress and hydrostatic stress are taken into account for the life prediction of structures with small cracks. Under such small scale, isotropic material property assumption is no longer valid, and the effects of various microstructural factors on stage I fatigue crack growth are included in the proposed model.

Some background on the anomalous propagation behavior of small cracks is given in section 4.2. Then a brief review of current small fatigue crack propagation models is shown in section 4.3. In the section 4.4, the derivation of the model is demonstrated using a smooth specimen with central crack under remote tension. The multiaxial fatigue limit criterion developed earlier by Liu and Mahadevan [9] is extended to develop a microscopic threshold stress intensity factor criterion using the Kitagawa-Takahashi diagram. Following this, an equivalent stress intensity factor is proposed for the crack growth rate prediction.

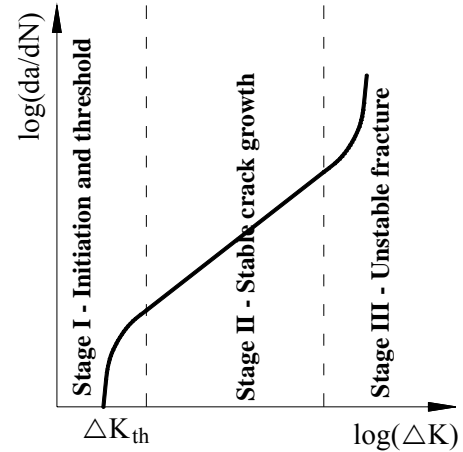
4.2 Background

In 1961, Forsyth [88] proposed a two-stage process theory (Figure 28 (a)) for fatigue crack growth from observations in push-pull tests. The initial Stage I growth (shear type) corresponds to the slip band formation and largely depends on microstructure details. Then it is followed by Stage II (tensile type) cracking, in which the general plane of the crack is normal to the direction of the maximum tensile stress and crack growth rates do not depend on microstructure. In sharply notched specimens, stage I growth may be completely absent, while in smooth specimens it may account for up to 90% of the total life [89]. Also in 1961, Paris [90] introduced stress intensity factors to quantify fatigue crack propagation rate in Stage II based on linear elastic fracture mechanics (LEFM). Later the crack growth rate for mode I cracks in metals is found to have a sigmoidal shape as shown in Figure 28 (b). In stage I, the crack growth rate goes asymptotically to zero as ΔK approaches a threshold value ΔK_{th} and there is no crack growth below this value. In this stage the crack path deviates from the pure stage II cracking. It is more sensitive to the microstructure of materials and the stress history on the structures. In stage II, crack growth follows linear growth pattern in log-log coordinate. In stage III crack growth exhibits a rapidly increasing growth rate towards “infinity”.

Actually there are two commonly used types of fatigue threshold, fatigue crack propagation threshold ΔK_{th} and fatigue limit $\Delta\sigma_{FL}$. Millers [91] and Kitagawa [11] tried to relate $\Delta\sigma_{FL}$ to ΔK_{th} as shown in Figure 29 and Figure 30.



(a) Two stages of crack growth [91]



(b) Three stages of crack growth [92]

Figure 28. Crack growth classification

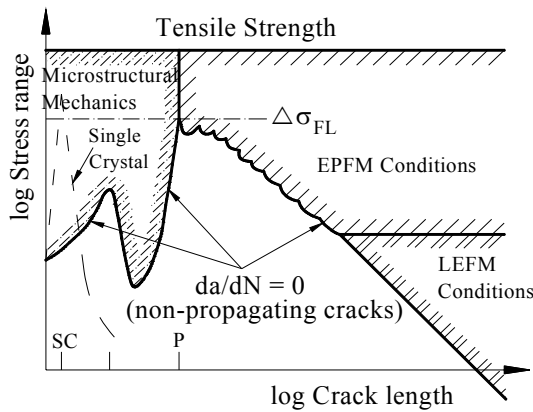


Figure 29. Threshold behavior by Miller [91]

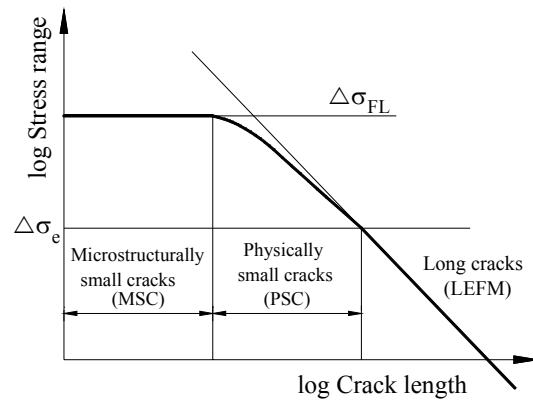


Figure 30. Kitagawa-Takahashi diagram [11]

In 1975, Pearson [93] observed that small cracks (0.006-0.5 mm) grow much faster than would be predicted from the large crack data on the basis of linear elastic fracture mechanics. Since then anomalous small crack growth behavior (Figure 31), which is defined as fatigue cracks grow at stress intensity factors significantly below the large crack fatigue threshold and grow faster than large cracks at the same ΔK level

above threshold, has been observed in steel [94-99], titanium alloys [100-102], aluminum alloys [5, 103-105] and nickel based alloys [106-108], etc. However, the mechanism of small crack growth and the basic causes of small crack anomalies are not fully understood.

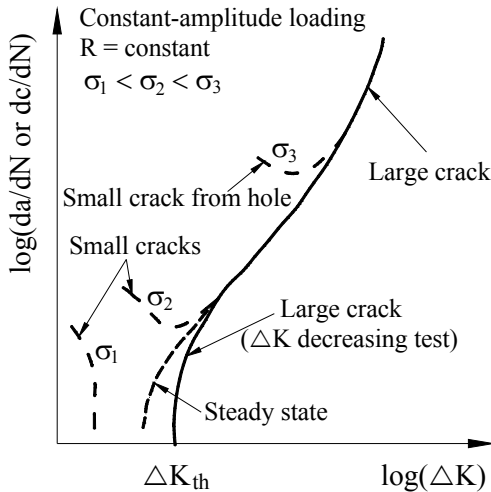


Figure 31. Small crack behavior [109]

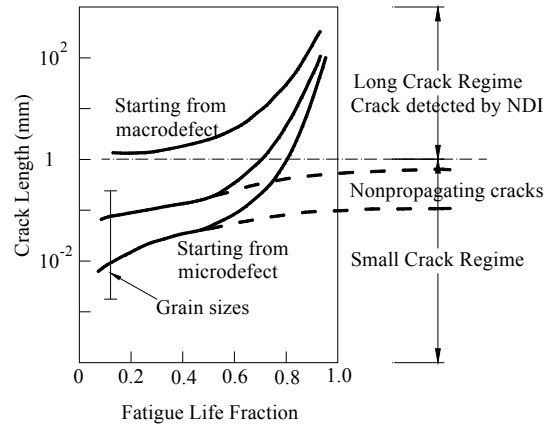


Figure 32. Fatigue life fraction [109]

Now it is generally realized that the fatigue life of many materials is primarily crack growth from small preexisting defects, which may be formed as a result of material forming and fabrication techniques and related to microstructural features, such as inclusion particles, voids (pores) or slip-band formation, or may be an inadvertent result of careless transportation or handling. Figure 32 shows that when failure originates from microdefects, the majority of the fatigue life will be spent as cracks smaller than the NDI detection limit, which is around 0.5-1.0mm.

Generally fatigue crack propagation is influenced by a mixture of factors: (a) material (e.g., ductile and brittle); (b) mechanics (e.g., statics, dynamics, fatigue, creep); and (c) loading modes (e.g., tension, torsion, biaxial/multi-axial). Additionally mixed-

mode crack propagation can be affected by many other factors such as (d) geometry (thin plates, thick shells, and the size, shape and orientation of the defect); (e) environmental effects (temperature, gaseous and liquid surroundings); (f) material state (crystallographic structure, heat treatment and route of manufacture) and (g) stress conditions (out-of – phase and random loading effects) [91].

Previous studies have proposed three main explanations for the “anomalous” propagation behavior: (a) plasticity effects (b) metallurgical effects and (c) crack closure. Details can be found in the review papers [110, 111]. All of these features challenge the use of LEFM and ΔK concepts to explain small fatigue crack growth rates [112]. A brief review of the existing criteria is given below.

4.3 Existing criteria

A number of small fatigue crack propagation models have been proposed in the literature and a brief description is given below.

(1) Models based on crack tip strain:

Using the elastic plastic fracture mechanics (EPFM) approach, Tomkins [113] equated da/dN to crack tip decohesion and then to the bulk plastic strain field as shown in Eq.(240), where B and m are material constants.

$$da/dN = B(\Delta\varepsilon_p \sqrt{\pi a})^m \quad (240)$$

Chan and Lankford [114] modified the LEFM equation to consider the variation on the grain orientation and effects of the grain boundaries. The model was based on the assumption that near the threshold stress intensity for a long crack, the crack-tip opening displacement (CTOD) is larger for small/short crack than for a nominally equivalent long

through-crack, i.e the plastic strain range associated with a small crack is higher than that of a long crack. Considering the influence of the crystallographic orientations of the neighboring grains and the distance of the crack-tip from the nearest grain boundary, the plastic strain range at the crack tip was defined as:

$$\Delta\varepsilon_p = C\Delta K^{n_1} \left[1 - K(\Phi) \left(\frac{D-2X}{D} \right)^m \right] \quad (241)$$

The crystallographic function $K(\Phi)$ in terms of resolved shear stress in the grain with small crack (grain A) and its neighboring grain (B) was defined as

$$K(\Phi) = 1 - \frac{\tau_B}{\tau_A} \quad (242)$$

In this approach, the local plastic strain range at the crack-tip was used as a measure of fatigue damage. Crack advance by the failure of a crack-tip element of size $\Delta X'$ occurs when the accumulated local plastic strain exceeds a critical value ε_p^* . The number of cycles ΔN required for failure of crack-tip element was given by

$$\Delta N = \frac{\varepsilon_p^*}{\Delta\varepsilon_p} \quad (243)$$

And the crack growth rate was defined as

$$\frac{da}{dN} = C_1 \Delta K^{n_1} \left[1 - \left(1 - \frac{\tau_A}{\tau_B} \right) \left(\frac{D-2X}{D} \right)^m \right] \quad (244)$$

where

$$C_1 = \frac{\Delta X' C}{\varepsilon^*} \quad (245)$$

From a physics and mechanics point of view, Chan and Lankford's model is a gross approximation to reality. The model predicts little or no deceleration in growth rate in the case of similar orientation of grains.

(2) Models based on modification of LEFM:

Donahue et al. [38] proposed a formula for both near crack threshold and Paris type crack growth as

$$\frac{da}{dN} = C(\Delta K - \Delta K_{th})^m \quad (246)$$

Another well known expression proposed for the entire regime of crack growth is the NASGRO expression [115] (also known as the Forman-Newman-de Koning equation), which is commonly used in aircraft applications.

$$\frac{da}{dN} = C \left(\left(\frac{1-f}{1-R} \right) \Delta K \right)^n \frac{\left(1 - \frac{\Delta K_{th}}{\Delta K} \right)^p}{\left(1 - \frac{K_{max}}{K_c} \right)^q} \quad (247)$$

This NASGRO equation [115] is used by AFGROW [116], NASGRO 3 [115] and NASGRO 4 [115] to calculate the crack growth rate. In Eq. (247), $C \left(\left(\frac{1-f}{1-R} \right) \Delta K \right)^n$ is fitted to the data in the Paris regime. The terms $\left(1 - \frac{\Delta K_{th}}{\Delta K} \right)^p$ and $\left(1 - \frac{K_{max}}{K_c} \right)^q$ are used to describe the crack growth behavior near threshold regime and rapid growth regime, respectively. K_{max} is the maximum stress intensity factor in a load cycle. K_c is the crack resistance against fracture. p and q are empirical constants from curve fitting. Since only

limited crack growth data is available for the threshold region, f is approximated using the Newman closure function [115] as

$$f = \frac{K_{op}}{K_{max}} = \begin{cases} \max(R, A_0 + A_1R + A_2R^2 + A_3R^3) & R \geq 0 \\ A_0 + A_1R & -2 \leq R \leq 0 \end{cases} \quad (248)$$

The coefficients are given by

$$\begin{aligned} A_0 &= (0.825 - 0.34\alpha + 0.05\alpha^2) \left[\cos\left(\frac{\pi}{2} \frac{S_{max}}{\sigma_0}\right) \right]^{\frac{1}{\alpha}} \\ A_1 &= (0.415 - 0.071\alpha) \frac{S_{max}}{\sigma_0} \\ A_2 &= 1 - A_0 - A_1 - A_3 \\ A_3 &= 2A_0 + A_1 - 1 \end{aligned} \quad (249)$$

where α is the plane stress/strain constraint factor and S_{max} / σ_0 is the ratio of maximum stress to the flow stress.

The threshold stress intensity factor range is calculated by the following empirical equations

$$\begin{aligned} \Delta K_{th} &= \Delta K_0 \left(\frac{a}{a+a_0} \right)^{\frac{1}{2}} / \left(\frac{1-f}{(1-A_0)(1-R)} \right)^{(1+C_{th}R)} && \text{in AFGROW / NASGRO 3} \\ \Delta K_{th} &= \begin{cases} \Delta K_0 \left(\frac{a}{a+a_0} \right)^{\frac{1}{2}} \left(\frac{1-R}{1-f} \right)^{(1+C_{th}^p R)} / (1-A_0)^{(1-R)C_{th}^p} & R \geq 0 \\ \Delta K_0 \left(\frac{a}{a+a_0} \right)^{\frac{1}{2}} \left(\frac{1-R}{1-f} \right)^{(1+C_{th}^m R)} / (1-A_0)^{(1-R)C_{th}^m} & R < 0 \end{cases} && \text{in NASGRO 4} \end{aligned} \quad (250)$$

where ΔK_0 is the threshold stress intensity factor range at $R=0$, C_{th} is an empirical constant, C_{th}^p and C_{th}^m are constants to control various R ratio ($C_{th}^m = 0.1$ for negative R ratio), a is the crack length, a_0 is an intrinsic crack length ($a_0 = 0.0381$).

Several researchers have proposed different correction factors to consider the stress ratio effect, such as Walker [37], and Erdogan and Ratwani [39].

McEvily *et al.* [117] proposed a short crack analysis considering large-scale plasticity effects, crack closure and the fatigue crack growth threshold. This model is based on modification of elastic analysis in the presence of large-scale plasticity, and is expanded as

$$\frac{da}{dN} = A \left[\sqrt{\frac{\pi\rho_e}{4}} + Y \sqrt{\frac{\pi}{2}} a \left(\sec \frac{\pi\sigma_{\max}}{2\sigma_y} + 1 \right) \Delta\sigma - (1 - e^{-kl}) K_{op\max} - \Delta K_{effth} \right]^2 \quad (251)$$

where A is a material and environment sensitive constant, ρ_e is the radius of the stress raise at crack tip, Y is a geometrical factor, a is the actual crack length, σ_{\max} is the maximum stress applied, σ_y is the yield strength, $\Delta\sigma$ is the applied stress range, k is a material constant which reflects the rate of crack closure development with crack advance, $K_{op\max}$ is the maximum stress intensity factor at the opening level for a macroscopic crack, ΔK_{effth} is the effective range of the stress intensity factor at the threshold level.

(3) Model based on strength of the slip band:

de los Rios *et al.* [118] proposed that crack growth rate is proportional to the strength of the slip band, assuming that crack will initiate from slip band for a smooth specimen:

$$\frac{da}{dN} = f_1 \frac{\tau(L-a)}{\mu} \quad (252)$$

where

$$\tau = \frac{\mu n_d b}{L} = \alpha \tau_{app} - \tau_0 \quad (253)$$

α is orientation factor, τ_{app} is the applied shear stress, n_d is the number of dislocation, b is the Burger vector and τ_0 is the internal friction stress, μ is the shear modulus, a is crack length and f_1 is the fraction of dislocation on the slip band.

(4) Model based on energy release rate:

de los Rios *et al.* [118] developed another model based on load and bulk energy considerations, assuming that the local energy, i.e. the energy at the slip band, should be equal to the crack extension energy for crack propagation. A second consideration of the model was the nature and strength of the barriers that should be overcome to propagate the crack into the next grain. The micro processes of crack growth need to be related to the mechanics of crack extension. The model is of the form

$$\frac{da}{dN} = f_1 (2\pi a D)^{0.5} \left[1 - \left(1 - \frac{\tau_B}{\tau_A} \right) \left(\frac{D-X}{D} \right)^m \right] \frac{\tau}{\mu} \quad (254)$$

where f_1 and m are material constants, a is crack length, D is the distance from barrier to barrier, τ_A and τ_B are the shear stress in the small grain A and its neighboring grain B , τ is the shear stress applied on slip band and μ is the shear modulus.

(5) Model using macro-micro approach:

As we know the nucleation of fatigue cracks is a microscopic phenomenon which happens at the scale of one or a few grains. At this scale the material is neither homogeneous nor isotropic, and the local stresses and strains (σ and ε) can be very different from corresponding macroscopic quantities (Σ and E). Dang Van [119]

proposed a multiaxial fatigue criterion using a macro to micro approach. The two scales are distinguished below:

- (a) The macroscopic scale is characterized by an elementary representative volume $V(M)$ surrounding the point M where the fatigue analysis is done and representing, for instance, an element of a finite element mesh or corresponding to the dimension of a strain gauge. Mechanical macroscopic variables $\Sigma(M, t)$ and $E(M, t)$ are assumed to be homogeneous in $V(M)$ at any time t .
- (b) The microscopic scale is the order of one or a few grain sizes corresponding to a subdivision of $V(M)$. The microscopic quantities σ and ε are not homogeneous and differ from Σ and E . Even if the mean value of σ equals Σ , the local stress σ can fluctuate.

The relationship of σ and Σ can be expressed as

$$\sigma_{ij}(m, t) = A_{ijhk}(M, m)\Sigma_{hk}(M, t) + \rho_{ij}(m, t) \quad (255)$$

where $A_{ijhk}(M, m)$ is the elastic localization tensor and $\rho_{ij}(m, t)$ is the local residual stress field. In general case it is difficult to get the mathematical answer for this localization. An approximate solution is given by Dang Van [119] to evaluate the local stress in the stabilized state, based on three hypotheses:

- (a) Only one slip system is activated. This system is defined by n , which is normal to the slip plane, and m , which is the slip direction.
- (b) Microscopic strains show isotropic hardening.
- (c) Micro element undergo the macroscopic deformation E , where $\varepsilon_{ij}^e + p_{ij} = E_{ij}$, since macroscopic plastic strain P_{ij} is negligible at the fatigue limit.

Thus Eq. (255) can be simplified as

$$\sigma_{ij}(t) = \Sigma_{ij}(t) - 2\alpha_{ij}T_0 \quad (256)$$

where $\alpha_{ij} = (n_i m_j + m_i n_j)/2$ and T_0 is the mean value of shear stresses in the plane where maximum shear amplitude occurs (this plane is defined by n). The failure criterion can be expressed as

$$\tau + ap - b = 0 \quad (257)$$

where τ is the local shear stress, p is the hydrostatic stress, and a and b are fitting parameters.

Among the analytical models discussed above, Chan and Lankford's model and de los Rios et al.'s model focuses on metallurgical effects, McEvily et al.'s model includes both plasticity effects and crack closure effects, while NASGRO and AFGROW include plasticity effects and crack closure effects together with stress ratio effects. Dang Van's model includes microstructural effects.

The characteristics of microstructurally small cracks are as follows [120]: (i) slip deformation near the crack tip is on the slip plane ; (ii) the crack-tip slip deformation is blocked by grain or phase boundaries ; (iii) cracks may follow slip planes and are often accompanied with crack deflection ; (iv) mixed-mode stress field near the crack tip; (v) large scale yielding or elastic-plastic condition near the crack tip; and (vi) the amount of crack closure is small and varies with crack length.

The effects of various microstructural factors on small-crack growth depend on the material and the applied stress levels. Experimental studies need to be carried out to determine the predominant factors in each specific situation. Meanwhile theoretical

modeling of microstructurally small crack growth is needed for quantitative prediction. The following sections pursue this objective.

4.4 Proposed criterion

Similar to the proposed mixed-mode near threshold fatigue crack growth criteria for smooth and notched specimens, the multiaxial fatigue limit criterion proposed earlier by Liu and Mahadevan [9] is extended to develop a mixed-mode near threshold fatigue crack growth criterion for small crack using the relationship between fatigue limit and microscopic threshold stress intensity factor.

4.4.1 Fatigue limit and microscopic threshold stress intensity factor

A link between the fatigue limit and the threshold stress intensity factor for long crack was proposed by Kitagawa and Takahashi [11] and can be expressed as the well-known El Haddad model [63].

For microstructurally small crack, crack-tip plasticity is simplified by a model that considers rigid plastic yield strips expanding coplanar to the crack according to dislocation-based formulation of crack growth. The crack and yield strips are represented by an array of infinitesimal dislocations. Under monotonic or cyclic loading, the slip band will emanate from the crack-tip and expand against the frictional stress.

Consider a crack of length $2a$ in an infinite plane under a remote tensile stress σ_0 , as shown in Figure 33, the size of the slip band is $w_0 = b_0 - a$. The microscopic stress intensity factor K_0^m at the tip of the slip band is expressed as [121]:

$$K_0^m = \sigma_0 \sqrt{\pi b_0} - 2\sigma_{fr} \sqrt{\frac{b_0}{\pi}} \arccos\left(\frac{a}{b_0}\right) \quad (258)$$

where b_0 is the effective crack length and σ_{fr} is the frictional stress regarded as a material constant that is independent of the slip-band configuration. Considering Hall-Petch law [122, 123] as shown in Eq. (259)

$$\sigma_y = \sigma_{fr} + \frac{k_y}{\sqrt{d}} \quad (259)$$

where σ_y is the yield stress, k_y is a material constant and d is the grain diameter. Then

σ_{fr} can be calculated by

$$\sigma_{fr} = \sigma_y - \frac{k_y}{\sqrt{d}} \quad (260)$$

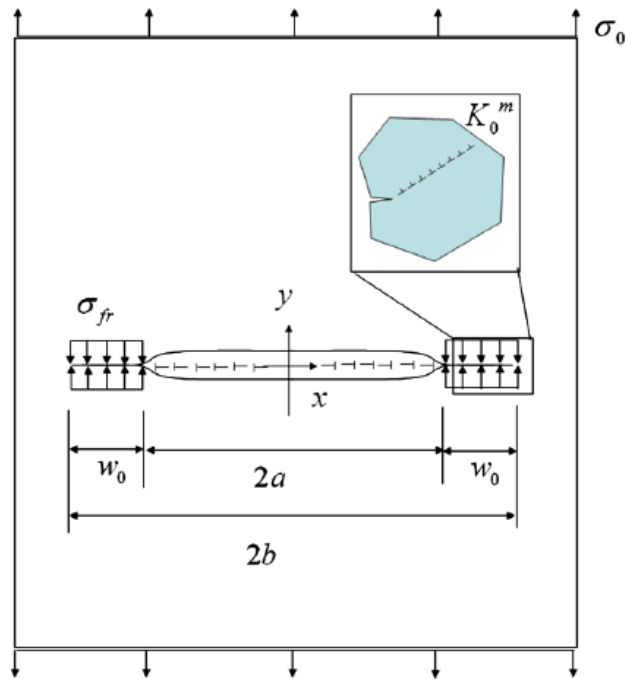


Figure 33. Coplanar slip band emanating from the tip of isolated crack [121]

For equilibrium slip band (ESB), dislocations slide only against frictional stress, the crack opening stress σ_0^{ESB} is obtained by letting K_0^m equals to zero in Eq. (258).

$$\sigma_0^{ESB} = \frac{2}{\pi} \sigma_{fr} \arccos\left(\frac{a^{ESB}}{b_0}\right) \quad (261)$$

The intrinsic threshold stress intensity factor $\Delta K_{th}^{i ntr}$, which is the driving force for stable fatigue crack growth in a single grain, can be expressed as

$$\Delta K_{th}^{i ntr} = \sigma_0^{ESB} \sqrt{\pi a^{ESB}} \quad (262)$$

When slip bands reach grain boundary, they may get blocked by the grain boundary. The crack opening stress σ_0^{BSB} for a blocked slip band (BSB) can be expressed as

$$\sigma_0^{BSB} = \frac{K_0^m}{\sqrt{\pi b_0^{BSB}}} + \left(\frac{2}{\pi} \sigma_{fr}\right) \arccos\left(\frac{a^{BSB}}{b_0^{BSB}}\right) \quad (263)$$

The corresponding intrinsic threshold stress intensity factor $\Delta K_{th}^{i ntr}$ is expressed as

$$\Delta K_{th}^{i ntr} = \sigma_0^{BSB} \sqrt{\pi a^{BSB}} = \left[\frac{K_0^m}{\sqrt{\pi b_0^{BSB}}} + \left(\frac{2}{\pi} \sigma_{fr}\right) \arccos\left(\frac{a^{BSB}}{b_0^{BSB}}\right) \right] \sqrt{\pi a^{BSB}} \quad (264)$$

Substituting $a = 0$ into Eq. (263), tensile fatigue limit f_{-1} can be obtained as

$$f_{-1} = \frac{K_{I,0}^m}{\sqrt{\pi w_0}} + \sigma_{fr} = \frac{K_{I,th}^m}{\sqrt{\pi w_0}} \quad (265)$$

Using the same approach, shear fatigue limit can be expressed as

$$t_{-1} = \frac{K_{II,0}^m}{\sqrt{\pi w_0}} + \tau_{fr} = \frac{K_{II,th}^m}{\sqrt{\pi w_0}} \quad (266)$$

where $K_{I,0}^m$ and $K_{II,0}^m$ are material constants and $K_{I,th}^m$ and $K_{II,th}^m$ are the microscopic threshold stress intensity factors for mode I and mode II, respectively.

4.4.2 Stress intensity factor in anisotropic material

For microstructurally small cracks in polycrystalline material, the assumption of isotropic material property is no longer valid. The method for mode I and mode II stress intensity factor calculation used in Ref. [115, 124-127] is based on finite element methodology, which is applicable to orthotropic materials where cracks are arbitrarily oriented with respect to the principle axes of material orthotropy as shown in Figure 34.

$$\varepsilon_i^o = a_{ij}^o \sigma_j^o \quad (a_{ij}^o = a_{ji}^o, \quad i, j = 1, 2, \dots, 6) \quad (267)$$

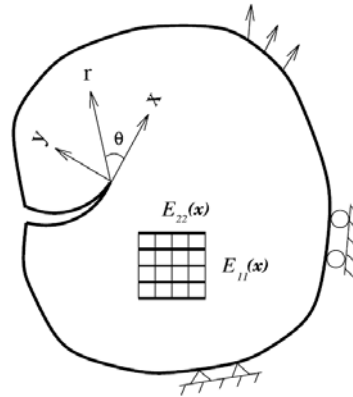


Figure 34. Coordinate system near crack tip

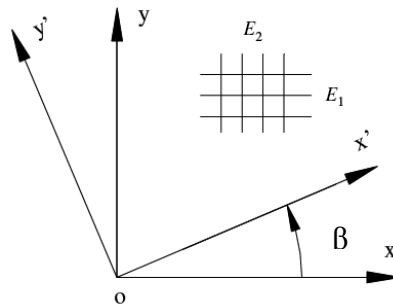


Figure 35. The complex parameters in two coordinate systems

If the coordinate at the crack tip is at an angle β with respect to the principal axes of the material as shown in Figure 35, the material compliance $[a_{ij}]$ in the coordinate at the crack tip can be calculated as

$$[a_{ij}] = [T]^T [a_{ij}^o] [T] \quad (268)$$

where

$$[T] = \begin{bmatrix} \cos^2 \beta & \sin^2 \beta & 2 \sin \beta \cos \beta \\ \sin^2 \beta & \cos^2 \beta & -2 \sin \beta \cos \beta \\ -\sin \beta \cos \beta & \cos \beta \sin \beta & \cos^2 \beta - \sin^2 \beta \end{bmatrix} \quad (269)$$

The relative displacements with respect to the crack tip in the x_i ($i = 1, 2$) direction can be expressed as

$$\begin{aligned} u_1 &= K_I \sqrt{\frac{2r}{\pi}} \operatorname{Re} \left[\frac{i}{\mu_1^{tip} - \mu_2^{tip}} (\mu_1^{tip} q_2 - \mu_2^{tip} q_1) \right] + K_{II} \sqrt{\frac{2r}{\pi}} \operatorname{Re} \left[\frac{i}{\mu_1^{tip} - \mu_2^{tip}} (q_2 - q_1) \right] \\ u_2 &= K_I \sqrt{\frac{2r}{\pi}} \operatorname{Re} \left[\frac{i}{\mu_1^{tip} - \mu_2^{tip}} (\mu_1^{tip} p_2 - \mu_2^{tip} p_1) \right] + K_{II} \sqrt{\frac{2r}{\pi}} \operatorname{Re} \left[\frac{i}{\mu_1^{tip} - \mu_2^{tip}} (p_2 - p_1) \right] \end{aligned} \quad (270)$$

The roots μ_k are always complex or purely imaginary in conjugate pairs as $\mu_1, \bar{\mu}_1, \mu_2, \bar{\mu}_2$, of which μ_1 and μ_2 must be calculated at the location of a crack tip.

$$a_{11}\mu^4 - 2a_{16}\mu^3 + (2a_{12} + a_{66})\mu^2 - 2a_{26}\mu + a_{22} = 0 \quad (271)$$

And p_k and q_k are given by

$$\begin{aligned} p_k &= a_{11}(\mu_k^{tip})^2 + a_{12} - a_{16}\mu_k^{tip} \\ q_k &= a_{12}\mu_k^{tip} + a_{22} / \mu_k^{tip} - a_{26} \end{aligned} \quad (272)$$

Thus the stress intensity factors at the crack tip are shown as

$$K_I = \frac{1}{4} \sqrt{\frac{2\pi}{\Delta a}} \frac{D(4u_{1,i-1} - u_{1,i-2}) - B(4u_{2,i-1} - u_{2,i-2})}{AD - BC}$$

$$K_{II} = \frac{1}{4} \sqrt{\frac{2\pi}{\Delta a}} \frac{A(4u_{2,i-1} - u_{2,i-2}) - C(4u_{1,i-1} - u_{1,i-2})}{AD - BC}$$
(273)

where $u_{1,i-1}$, $u_{1,i-2}$, $u_{2,i-1}$, and $u_{2,i-2}$ are the relative displacements with respect to the crack tip in the x_i ($i=1,2$) direction at locations $(i-1)$ and $(i-2)$, r is the distance from the crack tip along the local x_1 direction, and Δa is the characteristic length of the crack tip elements (see Figure 15).

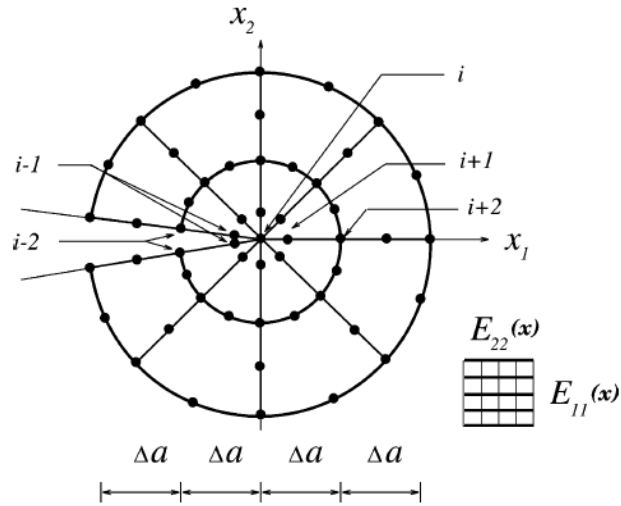


Figure 36. Crack tip elements

and

$$\begin{aligned}
A &= \operatorname{Re} \left[\frac{i}{\mu_1^{ip} - \mu_2^{ip}} (\mu_1 p_2 - \mu_2 p_1) \right] \\
B &= \operatorname{Re} \left[\frac{i}{\mu_1^{ip} - \mu_2^{ip}} (p_2 - p_1) \right] \\
C &= \operatorname{Re} \left[\frac{i}{\mu_1^{ip} - \mu_2^{ip}} (\mu_1 q_2 - \mu_2 q_1) \right] \\
D &= \operatorname{Re} \left[\frac{i}{\mu_1^{ip} - \mu_2^{ip}} (q_2 - q_1) \right]
\end{aligned} \tag{274}$$

4.4.3 Mixed mode I and II stress intensity factor

The primary mechanism of small fatigue crack growth in metals and alloys is crack-tip dislocation emission followed by the glide of the emitted dislocation. Both dislocation emission and glide are the result of a relative shear displacement in the direction of slip between the atoms of two neighboring slip planes, which is mainly driven by the shear stress field in the slip plane in the slip direction [128]. The hydrostatic stress on the slip plane also contributes to the dislocation movement.

To find the resolved normal and shear stresses of the slip system, a new coordinate is defined by three vectors, $\vec{b} = [b_1 \ b_2 \ b_3]$ as x' axis, $\vec{n} = [n_1 \ n_2 \ n_3]$ as y' axis and $\vec{l} = [l_1 \ l_2 \ l_3]$ as z' axis, where \vec{b} is the Burger's vector, which is along the slip direction, \vec{n} is the normal vector of slip plane, and \vec{l} is the vector perpendicular to both \vec{b} and \vec{n} and follows the right hand rule.

There are three major types of crystal structure as shown in Figure 37, FCC (face centered cubic. i.e. Al, Cu, γ -Fe and Ni), HCP (Hexagonal close-packing, i.e. α -Ti, Mg, Zn and Cd), and BCC (body centered cubic, i.e. α -Fe, Mo and W), where FCC has 12 slip systems, HCP has 3 and BCC has 48. For FCC structure with slip plane $\{111\}$ and

slip direction $\langle 1-10 \rangle$, the unit vectors \vec{n} and \vec{b} under new coordinate $x'y'z'$ can be expressed as

$$\vec{n} = \left[\frac{1}{\sqrt{3}} \quad \frac{1}{\sqrt{3}} \quad \frac{1}{\sqrt{3}} \right] \quad \vec{b} = \left[\frac{1}{\sqrt{2}} \quad -\frac{1}{\sqrt{2}} \quad 0 \right] \quad (275)$$

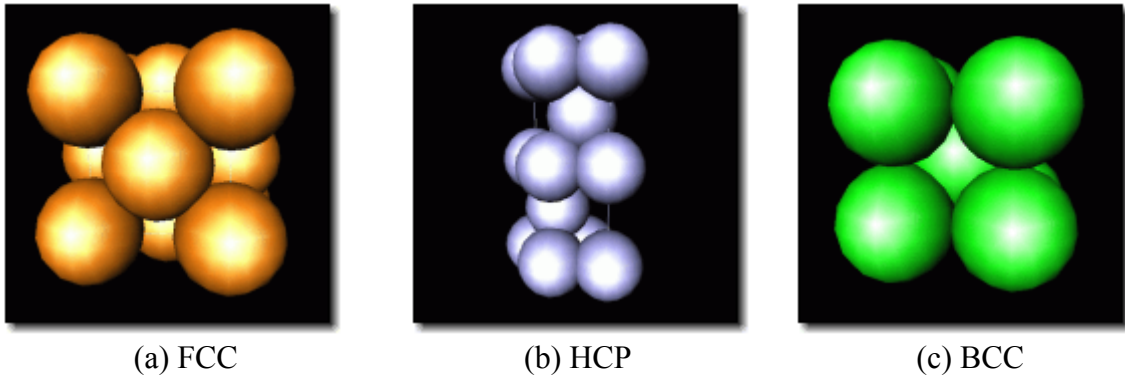


Figure 37. Crystal structures

The micro-crack is assumed to propagate along the slip plane and has to overcome the grain boundary in order to continue to grow [129]. If we know vectors \vec{n} and \vec{b} , the multiaxial fatigue limit criterion can be extended to a mixed mode threshold stress intensity factor criterion using Eqs.(265) and (266), which links the fatigue behavior of cracked and noncracked material together. Consider an infinite plate under remote tensional and torsional loading as shown in Figure 38, where x axis is along \vec{b} and y axis has the same direction as \vec{n} . There is a mixed mode I and II stress field near crack tip. The stress components on this new coordinate system $(\vec{b}\vec{n}\vec{l})$ can be expressed as

$$\sigma' = M^T \sigma M \quad (276)$$

where M is the transformation matrix and shown as

$$M = \begin{bmatrix} b_1 & n_1 & l_1 \\ b_2 & n_2 & l_2 \\ b_3 & n_3 & l_3 \end{bmatrix} \quad (277)$$

Thus the normal stress and shear stress under new coordinate are

$$\begin{aligned} \sigma_{r'r'} &= b_1^2 \sigma_{rr} + b_2^2 \sigma_{\theta\theta} + 2b_1 b_2 \tau_{r\theta} \\ \sigma_{\theta'\theta'} &= n_1^2 \sigma_{rr} + n_2^2 \sigma_{\theta\theta} + 2n_1 n_2 \tau_{r\theta} \\ \sigma_{z'z'} &= \sigma_{zz} \\ \tau_{r'\theta'} &= b_1 n_1 \sigma_{rr} + b_2 n_2 \sigma_{\theta\theta} + (b_1 n_2 + b_2 n_1) \tau_{r\theta} \end{aligned} \quad (278)$$

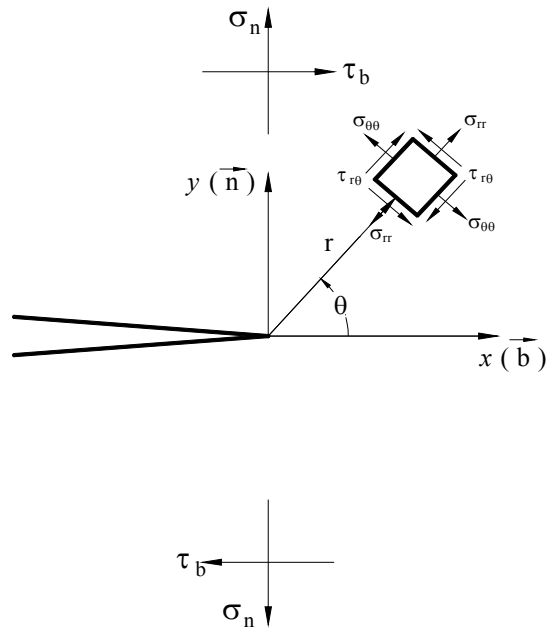


Figure 38. Mixed mode I and II stress fields near small crack tip

$$\begin{aligned}
\sigma_{r'r'} &= \frac{1}{\sqrt{2\pi r}} \cos\left(\frac{\theta}{2}\right) \left[K_{I(n)} \left(1 + \sin^2\left(\frac{\theta}{2}\right)\right) + K_{II(b)} \left(\frac{3}{2} \sin(\theta) - 2 \tan\left(\frac{\theta}{2}\right)\right) \right] \\
\sigma_{\theta'\theta'} &= \frac{1}{\sqrt{2\pi r}} \cos\left(\frac{\theta}{2}\right) \left[K_{I(n)} \cos^2\left(\frac{\theta}{2}\right) - \frac{3}{2} K_{II(b)} \sin(\theta) \right] \\
\sigma_{z'z'} &= \begin{cases} 0 & \text{plane stress} \\ \nu(\sigma_{\theta\theta} + \sigma_{rr}) & \text{plane strain} \end{cases} \\
\tau_{r'\theta'} &= \frac{1}{2\sqrt{2\pi r}} \cos\left(\frac{\theta}{2}\right) \left[K_{I(n)} \sin(\theta) + K_{II(b)} (3 \cos(\theta) - 1) \right]
\end{aligned} \tag{279}$$

To unify the multiaxial fatigue limit criterion for both plane stress and plane strain condition, a new parameter A^* is introduced which is the same as A under plane stress condition and equals to $A(1+\nu)^2$ under plane strain condition. Thus Eq. (41) can be expressed as

$$\sqrt{\left(\frac{\sigma_{\theta'\theta'}}{f_{-1}}\right)^2 + \left(\frac{\tau_{r'\theta'}}{t_{-1}}\right)^2 + A^* \left(\frac{\sigma_{\theta'\theta'} + \sigma_{r'r'}}{3f_{-1}}\right)^2} = B \tag{280}$$

Following the same procedure in sections 2.3.3 and 2.3.4, parameters A^* and B in Eq. (280) can be calculated using the two extreme cases according to maximum shear stress criterion. The threshold condition can be expressed as

$$\sqrt{\left(\frac{\cos\left(\frac{\alpha}{2}\right) \left[K_{I(n)} \cos^2\left(\frac{\alpha}{2}\right) - \frac{3}{2} K_{II(b)} \sin(\alpha) \right]}{K_{I,th}^m}\right)^2 + \left(\frac{\frac{1}{2} \cos\left(\frac{\alpha}{2}\right) \left[K_{I(n)} \sin(\alpha) + K_{II(b)} (3 \cos(\alpha) - 1) \right]}{\xi K_{I,th}^m}\right)^2 + A \left(\frac{2 \cos\left(\frac{\alpha}{2}\right) \left[K_{I(n)} - K_{II(b)} \tan\left(\frac{\alpha}{2}\right) \right]}{3K_{I,th}^m}\right)^2} = B \tag{281}$$

where $\alpha = \beta + \gamma$. Parameters γ , β and B are shown in Figure 4, Figure 6 and Figure 5.

Then, the equivalent mixed-mode microscopic threshold stress intensity factor

$K_{mix,eq}^m$ can be derived as

$$\begin{aligned}
K_{mix,eq}^m &= \frac{\left|\cos\left(\frac{\alpha}{2}\right)\right|}{B} \sqrt{\left(K_{I(b)} \cos^2\left(\frac{\alpha}{2}\right) - \frac{3}{2} K_{II(b)} \sin(\alpha)\right)^2 + \frac{1}{4\xi^2} \left(K_{I(n)} \sin(\alpha) + K_{II(b)} (3 \cos(\alpha) - 1)\right)^2 + \frac{4}{9} A \left(K_{I(n)} - K_{II(b)} \tan\left(\frac{\alpha}{2}\right)\right)^2} \\
&= K_{I,da/dN} = f\left(\frac{da}{dN}\right)
\end{aligned} \tag{282}$$

where $f\left(\frac{da}{dN}\right)$ is the crack growth curve obtained under mode I loading. After this, Paris law is applied for the small fatigue crack growth rate prediction.

4.5 Conclusion

A new model for mixed-mode I and II microscopic threshold stress intensity factor and small fatigue crack growth rate prediction is proposed in this chapter. The proposed fatigue crack growth model is developed using the local stress components on the slip plane and the characteristic plane concept. The relationship between fatigue limit and microscopic threshold stress intensity factor is expressed using Eq. (264) for small cracks. The stress intensity factors near small crack tip are shown as Eq. (273). Then, the equivalent mixed-mode microscopic threshold stress intensity factor $K_{mix,eq}^m$ is calculated by Eq. (282).

Three major advantages of the proposed model are that (1) it can automatically adapt for different failure mechanisms, as the models for near threshold cracks, (2) it considers anisotropic material properties and (3) it considers blocked slip band and the influence of various microstructural factors.

CHAPTER V

APPLICATION TO RAILROAD WHEELS

5.1 Overview

Unlike the slow deterioration process of wear, wheel failure caused by propagating fatigue cracks is more abrupt and violent. A part of the wheel or the entire wheel breaks off, which results in the damage of rail, sleepers, train suspensions and, in some cases, serious derailment of the train [130].

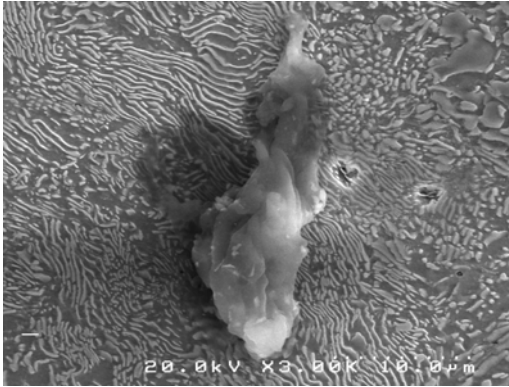
There are three types of cracks caused by the rolling contact stresses between wheel and rail during the rolling motion: surface crack which is initiated by the severe plastic deformation induced by contact stresses, sub-surface crack which is facilitated by the presence of structural inhomogeneities such as inclusions or pores and driven by sub-surface contact stresses, and deep defects which acts as cracks, and if large enough, propagate in low stress region far from the contact patch. A detailed overview of the rolling contact problem of railroad wheels is presented in references [131, 132]. The large subsurface cracks that propagate roughly parallel to the wheel tread surface [133, 134] result in shattered rim failure that can destroy the wheel's integrity and leads to train derailments at high speed.

Shattered rim cracks originate from inclusions in wrought wheels and pores in cast wheels [135]. Types of material defects detected using Scanning Electron Microscope (SEM) include non-metallic inclusions, such as manganese sulfide and silicon oxide, metallic inclusions, such as aluminum oxides, and pores in the wheel

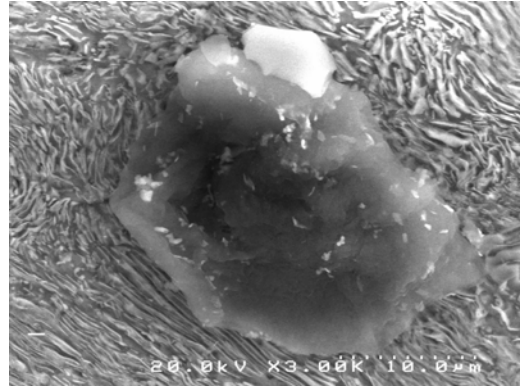
material as shown in Figure 39. The effective size of defects varies between 1 μm and 31 μm , using the Murikami criterion [136].

Several studies have been reported on shattered rim crack initiation from material defects [137-140]. Lunden [137] and Marais [139] estimated that a defect (pore or inclusion) of size 1 mm can initiate shattered rims. Stone and Dahlman [140] provided micrographic evidence that a shattered rim crack initiated from a void of size 0.64 mm. Baretta et al. [138] estimated the typical dimensions of aluminum oxide inclusions in wrought wheel for shattered rim initiation have a length of 1 to 5 mm and width of 0.3 to 1 mm. Ekberg [130] modeled material defects as pores, which are considered to be worse than inclusions [141, 142], using small circular holes. In all of the above studies, the material is assumed to be isotropic.

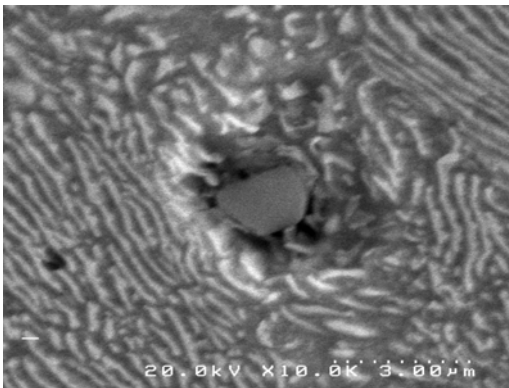
The Scanning Electron Microscope pictures show that the microstructure of wheel steel can be characterized as a ferrite-pearlite structure [143] in which ferrite has a body-centered cubic grain structure. The wheel material studied in this paper has an average grain size around 10 μm . The material exhibits an anisotropic microstructure. In this paper, a micro-level 2-D finite element model considering elasticity anisotropy is used to represent the polycrystalline wheel steel. The grain structure is established using Voronoi tessellation. The initial material defects are modeled as center or edge cracks.



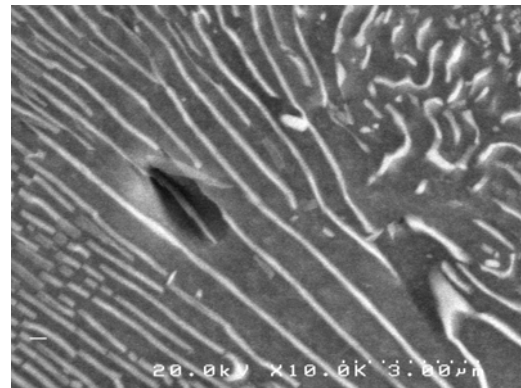
(a) – Silicon (inclusion)



(b) – Aluminum (inclusion)



(c) – Pore



(d) – Pore

Figure 39. Inclusions and pores in wheel material

Most of the existing rolling contact fatigue models use a simplified stress calculation technique, such as Hertz analytical solution or simplified finite element analysis with applied Hertz contact pressure. Due to the complex geometry of the wheel/rail contact area, it is more appropriate to use a 3D finite element method to calculate stress response in the mechanical components. It has been shown that the Hertz contact theory is not appropriate when the contact area between wheel and rail is near the wheel flange [9]. It is also desirable to include other factors which cannot be included in

the simplified method, such as material nonlinearity, irregular surface conditions and hunting movement of the wheel. Liu et al [9] proposed a macro-level finite element computational methodology to calculate the complex 3D stress histories of wheel/rail contact. The equivalent stress history at the critical location calculated by the multiaxial fatigue theory [9] in the macro-level model is used for the fatigue crack propagation analysis in the present micro-level model.

A general methodology for subsurface fatigue crack propagation analysis of railroad wheels is proposed in this paper. It combines a macro-micro finite element model for the wheel/rail contact analysis and a multiaxial fatigue limit criterion previously developed by Liu and Mahadevan [9]. The advantages of the proposed methodology are: (i) The fatigue model can automatically adapt for tensile/shear failure mechanisms according to material properties and loading conditions; (ii) The macro-level 3-D finite element model is versatile in representing complex wheel tread (or rail head) profiles, which is especially important when the contact conditions can not satisfy the Hertz assumptions; (iii) The micro-level 2-D finite element model considers material anisotropy, and randomness in both grain size and grain orientation. The effects of applied load, crack size, grain orientation and grain disorientation on the mixed mode equivalent stress intensity factor are investigated using the proposed model.

5.2 Finite element modeling of subsurface crack in wheel/rail contact

Liu et al [9] proposed a finite element computational methodology for rolling contact analysis of railroad wheels. It has several advantages compared with previous analytical and numerical approaches. First, it is a realistic macro-level 3D finite element

model and can accurately calculate the 3D stress response in the contact region. Second, it includes both material and geometric nonlinearity. It can be used to simulate large and complex wheel motions, such as rotation, sliding, hunting movement and even dynamic impact response. Finally, through sub-modeling techniques, the proposed model is made efficient in computing and hardware requirements. After the macro-level rolling contact stress analysis, the equivalent stress amplitude at the critical location, which is calculated using the previously developed multi-axial fatigue limit criterion, is applied to a micro-level 2-D finite element model with center or edge crack. A brief description of both macro-level and micro-level finite element computational methodology is given below.

(1) Macro-level full model and submodel

First, use the available profiles to build the geometry model of the wheel and a piece of rail. This model is called the full model as shown in Figure 40(a). The rail length equals the length between two sleepers. Fixed boundary conditions are applied to the two ends of the rail. Different 3D element sizes are used in the full model (SOLID 45 in ANSYS [144]). In the contact region, relatively finer mesh is used. At the wheel center, a pilot point is connected to the wheel using rigid link elements. All the external loading and boundary conditions of the wheel are applied on the pilot point. These loading and boundary conditions can be obtained through field measurements or from numerical simulation of the track system motion analysis. On the possible contact areas of the railhead and the wheel tread, area contact elements (CONTACT 174 and TARGET 170 in ANSYS) are used corresponding to the geometry mesh of the wheel. The contact algorithm is augmented Lagrangian method [144]. Friction effect is included in the material properties of the contact element. A Coulomb friction model is used. Friction

coefficients can be calibrated using field measurement data. The material properties of the wheel and rail as described using a bilinear kinematic hardening model in ANSYS. No isotropic hardening is included in the current model.

Next, quasi-static analysis is performed for the full model and the results for each step are stored. Then the geometry model of the contact region is cut out to create a sub-model as shown in Figure 40(b). The size of the sub-model depends on the analysis objective and also on the wheel motion simulated. The same types of elements as those in the full-model analysis are used to mesh the sub-model. A very fine mesh is used in the contact area and to some depth under the contact surface. The results of the full-model are interpolated on the cutting edge of the sub-model corresponding to different calculation steps, and the interpolation results are applied as boundary conditions to the sub-model.

(2) Micro-level FEM model

A 2-D representative volume element (RVE) is generated using the Voronoi tessellation at the critical location as shown in Figure 40(c). The critical location is determined using the method shown in Section 2, which is consistent with the field observation of subsurface crack in railroad wheels. The coordinates of the vertices of the Voronoi diagram and the connection relationship of the vertices (generated in MATLAB) are input to the finite element analysis (using ANSYS). Each Voronoi cell represents one grain with a random grain orientation. The origin of each local coordinate system is located at the center of gravity of each grain and the x -axis lies in the direction of the $[100]$ direction of the crystal lattice in the grain. In the present simulation, the slip plane is assumed to be the $(\bar{1}\bar{1}0)$ plane which is at 45° to the grain orientation. The average

grain size is $10\mu m$. One RVE can consist of up to 100 grains, which represents an area of $0.01mm^2$ of the real material. A center crack is built into the micro-level model along the slip plane. The center of the crack is located at the center of gravity of the specific grain. The micro-crack is assumed to propagate along the slip plane and has to overcome the grain boundary in order to continue to grow [129]. Friction effect is not included between the two crack surfaces. The FEM mesh for each grain is built with SOLID 183 element in ANSYS. A very fine mesh (average element length of about $0.1\mu m$) is applied near the crack tip.

The finite element models of the macro-level full model, sub-model and micro-level sub-model with the crack are shown in Figure 40. The wheel profile is chosen according to the AAR standard [145] wide flange contour. The wheel diameter is 0.914 meter (36 inches). The subsurface crack is assumed to be located 5 mm below the wheel tread surface. The crack length $2a$ is $1\mu m$. The vertical load applied on the wheel is assumed to be the maximum design load, which is 146.2 KN (32,875 lb.). The material properties of the rail and wheel are assumed to be the same (yielding strength = 500 MPa; Young's Modulus= 205 MPa; Poisson's ratio = 0.3, Friction coefficient = 0.3). The rail length is 600mm, which is normally the length between two sleepers. In the current study, the initial contact point is assumed to occur at the railhead center and wheel tread center.

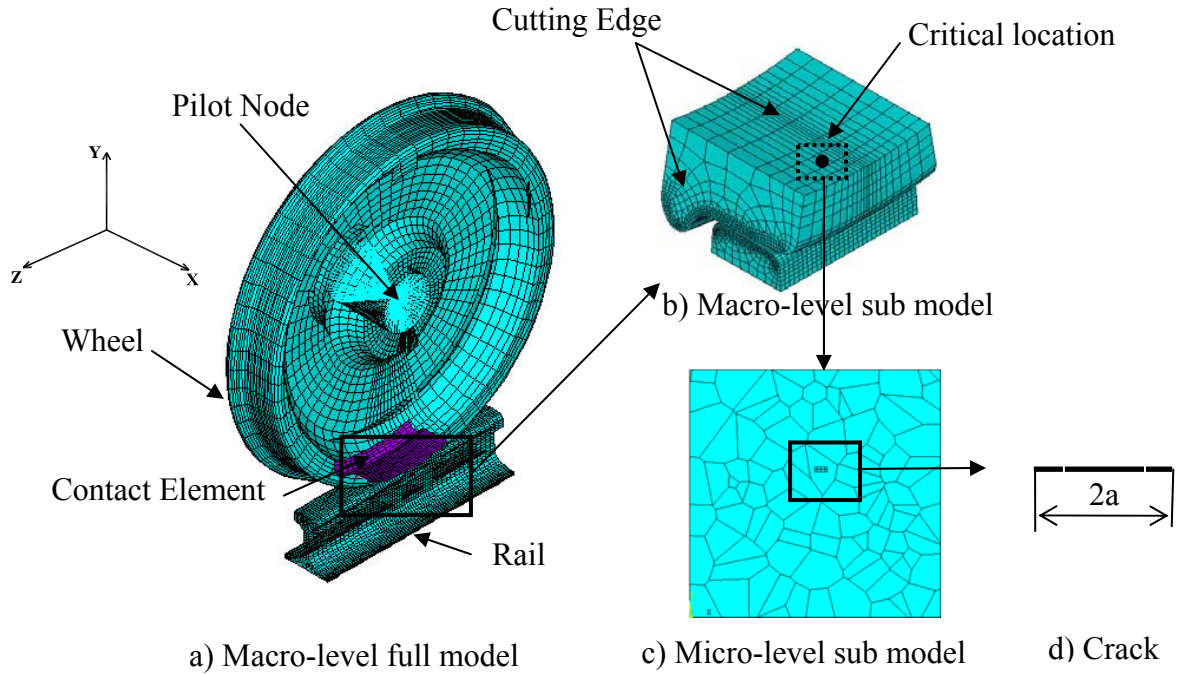


Figure 40. Finite element modeling of wheel/rail contact with subsurface crack

The static load analysis of the wheel/rail contact is performed first. The results of the macro-level sub model are shown in Figure 41 and Figure 42. Figure 41 shows the Von Mises stresses from two different section views. Figure 42 shows two in-plane shear stresses (τ_{xy} and τ_{yz}) from two different section views. From Figure 41, it is found that the maximum Von Mises stress occurs at some depth below the tread surface. The stress decreases quickly as the depth increases. The maximum Von Mises stress is computed around the crack tip, which is caused by the stress singularity near the crack tip. From Figure 42, a butterfly pattern of the shear stress τ_{yz} is observed. The maximum value occurs at the crack tip. Figure 41 and Figure 42 show that the high stress only occurs within a small region of the contact location. The stress in the other parts of the model is

almost zero. This indicates that only a small portion of the motion simulation is needed because the stress far away from the contact location is negligible.

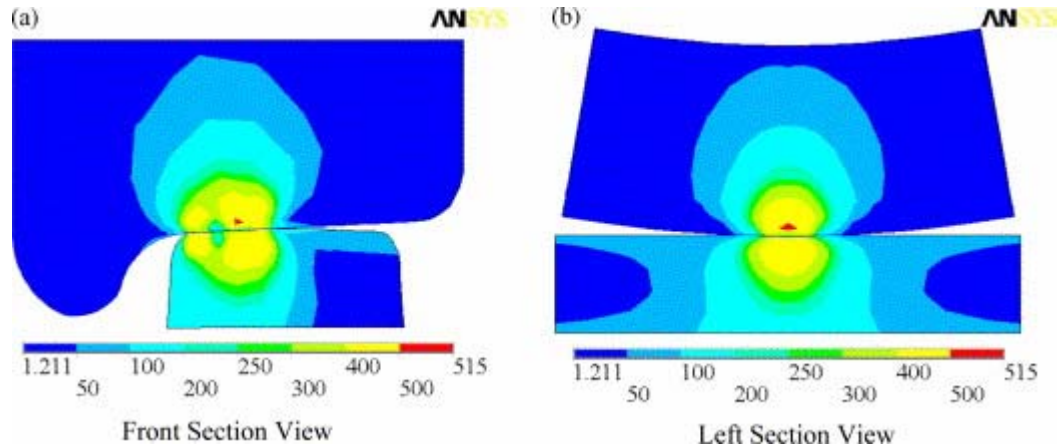


Figure 41. Von-Mises stress distribution of wheel/rail contact

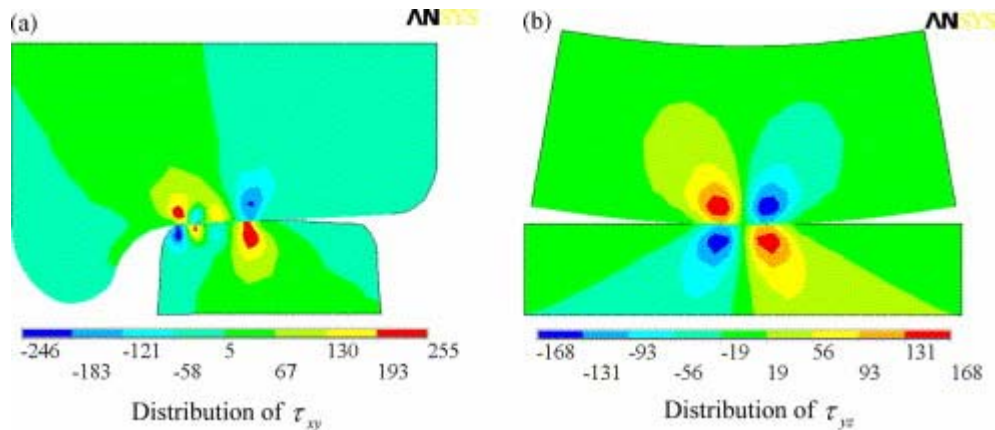


Figure 42. In-plane shear stress distribution of wheel/rail contact

After performing the static analysis, we simulate the wheel rotation on the rail, which is the normal motion mode of the wheel. This is done by applying the proper boundary conditions on the pilot node in the full model. The stress histories of two points (one is 3 mm below the tread surface, the other is 10 mm below the tread surface) during

half a revolution of the wheel rotation are plotted in Figure 43. The x -axis does not indicate the real time and is the time step in FE analysis during the simulation of wheel rotating. Figure 43 shows that the stress history in the wheel when rolling contact loading is not proportional, which indicates that the maximum normal stress and maximum shear stress do not occur simultaneously. The normal stress amplitude decreases from a depth of 3 mm to 10 mm. The FEA results only show very small residual stresses at these two locations. They can be barely seen in Figure 43 and their effects are negligible in the current analysis. The critical location with maximum equivalent stress amplitude of 200Mpa is found to be at 5 mm below the tread surface. This load is applied as a uniaxial tensile load to the top of the micro-level sub-model.

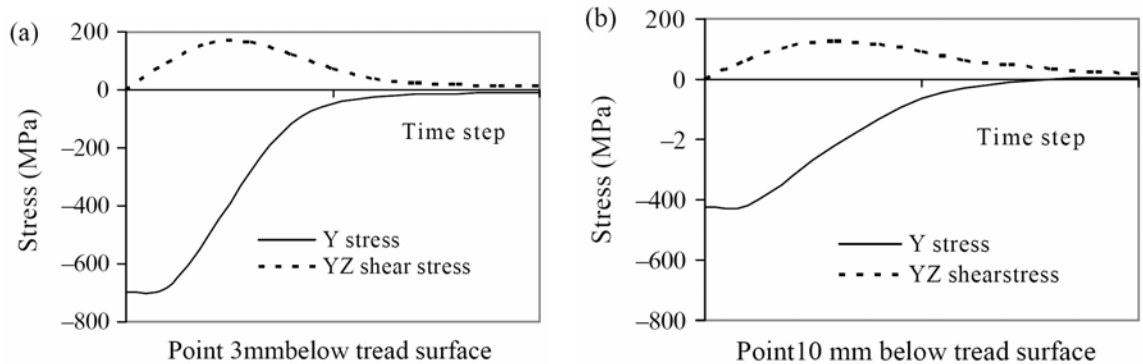


Figure 43. Stress history at two locations in the wheel.

4 Parametric study

In this section, the influence of several factors on the crack tip mixed mode equivalent stress intensity factor is studied, using the developed methodology described above. These factors are applied load F , crack size a , grain orientation $[100] \theta_g$, and

grain disorientation ϕ_g , as shown in Figure 44. The details about the parametric study are shown below.

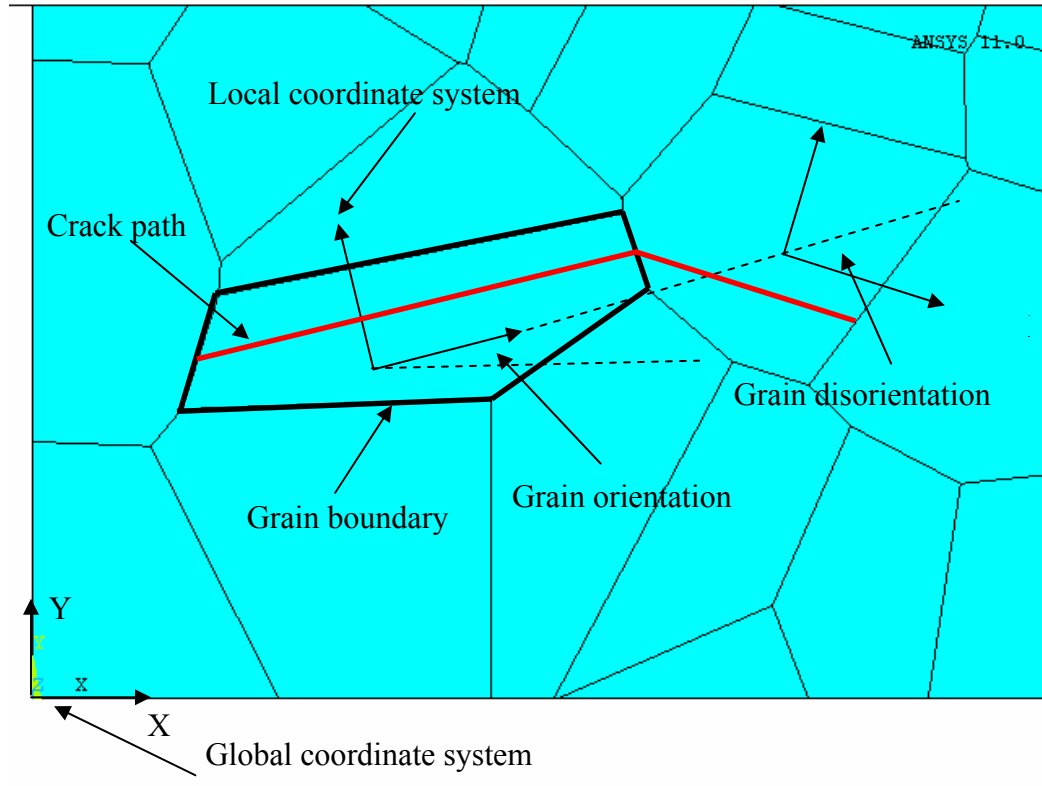


Figure 44. Parameters used in parametric study

The applied load on the micro-level sub-model will affect the small fatigue crack propagation. 21 loading conditions are studied (from 100 Mpa to 300 Mpa with increment 10 Mpa). The other parameters are fixed for all the simulations, which are crack size ($3 \mu m$) and the grain orientation of the grain with crack (0°). The mixed mode equivalent stress intensity factor, $\Delta K_{mix,eq}$, for different load are plotted in Figure 45. It is seen that $\Delta K_{mix,eq}$ increases as the applied load increases almost linearly.

The effects of different crack lengths (from $1 \mu m$ to $7 \mu m$ with increment $1 \mu m$) are plotted in Figure 46. The other parameters are fixed for all the simulations, which are the applied load (200 Mpa) and the grain orientation of the grain with crack (0°). Similar to the parametric study for applied load, $\Delta K_{mix,eq}$ increases as the crack length increases which is consistent with long crack propagation.

The effects of different grain orientations (from -90° to 90° at increments of 5°) are plotted in Figure 47. The other parameters are fixed for all the simulations, which are crack size ($3 \mu m$) and the applied load (200 Mpa). It is seen that as grain orientation approaches to -45° , which means the crack as well as the slip plane of the grain approaches to the plane perpendicular to the applied load, ΔK_I increases while ΔK_{II} decreases. The mixed mode equivalent stress intensity factor, $\Delta K_{mix,eq}$, decreases. After that as crack approaches to the plane parallel to the applied load, ΔK_I decreases while ΔK_{II} increases first and then decrease. As a result, $\Delta K_{mix,eq}$ increase a little bit at first then keep decreasing to zero when the grain orientation is equal to 45° . As grain orientation increases from 45° to 90° , which means the crack is rotating from parallel to the applied load to at 45° deviation from the applied load, $\Delta K_{mix,eq}$ increase.

The effects of different grain disorientations (from -45° to 45° with increment 5°) are plotted in Figure 48. The other parameters are fixed for all the simulations, which are the kinked crack size ($3 \mu m$) and the applied load (200 Mpa). The original crack is at 45° deviation from the applied load as shown in Figure 49 and the kinked crack rotate from perpendicular to the applied load to parallel to it. From Figure

12, $\Delta K_{mix,eq}$ increases a little bit then decreases to the minimum where grain disorientation is equal to 45° . ΔK_I has maximum value while ΔK_{II} is almost zero when the grain disorientation equals to -45° , which means the kinked crack is perpendicular to the applied load. As grain disorientation increases to 45° , ΔK_I approaches zero. ΔK_{II} has the maximum value as the two neighboring grains have the same orientation. As the grain disorientation increases, ΔK_{II} decreases. The FEM mesh and Von-Mises stress distribution near the crack tip are shown in Figure 49.

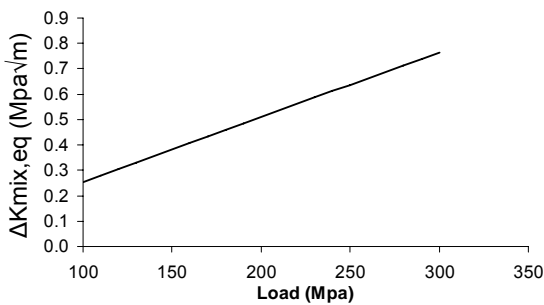


Figure 45. $\Delta K_{mix,eq}$ vs. applied load

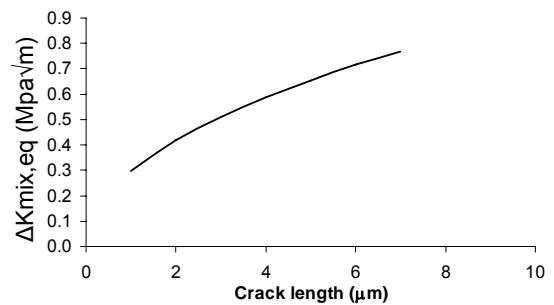


Figure 46. $\Delta K_{mix,eq}$ vs. crack length (2a)

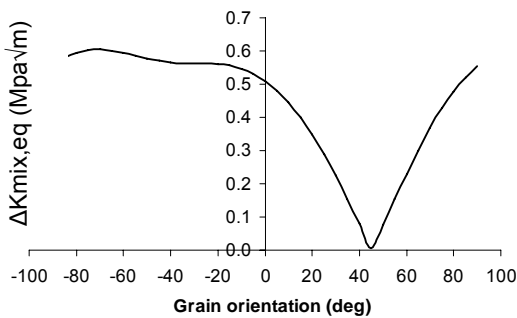


Figure 47. $\Delta K_{mix,eq}$ vs. grain orientation

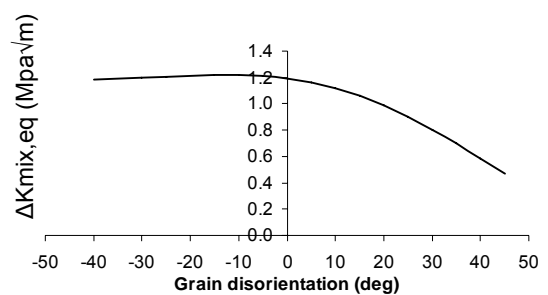


Figure 48. $\Delta K_{mix,eq}$ vs. grain disorientation

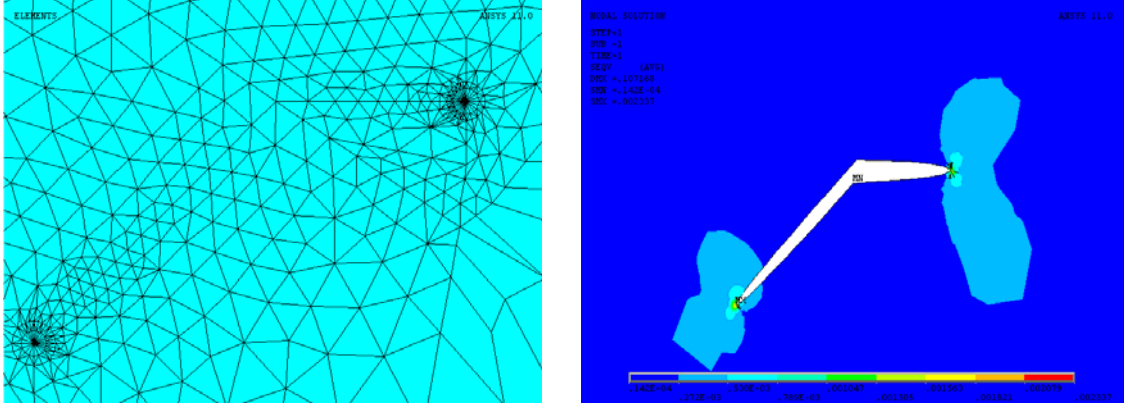


Figure 49. Mesh and Von-Mises stress distribution near crack tip

After obtaining the mixed-mode equivalent stress intensity factors for each parameter, ΔK_{eq} can be expressed as a function of the applied load F , crack size a , grain orientation θ_g , and grain disorientation ϕ_g

$$\Delta K_{eq} = f(F, a, \theta_g, \phi_g) \quad (283)$$

The general crack propagation function, which includes the stress ratio effect, is expressed as

$$\frac{da}{dN} = C \left(\frac{\Delta K_{eq}}{(1-R)^\gamma} \right)^m \quad (284)$$

where $\frac{da}{dN}$ is the crack growth rate, ΔK_{eq} is the equivalent stress intensity factor range for mixed-mode loading, R is the stress ratio, C , m and γ are material parameters.

Substituting Eq. (283) into Eq. (284) and solve for fatigue life.

$$N(a) = \frac{1}{C} \int_{a_0}^{a_f} \frac{(1-R)^\gamma}{(\Delta K_{eq})^m} da = \frac{1}{C} \int_{a_0}^{a_f} \frac{(1-R)^\gamma}{(f(F, a, \theta_g, \phi_g))^m} da \quad (285)$$

where $N(a)$ is the number of cycles to growth a crack from the initial length a_0 to the length a_f .

5.3 Conclusion

A general subsurface fatigue crack propagation model under rolling contact conditions of railroad wheels is developed in this chapter, which combines a macro-micro finite element computational method and a previously developed multiaxial fatigue limit criterion. The macro-level finite element analysis is used for stress computation. The micro-level finite element analysis is used for the calculation of fracture parameter $\Delta K_{mix,eq}$. The effects of four parameters, namely applied load, crack size, grain orientation and grain disorientation, on the mixed mode equivalent stress intensity factor are studied using the proposed model.

Parametric study shows that both macro-structural parameters (applied load and crack size) and micro-structural parameters (grain orientation and grain disorientation) have significant effects on $\Delta K_{mix,eq}$ of the subsurface crack. Since the initial defects in railroad wheels are comparable to grain size, the micro-level model which is capable of modeling material anisotropy is necessary for the initial defects analysis.

This study focused on testing the effects of microstructures on the fracture parameters under rolling contact fatigue loading. The life prediction of railroad wheels with microstructurally small fatigue cracks needs further study. Also, other effects influencing the shattered rim failure, such as manufacturing process parameters, residual stress, and brake thermal loading need to be investigated in the future.

CHAPTER VI

CONCLUSION AND FUTURE WORK

6.1 Summary of contribution

Analytical and experimental approaches to determine mixed-mode fatigue crack growth threshold and growth rates are not well established and remain an active research topic. This study compared the existing methods and proposed some alternatives to address the problem with less assumptions and broader applicability. The proposed models are based on a characteristic plane methodology [9] and extend the stress/strain-based approach to fracture mechanics-based approach. Both shear-dominated failure and tension-dominated failure can be analyzed. The orientation of the characteristic plane changes according to the mode mixity, the ratio of shear fatigue limit over tensile fatigue limit, and the crack/notch tip radius for near threshold crack. It also depends on the grain orientation for microstructurally small crack.

The effect of microstructure on the propagation of small fatigue cracks under rolling contact fatigue loading is examined in this dissertation. The local stress history is calculated using a macro-level 3-D elasto-plastic finite element model. A sub-modelling technique is used to achieve both computational efficiency and accuracy. The macro-level finite element model can accurately represent the contact stress of complex mechanical components and can consider the effect of loading non-proportionality. Then the equivalent stress amplitude at the critical location, which is calculated using a previously developed multiaxial fatigue limit criterion, is applied to a micro-level 2-D

finite element model with center or edge crack. The fatigue model can automatically adapt for tensile/shear failure mechanisms according to material properties and loading conditions. Elasticity anisotropy, and randomness in both grain size and grain orientation are considered in the micro-level model. The geometric patterns of the grains in the polycrystalline wheel steel are generated using a 2D voronoi tessellation. The effects of applied load, crack size, grain orientation and grain disorientation on the mixed mode equivalent stress intensity factor are investigated using the proposed model.

6.2 Future work

Since the proposed models in this dissertation use local stress near crack/notch tip, local geometry and manufacturing induced residual stress effects can be easily captured. The models in this dissertation are mainly for constant amplitude loading. The potential application for random amplitude multiaxial loading needs to be studied. Linear elastic fracture mechanics is assumed in this dissertation; the proposed approach needs to be extended to include the crack/notch tip plasticity effects. Also this approach has the potential to be applied to anisotropic materials and functionally graded materials in future.

In this dissertation analytical models are proposed for threshold fatigue crack growth prediction in U-notched specimen. Future work is needed to extend the proposed models to V-notch and radiused V-notched specimen, by simply replacing the local stress expression according to the notch configuration and follow the similar derivation for U-notched specimen.

This study focused on testing the effects of microstructure on the fracture parameters under rolling contact fatigue loading. The life prediction of railroad wheels with microstructurally small fatigue cracks needs further study. A more realistic 3D micro-model is needed to address the effects of inclusions and voids on fatigue life prediction. The micro structural parameters on crack rotation, twist and retardation need to be explored. Also, other effects influencing the failure of railroad wheels, such as manufacturing process parameters, residual stress, brake thermal loading, and wear and fatigue interaction, need to be investigated in the future.

REFERENCES

1. FAA, *Rotorcraft Damage Tolerance (RCDT) for Metallic Materials*. 2006, FAA.
2. Vaughan, R.E., R. Arsenal, and J.H. Chang. *Life predictions for high cycle dynamic components using damage tolerance and small threshold cracks*. in *American Helicopter Society 59th Annual Forum*. 2003. Phoenix, Arizona.
3. Le, D. and M. Kanninen. *The development of a methodology for quantifying fatigue crack growth in residual stress fields for application to rotorcraft design and maintenance*. in *ASTM Symposium on the Residual Effects on Fatigue and Fracture Testing and Incorporation of Results Into Design, ASTM Proceeding*. 2004.
4. Chang, J.B., M. Szamossi, and K.W. Liu, *Random spectrum fatigue crack life predictions with or without considering load interactions*. ASTM Special Technical Publication, 1981: p. 115-132.
5. Wei, L.W., E.R. de los Rios, and M.N. James, *Experimental study and modelling of short fatigue crack growth in aluminium alloy Al7010-T7451 under random loading*. *International Journal of Fatigue*, 2002. **24**(9): p. 963-975.
6. James, M.N. and E.R. de los Rios, *Variable amplitude loading of small fatigue cracks in 6261-T6 aluminium alloy*. *Fatigue and Fracture of Engineering Materials & Structures*, 1996. **19**(4): p. 413-426.
7. Moshier, M.A., T. Nicholas, and B.M. Hillberry, *Load history effects on fatigue crack growth threshold for Ti-6Al-4V and Ti-17 titanium alloys*. *International Journal of Fatigue*, 2001. **23**(Supplement 1): p. 253-258.
8. Moshier, M.A., B.M. Hillberry, and T. Nicholas, *The effect of low-cycle fatigue cracks and loading history on the high cycle fatigue threshold*, in *Fatigue and fracture mechanics*, J.P. Gallagher, Editor. 2000, American Society for Testing and Materials: West Conshohocken. p. 427-444.
9. Liu, Y. and S. Mahadevan, *Multiaxial high-cycle fatigue criterion and life prediction for metals*. *International Journal of Fatigue*, 2005. **27**(7): p. 790-800.
10. Liu, Y., *Stochastic modeling of multiaxial fatigue and fracture*, in *Civil and Environmental Department*. 2006, Vanderbilt University: Nashville. p. 215.
11. Kitagawa, H. and S. Takahashi. *Applicability of fracture mechanics to vary small cracks or cracks in early stage*. in *2nd International Conference on Mechanical behavior of Materials*. 1976. Metal Park (OH,USA): ASM International.

12. Papadopoulos, I.V., et al., *A comparative study of multiaxial high-cycle fatigue criteria for metals*. International Journal of Fatigue, 1997. **19**(3): p. 219-235.
13. You, B.-R. and S.-B. Lee, *A critical review on multiaxial fatigue assessments of metals*. International Journal of Fatigue, 1996. **18**(4): p. 235-244.
14. Karolczuk, A. and E. Macha, *A review of critical plane orientations in multiaxial fatigue failure criteria of metallic materials*. International Journal of Fracture, 2005. **134**(3): p. 267-304.
15. Bold, P., M. Brown, and R. Allen, *A review of fatigue crack growth in steels under mixed mode I and II loading*. Fatigue and Fracture of Engineering Materials and Structures, 1992. **15**(10): p. 965-977.
16. Qian, J. and A. Fatemi, *Mixed mode fatigue crack growth: A literature survey*. Engineering Fracture Mechanics, 1996. **55**(6): p. 969-990.
17. Liu, Y. and S. Mahadevan, *Strain-based multiaxial fatigue damage modelling*. Fatigue & Fracture of Engineering Materials and Structures, 2005. **28**(12): p. 1177-1189.
18. Varvani-Farahani, A., *A new energy-critical plane parameter for fatigue life assessment of various metallic materials subjected to in-phase and out-of-phase multiaxial fatigue loading conditions*. International Journal of Fatigue, 2000. **22**(4): p. 295-305.
19. Kim, K.S., et al., *A fatigue life model for 5% chrome work roll steel under multiaxial loading*. International Journal of Fatigue, 2004. **26**(7): p. 683-689.
20. Jiang, *A fatigue criterion for general multiaxial loading*. Fatigue & Fracture of Engineering Materials and Structures, 2000. **23**(1): p. 19-32.
21. Jiang, Y. and M. Feng, *Modeling of fatigue crack propagation*. Journal of Engineering Materials and Technology, 2004. **126**: p. 77-86.
22. Feng, M., F. Ding, and Y. Jiang, *A study of crack growth retardation due to artificially induced crack surface contact*. International Journal of Fatigue, Fatigue Damage of Structural Materials V, 2005. **27**(10-12): p. 1319-1327.
23. Erdogan, F. and G.C. Sih, *On the crack extension in plates under plane loading and transverse shear*. J Basic Engng, 1963. **85**: p. 650-652.
24. Chambers, A.C., T.H. Hyde, and J.J. Webster, *Mixed mode fatigue crack growth at 550[degree sign]c under plane stress conditions in Jethete M152*. Engineering Fracture Mechanics, 1991. **39**(3): p. 603-619.

25. Yan, X., Z. Zhang, and S. Du, *Mixed-mode fracture criteria for the materials with different yield strengths in tension and compression*. *Engineering Fracture Mechanics*, 1992. 42: p. 109-116.
26. Forth, S.C., et al., *Three-dimensional mixed-mode fatigue crack growth in a functionally graded titanium alloy*. *Engineering Fracture Mechanics*, 2003. 70(15): p. 2175-2185.
27. Sih, G.C. and B.M. Barthelemy, *Mixed mode fatigue crack growth predictions*. *Engineering Fracture Mechanics*, 1980. 13(3): p. 439-451.
28. Theocaris, P.S. and N.P. Andrianopoulos, *The T-criterion applied to ductile fracture*. *Int J Fract*, 1982. 20: p. 125-130.
29. Chao, Y.J. and S. Liu, *On the failure of cracks under mixed-mode loads*. *Int J Fract*, 1997. 87: p. 201-223.
30. Otsuka, A., K. Mori, and T. Miyata, *The condition of fatigue crack growth in mixed-mode condition*. *Engng Fract Mech*, 1975. 7: p. 429-439.
31. Socie, D.F., C.T. Hua, and D.W. Worthem, *Mixed-mode small crack growth*. *Fatigue Fract Engng Mater Struct*, 1987. 10: p. 1-16.
32. Reddy, S.C. and A. Fatemi. *Small crack growth in multiaxial fatigue*. in *Advances in fatigue lifetime predictive techniques*. 1992. Philadelphia,PA: ASTM STP.
33. Gao, H., M.W. Brown, and K.J. Miller, *Mixed mode fatigue thresholds*. *Fatigue Engng Mater Struct*, 1982. 5(1): p. 1-17.
34. Paris, P.C. and F. Erdogan, *A critical analysis of crack propagation laws*. *Trans. ASME, J. Basic Engng*, 1963. 55: p. 528-534.
35. Walker, K., *The effects of stress ratio during crack propagation and fatigue for 2024-T3 and 7075-T6 aluminum, in Effects of environment and complex load history on fatigue life.*. 1970, American Society for Testing and Materials: Philadelphia. p. 1-14.
36. Kim, J.-K. and C.-S. Kim, *Fatigue crack growth behavior of rail steel under mode I and mixed mode loadings*. *Materials Science and Engineering A*, 2002. 338(1-2): p. 191-201.
37. Forman, R.G., V.E. Kearney, and R.M. Engle, *Numerical analysis of crack propagation in cyclic-loaded structures*. *journal of Basic Engineering*, Trans, ASME, 1967. 89: p. 459-464.

38. Donahue, R.J., et al., Crack opening *displacement and the rate of fatigue crack growth*. *International Journal of Fracture Mechanics*, 1972. 8: p. 209-219.
39. Erdogan, F. and M. Ratwani, Fatigue and *fracture of cylindrical shells containing a circumferential crack*. *International Journal of Fracture Mechanics*, 1970. 6: p. 379-392.
40. Pook, L.P. and A.F. Greenan, Fatigue crack *growth threshold in mild steel under combined loading*. *ASTM STP 677*, Fracture Mechanics, 1979: p. 23-25.
41. Roberts, R. and J.J. Kibler, Mode II fatigue crack *propagation*. *J. Basic Engineering* (Trans. ASME), 1971. 93: p. 671-680.
42. Newman, J.C., A crack closure *model for predicting fatigue crack growth under aircraft spectrum loading*. *Methods and Models for Predicting Fatigue Crack Growth Under Random Loading*, ASTM STP, 1981. 748: p. 53-84.
43. Chen, W.R. and L.M. Keer, Fatigue crack *growth in mixed mode loading*. *J. Engng Mater. Technol*, ASME Trans., 1991. 113: p. 222-227.
44. Lam, Y.C., Mixed mode fatigue crack *growth and the strain energy density factor*. *Theor. appl. Fracture Mech*, 1989. 12: p. 67-72.
45. Lam, Y.C. and J.F. Williams, The effect of *contact stress intensity factors on fatigue crack propagation*. *Theor. appl. Fracture Mech*, 1984. 1: p. 193-202.
46. Theocaris, P.S. and N.P. Andrianopoulos, Author's closure *on the discussion by G. C. Sih and E. E. Gdoutos of "The Mises elastic-plastic boundary as the core region in fracture criteria"*. *Engng Fracture Mech*, 1984. 20: p. 691-694.
47. Yan, X., Z. Zhang, and S. Du, Mixed mode *fracture criteria for the materials with different yield strengths in tension and compression*. *Engng Fracture Mech*, 1992. 42: p. 109-116.
48. Wu, C.H., Fracture under *combined loads by maximum energy release rate criterion*. *J. appl. Mech.*, ASME Trans, 1978. 45: p. 553-558.
49. Wong, A.K., On the application of *the strain energy density theory in predicting crack initiation and angle of growth*. *Engng Fracture Mech*, 1987. 27: p. 157-170.
50. Li, C., Vector CTD criterion *applied to mixed-mode fatigue crack growth*. *Fatigue Fract. Eng. Mater. Struct*, 1989. 12(1): p. 59-65.
51. Dowling, N.E. and J.A. Begley, Fatigue crack *growth during gross plasticity and the J-integral*. *Mechanics of Crack Growth*, ASTM STP 590, 1976: p. 82-103.

52. Wuthrich, C., The extension of the *J-integral* concept to fatigue cracks. *Int. J. Fracture*, 1982. 20: p. R35–R37.
53. Srivastava, Y.P., Study on modified *J-integral* range and its correlation with fatigue crack growth. *Engng Fracture Mech*, 1988. 30: p. 119-133.
54. Chow, C.L. and T.J. Lu, Cyclic *J-integral* in relation to fatigue crack initiation and propagation. *Engng Fracture Mech*, 1991. 39: p. 1-20.
55. Hoshide, T. and D.F. Socie, Mechanics of mixed mode small fatigue crack growth. *Engng Fracture Mech*, 1987. 26: p. 841-850.
56. Tanaka, K., Fatigue crack propagation from a crack inclined to the cyclic tensile axis. *Engng Fracture Mech*, 1974. 6: p. 493-507.
57. Erdogan, F. and G.C. Sih, On the crack extension in plates under plane loading and transverse shear. *J. bas. Engng, ASME Trans.*, 1963. 85: p. 519-525.
58. Richard, H.A., *Role of Fracture Mechanics in Modern Technology*. Elsevier Science Publishing, North-Holland, 1987.
59. Rhee, H.C. and M.M. Salama, Mixed-mode stress intensity factor solutions of a warped surface flaw by three-dimensional finite element analysis. *Engineering Fracture Mechanics*, 1987. 28(2): p. 203-209.
60. Liu, Y. and S. Mahadevan, Threshold stress intensity factor and crack growth rate prediction under mixed-mode loading. *Engineering Fracture Mechanics*, 2007. 74(3): p. 332-345.
61. Liu, Y. and S. Mahadevan, A unified multiaxial fatigue damage model for isotropic and anisotropic materials. *International Journal of Fatigue*, 2007. 29(2): p. 347-359.
62. Lawson, L., E.Y. Chen, and M. Meshii, Near-threshold fatigue: a review. *International Journal of Fatigue*, 1999. 21(Supplement 1): p. 15-34.
63. El Haddad, M.H., T.H. Topper, and K.N. Smith, Prediction of non propagating cracks. *Engineering Fracture Mechanics*, 1979. 11(3): p. 573-584.
64. Erdogan, G. and G.C. Sih, On the crack extension in plates under plane loading and transverse shear. *Journal of Basic Engineering ASME Transactions*, 1963. 85: p. 519-527.
65. Wang, D.Z., et al., Fatigue crack propagation of extruded-19Vf%-SiCw/6061Al composites under mixed mode (I + II) loading. *Scripta Metallurgica et Materialia*, 1995. 32(10): p. 1637-1642.

66. Otsuka, A., K. Tohgo, and H. Matsuyama, Fatigue crack initiation *and growth under mixed mode loading in aluminum alloys 2017-T3 and 7075-T6*. *Engineering Fracture Mechanics*, 1987. 28(5-6): p. 721-732.
67. Soh, A.K. and L.C. Bian, Mixed mode fatigue crack *growth criteria*. *International Journal of Fatigue*, 2001. 23(5): p. 427-439.
68. Liu, P. and Z. Wang, Mixed-mode I and II fatigue *threshold and crack deflection angle in SiCP/2024Al composite*. *Scripta Materialia*, 1996. 34(8): p. 1323-1330.
69. Torres, Y., et al., Loading mode effects on *the fracture toughness and fatigue crack growth resistance of WC-Co cemented carbides*. *Scripta Materialia*, 2005. 52(11): p. 1087-1091.
70. Pook, L.P., Mixed mode I and III fatigue *crack growth thresholds for a range of steels*. 1986, *The National Engineering Laboratory*: East Kilbride.
71. Suresh, S., Fatigue of materials. 2 ed. 1998, *New York*: Cambridge University Press.
72. Yao, W., K. Xia, and Y. Gu, On the fatigue notch factor, *K_f*. *International Journal of Fatigue*, 1995. 17(4): p. 245-251.
73. Ciavarella, M. and G. Meneghetti, On fatigue limit in the *presence of notches: classical vs. recent unified formulations*. *International Journal of Fatigue*, 2004. 26(3): p. 289-298.
74. Smith, R.A. and K.J. Miller, Fatigue cracks at notches. *International Journal of Mechanical Sciences*, 1977. 19(1): p. 11-22.
75. Sehitoglu, H., Fatigue life prediction of *notched members based on local strain and elastic-plastic fracture mechanics concepts*. *Engineering Fracture Mechanics*, 1983. 18(3): p. 609-621.
76. Smith, R.A. and K.J. Miller, Prediction of fatigue regimes in *notched components*. *International Journal of Mechanical Sciences*, 1978. 20(4): p. 201-206.
77. Taylor, D., Geometrical effects in *fatigue: a unifying theoretical model*. *International Journal of Fatigue*, 1999. 21(5): p. 413-420.
78. Atzori, B. and P. Lazzarin, Notch sensitivity and defect *sensitivity under fatigue loading: two sides of the same medal*. *International Journal of Fracture*, 2001. 107(1): p. 1-8.

79. Creager, M. and P. Paris, Elastic field equations for blunt cracks with reference to stress corrosion cracking. *International Journal of Fracture Mechanics*, 1967. 3: p. 247-252.
80. Dini, D. and D. Hills, When does a notch behave like a crack. *Proceedings of the I MECH E Part C Journal of Mechanical Engineering Science*, 2006. 220(1): p. 27-43.
81. Kujawski, D., Estimation of stress intensity factors for small cracks at notches. *Fatigue and Fracture Engineering Materials and Structures*, 1991. 14(10): p. 953-965.
82. Jones, R. and D. Peng, A simple method for computing the stress intensity factors for cracks at notches. *Engineering Failure Analysis*, 2002. 9(6): p. 683-702.
83. Lucas, P., Stress intensity factors of small cracks at notches. *Engineering fracture Mechanics*, 1987. 26: p. 471-473.
84. Benthem, J. and W. Koiter, Asymptotic approximations to crack problems. *Mechanics of fracture*, 1973. 1: p. 137-178.
85. Jones, R., et al., Weight functions, CTOD, and related solutions for cracks at notches. *Engineering Failure Analysis*, 2004. 11(1): p. 79-114.
86. Gomez, F.J., et al., Local strain energy to assess the static failure of U-notches in plates under mixed mode loading. *International Journal of Fracture*, 2007. 145(1): p. 29-45.
87. Atzori, B., P. Lazzarin, and G. Meneghetti, Fracture mechanics and notch sensitivity. *Fatigue & Fracture of Engineering Materials and Structures*, 2003. 26(3): p. 257-267.
88. Forsyth, P.J.E. A two-stage process of fatigue crack growth. in *Crack Propagation Symposium. 1961. The College of Aeronautics*, University of Cranfield, Cranfield, UK.
89. Duggan, T., Fatigue and fracture mechanics. *Phys. Technol.*, 1983. 14: p. 126-132.
90. Paris, P., M. Gomez, and W. Anderson, A rational analytical theory of fatigue. *Trends Eng.*, 1961. 13: p. 9-14.
91. Miller, K., M. Brown, and J. Yates, Some observations on mixed-mode fatigue behavior of polycrystalline metals, in *Mixed-mode crack behavior*, ASTM STP 1359, D. McDowell, Editor. 1999, American Society for Testing and Materials: West Conshohocken, PA.

92. Paris, P. and F. Erdogan, A critical analysis of crack *propagation laws*. *J. Basic Eng.*, 1963. 85: p. 528-534.
93. Pearson, S., Initiation of fatigue cracks in *commercial aluminium alloys and the subsequent propagation of very short cracks*. *Eng Fract Mech*, 1975. 7(2): p. 235-247.
94. Narasaiah, N. and K.K. Ray, Study of short crack growth *behaviour in single and multiphase steels using rotating bending machine*. *International Journal of Fatigue*, 2006. 28(8): p. 891-900.
95. Obrtlík, K., et al., Short fatigue crack *behaviour in 316L stainless steel*. *International Journal of Fatigue*, 1997. 19(6): p. 471-475.
96. Murtaza, G. and R. Akid, Corrosion fatigue short crack *growth behaviour in a high strength steel*. *International Journal of Fatigue*, 1996. 18(8): p. 557-566.
97. Kaynak, C., A. Ankara, and T.J. Baker, A comparison of short and long *fatigue crack growth in steel*. *International Journal of Fatigue*, 1996. 18(1): p. 17-23.
98. Murtaza, G. and R. Akid, Modelling short fatigue crack *growth in a heat-treated low-alloy steel*. *International Journal of Fatigue*, 1995. 17(3): p. 207-214.
99. Hussain, K., E.R. De Los Rios, and A. Navarro, A two-stage micromechanics *model for short fatigue cracks*. *Engineering Fracture Mechanics*, 1993. 44(3): p. 425-436.
100. Brown, C.W. and M.A. Hicks, Study of short fatigue crack *growth behaviour in titanium alloy imi 685*. *Fatigue of Engineering Materials and Structures*, 1983. 6(1): p. 67-76.
101. Sinha, V., C. Mercer, and W.O. Soboyejo, An investigation of short and long *fatigue crack growth behavior of Ti-6Al-4V*. *Materials Science and Engineering A*, 2000. 287(1): p. 30-42.
102. Shademan, S. and W.O. Soboyejo, An investigation of short *fatigue crack growth in Ti-6Al-4V with colony microstructures*. *Materials Science and Engineering A*, 2002. 335(1-2): p. 116-127.
103. Ishihara, S. and A.J. McEvily, Analysis of short *fatigue crack growth in cast aluminum alloys*. *International Journal of Fatigue*, 2002. 24(11): p. 1169-1174.
104. Costa, J.D., C.M. Branco, and J.C. Radon, Short *fatigue crack growth behaviour in Al 5083 alloy*. *International Journal of Fatigue*, 1997. 19(2): p. 161-168.

105. Kaynak, C. and A. Ankara, Short fatigue crack growth in *AL 2024-T3 and AL 7075-T6*. *Engineering Fracture Mechanics*, 1992. 43(5): p. 769-778.
106. Pang, H.T. and P.A.S. Reed, Fatigue crack initiation and *short crack growth in nickel-base turbine disc alloys--the effects of microstructure and operating parameters*. *International Journal of Fatigue*, International Conference on Fatigue Damage of Structural Materials IV, 2003. 25(9-11): p. 1089-1099.
107. Healy, J.C., L. Grabowski, and C.J. Beevers, Short-fatigue-crack growth in a *nickel-base superalloy at room and elevated temperature*. *International Journal of Fatigue*, 1991. 13(2): p. 133-138.
108. Zhang, X.P., et al., Investigation of short fatigue cracks in *nickel-based single crystal superalloy SC16 by in-situ SEM fatigue testing*. *Scripta Materialia*, 2001. 44(10): p. 2443-2448.
109. James, M.N. and J.F. Knott, Aspects of Small Crack Growth. *AGARD (NATO), 1985. CP-393*: p. 10.1-10.12.
110. Leis, B.N., et al., Critical review of the fatigue growth of short cracks. *Engineering Fracture Mechanics*, 1986. 23(5): p. 883-898.
111. Hussain, K., Short fatigue crack behaviour and analytical models: A review. *Engineering Fracture Mechanics*, 1997. 58(4): p. 327-354.
112. Newman Jr, J.C., E.P. Phillips, and M.H. Swain, Fatigue-life prediction methodology using small-crack theory. *International Journal of Fatigue*, 1999. 21(2): p. 109-119.
113. Miller, K. A historical perspective of the important parameters of metal fatigue and problems for the next century. in *7th International Fatigue Congress (Fatigue'99)*. 1999. Beijing: Higher Education Press.
114. Chan, K. and J. Lankford, A crack-tip strain model for the growth of small fatigue cracks (in engineering alloys). *Scripta Metallurgica*, 1983. 17: p. 529-532.
115. Kim, J.-H. and G.H. Paulino, Mixed-mode fracture of orthotropic functionally graded materials using finite elements and the modified crack closure method. *Engineering Fracture Mechanics*, 2002. 69(14-16): p. 1557-1586.
116. AFGROW Reference Manual (version 4.0). 2003, Wright-Patterson Air Force Base, AFRL/VASM.
117. Mcevely, A., D. Eifler, and E. Macherauch, An analysis of the growth of short fatigue cracks. *Engineering Fracture Mechanics*, 1991. 40(3): p. 571-584.

118. de los Rios, E.R., Z. Tang, and K.J. Miller, Short crack fatigue behaviour in a medium carbon steel. *Fatigue of Engineering Materials and Structures*, 1984. 7(2): p. 97-108.
119. Dang Van, K., Macro-Micro approach in high-cycle multiaxial fatigue, in *Advances in Multiaxial Fatigue*. 1993. p. 120-130.
120. Tanaka, K., et al., Modelling of small fatigue crack growth interacting with grain boundary. *Engineering Fracture Mechanics*, 1986. 24(6): p. 803-819.
121. Yang, Y., et al., Nanoscale and submicron fatigue crack growth in nickel microbeams. *Acta Materialia*, 2007. 55(13): p. 4305-4315.
122. Hall, E.O., The deformation and aging of mild steel. *Proc. Phys. Soc. B*, 1951. 64: p. 747-753.
123. Petch, N.J., The cleavage strength of polycrystals. *J Iron Steel Inst*, 1953. 25(8): p. 174.
124. Su, R.K.L. and H.Y. Sun, Numerical solutions of two-dimensional anisotropic crack problems. *International Journal of Solids and Structures*, 2003. 40(18): p. 4615-4635.
125. Saouma, V.E., M.L. Ayari, and D.A. Leavell, Mixed mode crack propagation in homogeneous anisotropic solids. *Engineering Fracture Mechanics*, 1987. 27(2): p. 171-184.
126. Lim, W.-K., S.-Y. Choi, and B.V. Sankar, Biaxial load effects on crack extension in anisotropic solids. *Engineering Fracture Mechanics*, 2001. 68(4): p. 403-416.
127. Xu, Y. and L.M. Keer, Crack curving in anisotropic elastic solids. *Engineering Fracture Mechanics*, 1993. 44(1): p. 63-73.
128. Liu, H.W., A Dislocation barrier model for fatigue crack growth threshold. *International Journal of Fracture*, 1998. 93(1): p. 261-280.
129. Miller, K., The behavior of short fatigue cracks and their initiation, parts I+II. *Fatigue Fract. Eng. Mater. Struct.*, 1987. 10: p. 75-113.
130. Kabo, E. and A. Ekberg, Fatigue initiation in railway wheels--a numerical study of the influence of defects. *Wear*, 2002. 253(1-2): p. 26-34.
131. Bernasconi, A., et al., Multiaxial fatigue of a railway wheel steel under non-proportional loading. *International Journal of Fatigue*, Selected papers from the 7th International Conference on Biaxial/Multiaxial Fatigue and Fracture (ICBMFF), 2006. 28(5-6): p. 663-672.

132. Ekberg, A. and E. Kabo, Fatigue of railway wheels and *rails under rolling contact and thermal loading--an overview*. *Wear, Contact Mechanics and Wear of Rail/Wheel Systems*, 2005. 258(7-8): p. 1288-1300.
133. **Giammarise**, A. and R. Gilmore, Wheel Quality: A north American locomotive builder's perspective. 2001, GE Research & Development Center.
134. Stone, D., G. Majumder, and V. Bowaj. Shattered rim wheel defects and the effect of lateral loads and brake heating on their growth. in *ASME International Mechanical Engineering Congress & Exposition*. 2002. New Orleans, Louisiana.
135. Stone, D., C. Lonsdale, and S. Kalay. Effect of wheel impact loading on shattered rims. in *Proceedings of 13th International Wheelset Congress*. 2001. Rome.
136. Murikami, Y. and M. Endo, Effects of defects, inclusions, and inhomogeneities on fatigue strength. *International Journal of Fatigue*, 1994. 16: p. 163-182.
137. Lunden, **R.** Cracks in railway wheels under rolling contact load. in *Proceedings of the 10th International Wheelset Congress*. 1992. Australia.
138. Beretta, S., et al. Deep shelling in railway wheels. in *Proceedings of the 13th International Wheelset Congress*. 2001. Italy.
139. Marais, J. Wheel failures on heavy haul freight wheels due to subsurface defects. in *Proceedings of the 12th International Wheelset Congress*. 1998. China.
140. Stone, D. and G. Dahlman, The effect of discontinuity size on the initiation of shattered rim defects. *ASME Rail Transportation Division*, 2000. 19: p. 7-14.
141. Melander, A. Simulation of the behaviour of short cracks at inclusions under rolling contact fatigue loading-specially the effect of plasticity. in *bearing steels: into the 21st century*. 1998.
142. Fry, G.T., F.V. Lawrence, and A.R. Robinson, A model for fatigue defect nucleation in thermite rail welds. *Fatigue Fract. Eng. Mater. Struct.*, 1996. 19: p. 655-668.
143. Ekberg, A. and P. Sotkovszki, Anisotropy and rolling contact fatigue of railway wheels. *International Journal of Fatigue*, 2001. 23(1): p. 29-43.
144. Ansys, ANSYS Theory Reference, release 7.0. 2003, ANSYS, Inc., .
145. AAR, Manual of Standards and Recommended Practices: Section G-Wheels and Axles. 1998.